IOP Publishing and International Atomic Energy Agency Nuclear Fusion
Nucl. Fusion **52** (2012) 083020 (36pp) doi:10.1088/0029-5515/52/8/083020

Exploration of the equilibrium operating space for NSTX-Upgrade

S.P. Gerhardt, R. Andre and J.E. Menard

Princeton Plasma Physics Laboratory, Princeton, NJ 08543, USA

E-mail: sgerhard@pppl.gov

Received 14 December 2011, accepted for publication 10 July 2012
Published 1 August 2012
Online at stacks.iop.org/NF/52/083020

Abstract
This paper explores a range of high-performance equilibrium scenarios achievable with neutral beam heating in the NSTX-Upgrade device (Menard J.E. 2012 *Nucl. Fusion* **52** 083015). NSTX-Upgrade is a substantial upgrade to the existing NSTX device (Ono M. *et al* 2000 *Nucl. Fusion* **40** 557), with significantly higher toroidal field and solenoid capabilities, and three additional neutral beam sources with significantly larger current-drive efficiency. Equilibria are computed with free-boundary TRANSP, allowing a self-consistent calculation of the non-inductive current-drive sources, the plasma equilibrium and poloidal-field coil currents, using the realistic device geometry. The thermal profiles are taken from a variety of existing NSTX discharges, and different assumptions for the thermal confinement scalings are utilized. The no-wall and ideal-wall $n = 1$ stability limits are computed with the DCON code. The central and minimum safety factors are quite sensitive to many parameters: they generally increase with large outer plasma-wall gaps and higher density, but can have either trend with the confinement enhancement factor. In scenarios with strong central beam current drive, the inclusion of non-classical fast-ion diffusion raises $q_{\min}$, decreases the pressure peaking, and generally improves the global stability, at the expense of a reduction in the non-inductive current-drive fraction; cases with less beam current drive are largely insensitive to additional fast-ion diffusion. The non-inductive current level is quite sensitive to the underlying confinement and profile assumptions. For instance, for $B_T = 1.0$ T and $P_{inj} = 12.6$ MW, the non-inductive current level varies from 875 kA with ITER-98y,2 thermal confinement scaling and narrow thermal profiles to 1325 kA for an ST specific scaling expression and broad profiles. Scenarios are presented which can be sustained for 8–10 s, or (20–30) τ_{CR}, at $\beta_N = 3.8$–4.5. The value of $q_{\min}$ can be controlled at either fixed non-inductive fraction of 100% or fixed plasma current, by varying which beam sources are used, opening the possibility for feedback control of the current profile. In terms of quantities like collisionality, neutron emission, non-inductive fraction, or stored energy, these scenarios represent a significant performance extension compared with NSTX and other present spherical torii.

(Some figures may appear in colour only in the online journal)

1. Introduction and motivation

The spherical torus (ST) [1] is a leading candidate for the plasma core of facilities designed to study plasma material interactions [2], nuclear component testing [3–10] or to generate fusion power [11–15]. This interest is driven by the compact nature of the ST device and associated excellent utilization of the toroidal field (TF), the natural elongation of the plasma cross-section [1, 16], the high neutron wall loading, the significantly higher β values [17, 18] and potential ease of maintenance [2, 4, 6].

However, in order to connect the database of results from present 1 MA class STs, such as the National Spherical Torus experiment (NSTX) [19] or the Mega-Ampere Spherical Tokamak (MAST) [20], to the scenario requirements for machine targeting those next-step missions, better physics understanding is required in many areas. Among the most critical of these issues are the scaling of the electron transport with field and current [21–25], the physics of fast particles in the lower field of the ST [26–35] and the ability to non-inductively sustain the high-beta ST configuration (see [36–44] for progress towards this goal in NSTX and [45, 46] for progress in MAST).

The NSTX-Upgrade facility [47] has been designed to address these and other critical issues. There are two primary components to this upgrade of the existing NSTX device. The first is a complete replacement of the 'centre stack', which contains the inner-leg of the TF coils, the ohmic heating (OH) solenoid and some divertor coils. This allows an increase of the TF capability from 0.55 to 1.0 T and an increase in the

plasma current from a maximum of ∼1.3 to 2.0 MA, with significantly longer pulse capability. The second upgrade is the addition of a second neutral beam injector with more tangential injection. This provides more auxiliary heating power, and equally importantly, additional neutral beam current drive (NBCD).

Of course, the scenarios for NSTX-Upgrade cannot be fully defined in advance, because the physics knowledge required to define those scenarios is incomplete; this uncertainty is among the primary motivations of the Upgrade project. This study will scan important quantities which have some uncertainty (global confinement, anomalous fast-ion diffusivity, profile shapes), in order to quantify the effects of various assumptions. This will in turn identify scenarios where small variations in these quantities will have a large impact, and thus facilitate important physics studies.

The rest of this paper is organized as follows. Section 2 provides a brief summary of the facility modifications associated with the NSTX-Upgrade project. Section 3 describes the numerical tools used in this study. Section 4 illustrates a comparison of the free-boundary equilibrium solver in TRANSP with actual NSTX data. Section 5 describes the effect of some important parameters on the performance of NSTX-Upgrade plasmas; variations in the outer plasma-wall gap, global thermal confinement, plasma density, anomalous fast-ion diffusivity, ion thermal diffusivity and $Z_{\rm eff}$ (both at fixed global confinement), and profile shapes are all considered. Section 6 describes six different scenario optimizations:

- Section 6.1 studies 100% non-inductive scenarios optimized at high-injected power and high plasma current.
- Section 6.2 addresses partial-inductive configurations with high current, field and heating power.
- Section 6.3 describes lower power scenarios at somewhat reduced TF strength ($B_{\rm T} = 0.75$ T) and plasma current, which are in principal sustainable for 8–10 s.
- Section 6.4 addresses configurations designed to maximize the *sustainable* toroidal β.
- Section 6.5 describes the ability to control the current profile using various combinations of four of the available heating neutral beam sources.
- Section 6.6 examines the possibility of achieving scenarios with bootstrap fractions exceeding 80% using neutral beam heating alone.

Section 7 provides a comparison between the parameters already achieved in NSTX and the projected parameters of NSTX-Upgrade. A summary and discussion is provided in section 8.

2. The NSTX-Upgrade facility

As noted above, NSTX-U represents a major expansion of the physics capabilities of the facility. A comprehensive overview of the NSTX-Upgrade physics motivation and engineering design is given in [47]. This section describes briefly those upgrades relevant to this study.

The first major component of the upgrade is a new centre column with upgraded TF and OH coils. The TF upgrade is reflected in two figures of merit. First, the maximum field that can be created at the plasma midradius is increased from 0.55 to 1.0 T. Second, the $\int I_{\rm TF}^2\,{\rm d}t$ limit, which is indicative of coil heating limits, is increased by a factor of 20 (from 6×10^9 to 1.2×10^{11} A^2 s). Hence, both higher fields and longer pulses will be available. The OH coil also has significant new capability, with the $\int I_{\rm OH}^2\,{\rm d}t$ limits increased by a factor of 3.5 (from 2.5×10^8 to 8.5×10^8 A^2 s), and the flux available for driving inductive current increased from 0.75 to 2.1 Wb.

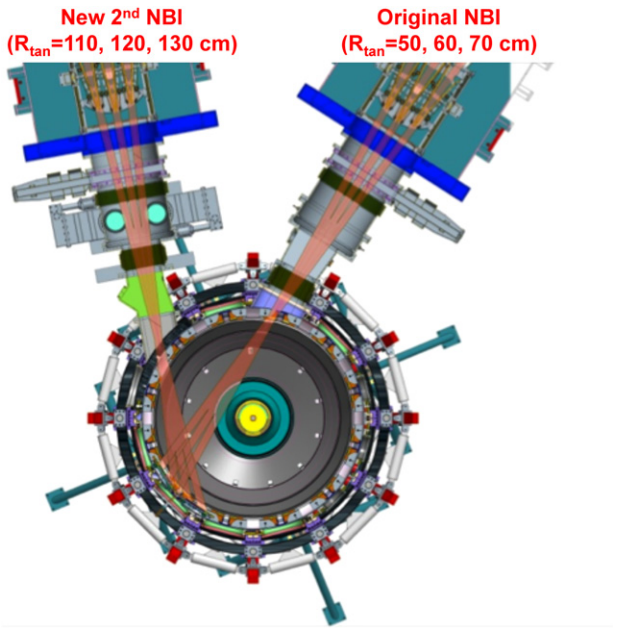

Figure 1. Illustration of the present neutral beam injector utilized in NSTX, and the second neutral beam injector that is a primary component of the NSTX-Upgrade project.

These enhanced capabilities come from both improved magnet design and an increase in the radius of the centre column allowing larger conductors and an increase in the solenoid radius. In particular, the inboard PFC boundary is increased from $R = 18.5$ cm in NSTX to $R = 31.5$ cm in NSTX-Upgrade. As a consequence, typical aspect ratios $A = R_0/a$ for NSTX-Upgrade scenarios are $1.65 < A < 1.8$, compared with $1.35 < A < 1.6$ for NSTX. Here, R_0 is defined as the mean radii of the inner- and outer-midplane separatrix radii, while the minor radius a is the defined as the half-distance between them. Structural improvements required for safe operations at these higher fields and currents are described in [47].

As illustrated in figure 1, the second major component of the Upgrade is the addition of a second neutral beamline, complementing the existing NSTX heating systems [48] with three additional beam sources. As will be discussed in great detail throughout this paper, the increased heating power is only one motivation for this addition. Equally important, the new beamline is steered to have a significantly larger beam tangency radius, which improves the current-drive efficiency and provides the option for off-axis NBCD [43, 47].

The NSTX neutral beams are a reuse of the system originally designed and implemented on TFTR [49–51]. Each beamline has three sources assembled horizontally in a fan array, with the crossing-point of the three beams at approximately the point where they enter the vessel. Both

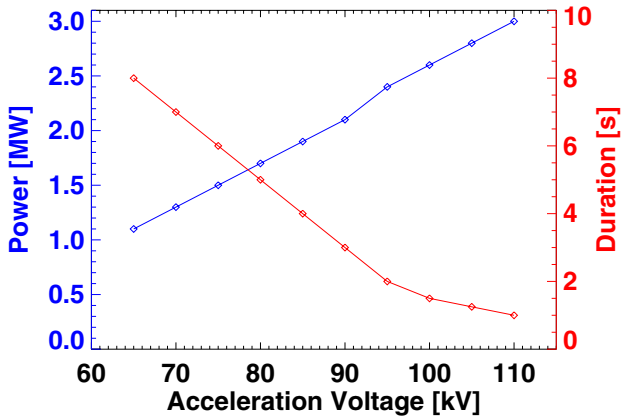

Figure 2. Power and allowable pulse duration for the NSTX neutral beam systems, as a function of the acceleration voltage.

the new and old beamlines inject horizontally at the vessel midplane. The original NSTX beamline has sources with tangency radii of $R_{\text{tan}} = 50$, 60 and 70 cm; the new beamline has sources with tangency radii of 110, 120 and 130 cm. As described in [47], the outermost beam, with $R_{\text{tan}} = 130$ cm, provides substantial off-axis NBCD. Note that off-axis NBCD has been observed [52–54] and utilized [55, 56] in conventional aspect-ratio tokamaks as well as STs [57].

An important determinant of the scenario parameters are the power and pulse duration achievable for a given neutral beam acceleration voltage. These parameters for the NSTX-U neutral beam systems are given in figure 2. A higher beam voltage will clearly provide more power and better beam penetration to the plasma core. However, the allowable pulse duration, limited by heating of the primary energy ion dump, decreases rapidly as the voltage is increased. The scenarios in this paper will most commonly utilize 90 kV sources, which produce 2.1 MW for up to 3 s; this duration typically allows the current profile to fully equilibrate. Lower beam voltages (80 and 65 kV) will be used for scenarios where longer pulse is desired, and higher beam voltages will be used for scenarios that desire additional power and current drive, at the expense of pulse length.

3. Computation techniques

3.1. Free-boundary TRANSP simulations

The primary computation tool utilized in this study is the recently available free-boundary equilibrium capability in the TRANSP code [58]. For the NSTX-Upgrade simulations described in sections 5–7 of this manuscript, the inputs to these simulations are the time histories of the requested plasma boundary shapes and plasma current level, electron temperature and density profiles mapped to the minor radius (defined as the square-root of toroidal flux), and the power, voltage and geometry of the neutral beam injection. For the demonstration simulations of existing NSTX data in section 4, the ion temperature, ion density and safety factor profiles are also used as inputs to the code. The measured shaping and divertor coil currents are never used to constrain the calculations in the code.

These inputs are used to compute the bootstrap current [59–62] using the Sauter model [63]. The NBCD [64–67] is computed by the NUBEAM code [67]; 8000–16 000 particles were typically used in these simulations, weighted towards the plasma core to reduce the Monte Carlo noise on the central beam current drive (wghta = 10 [67]). The beam-current shielding factor derived by Lin-Liu and Hinton [66] is used.

These plasma parameter and current profile data are then used to compute the fully relaxed current profile for the NSTX-U simulations in sections 5–8. The poloidal-field diffusion equation [68] is solved to relax the current profile; we allow this calculation to run for at least four seconds with no other changes to the input parameters, so that the fully relaxed state can be studied. It is possible that the total of the non-inductive currents are greater than the total requested current, and these cases will be indicated as non-inductive fractions greater than 100%. These cases will have negative inductive currents and negative surface voltages, so that the total current level is matched to the request. Note that there is no effort to model the ramp-up in these simulations, and the equilibria presented here represent 'snap-shots' of the fully relaxed state. Overall, more than 11 500 separate fully relaxed equilibria were generated over the course of these studies. Note that the analysis of the NSTX experimental data in section 4 uses the q-profile derived from experimental equilibrium reconstruction, and does not solve poloidal-field diffusion.

The free-boundary capability utilized in this study comes from the recent inclusion of the ISOLVER equilibrium code within TRANSP. The desired plasma boundaries in this study were generated with the stand-alone free-boundary equilibrium ISOLVER code, utilizing the coil set of NSTX-Upgrade. These plasma boundaries were then given to TRANSP as the 'target' boundaries for the free-boundary simulations. Using these target boundaries and the pressure and current profiles described above, ISOLVER then computes a free-boundary solution to the Grad–Shafranov whose boundary and X-point locations are closest to the target boundary and X-points. This new equilibrium is used as the starting point for the next iteration, where new profiles of the current and pressure are computed on that equilibrium, followed by recalculation of the free-boundary equilibrium. This iteration is then repeated through the calculation. There are no vessel eddy currents in the calculation.

In the context of heating and current-drive systems, we note that NSTX has a 30 MHz high-harmonic fast wave (HHFW) heating and current-drive system [69–71]. This system has demonstrated the ability to heat L-mode plasmas to very high temperatures when an internal transport barrier forms [72, 73]. However, the system has historically been less successful at heating deuterium H-mode plasmas that are also heated by neutral beams; only recently have a few examples of HHFW heating in NB H-modes been observed [71]. Specific issues include (i) the propagation of waves in the scrape-off layer (SOL) [70], which reduces the power available for core heating, and (ii) the tendency of the waves to damp on the fast ions rather than the electrons [69, 74]. However, neither of these processes is treated properly in the HHFW modules available in TRANSP. We also note that the current driven by direct HHFW current drive tends to be small and centrally peaked, due to the large electron trapping at low aspect ratio

[70]. Finally, the next section will describe how we use a range of experimental profiles and confinement assumptions in setting the electron temperature profile in these simulations; we do not have such a database of HHFW heated H-modes for use in simulation. For all these reasons we do not address HHFW simulations in these simulations. It is, however, anticipated that the HHFW system will be used for both RF physics and scenario development studies in NSTX-Upgrade.

3.2. H-mode confinement and profile assumptions

A first-principles integrated simulation of these scenarios would involve a validated model for the ion and electron thermal transport in both the plasma core and edge pedestal. With regard to ions, we infer from experiment that neoclassical theory describes the heat transport reasonably well [22, 23, 25, 75]. Models for the electron transport are not as well established.

For the plasma core, the dependence of the core χ_e on the plasma current profile would be a key component of such a model [76, 77]. Models such as GLF23 [78] or, more recently, TGLF [75, 79] have been used for this purpose in modelling the core electron transport at conventional aspect ratio [80–82]. The electron temperature gradient (ETG) [83–85] and/or microtearing modes [86–88] that have been suggested as the source of electron transport in the ST are in principle included in the transport model formulation noted above. However, these models have not been successfully validated against ST profiles (see [75] for initial work in this area). Furthermore, it has also been suggested that fast-particle-driven MHD instabilities could contribute to the observed electron transport in the ST [89]. This transport mechanism would not be included in turbulence-based reduced transport models noted above.

It would also be desirable to have a first-principles model for the height of the H-mode [90] pedestal, which sets the boundary condition for the core physics modelling. At conventional aspect ratio, models such as EPED1 [91] are being developed to predict the pedestal height. This model utilizes a combination of peeling–ballooning stability and transport driven by kinetic ballooning modes to determine the pedestal structure. However, the applicability of this model to the ST is not yet established. There is evidence that peeling–ballooning physics plays an important role in determining the edge stability [92–95], and some evidence that kinetic ballooning modes can be the dominant instability in the pedestal region [96]. However, the detailed experiment/theory comparisons of pedestal structure have not been completed as at conventional aspect ratio. Hence, for the reasons stated in this and the previous paragraph, first-principles calculations of the electron temperature profile shape and magnitude are not at the moment possible.

A similar situation exists with respect to the density profile. In this case, neither the external fuelling and impurity sources such as gas puffing, nor the particle and impurity transport, are sufficiently well understood and quantified for inclusion in these integrated models.

For these reasons we have decided to use experimental profiles for the electron temperature and density shapes in these simulations, while simulating the ion thermal transport using neoclassical theory. In particular, the experimental electron density profile is scaled to achieve a desired Greenwald fraction $f_{GW} = \bar{n}_e/(I_P/\pi a^2)$ [97, 98]. The ion thermal transport is predicted by the Chang–Hinton formulation [99]. The ion density is calculated assuming a flat Z_{eff} profile, with carbon being the only impurity (the baseline plasma facing component (PFC) material for NSTX-U is graphite). The value of Z_{eff} is 2 unless stated otherwise. The electron temperature profile input to the TRANSP simulation is a scaled version of the experimental profile, with the scale factor set to give a desired global confinement level for the resulting simulation. Finally, the toroidal rotation profile used in the simulations is taken from experiment, but scaled inversely with the density. While this does not take into account any confinement changes with increased field and current or increase in torque with additional beams [47], it is sufficient for the present simulations where only the beam deposition profile is slightly modified by different rotation magnitudes.

Two different assumptions for the 0D thermal confinement are utilized in this modelling. The first is the standard $H_{98y,2}$ scaling expression [100], given by

$$\tau_{98y,2} \propto I_P^{0.93} B_T^{0.15} \bar{n}_e^{0.41} P_{Loss}^{-0.69} R_0^{1.97} \varepsilon^{0.58} \kappa^{0.78}. \quad (1a)$$

The second scaling assumption is a ST expression [21], given by

$$\tau_{ST} \propto I_P^{0.57} B_T^{1.08} \bar{n}_e^{0.44} P_{Loss}^{-0.73}. \quad (1b)$$

This second expression was determined by ordinary least squares regression on a database of NSTX beam heated H-mode discharges. The primary difference between these expressions is the scaling with TF and plasma current, and this will have implications for the scenarios described below. For instance, the optimization to highest non-inductive fraction utilizes the highest TF possible at less than maximum plasma current; in these cases, the ST scaling expression predicts a more favourable result. On the other hand, the optimization to high toroidal β utilizes higher plasma current but lower TF strength; the ITER-98y, 2 scaling expression is more favourable in this case. We also note that other forms of the ST confinement time have been presented. For instance, [21] uses a different regression technique to derive a scaling expression with somewhat weaker B_T, n_e and P_{loss} dependences. On the other hand, an analysis of data from MAST [24] shows significantly weaker power degradation and stronger B_T dependence compared with equation (1*b*), with no dependence of confinement on density.

Secondly, the simulations have been run with different n_e and T_e profile shapes, from five different discharges taken in NSTX. Many cases utilize the profiles from the high aspect-ratio discharge 142301 [44]; these profiles generally produce the best performance. Also tested are profiles from a very high β_P discharge (133964) and a high β_T discharge 135129 [44]. These three discharges were made with active lithium conditioning of the PFCs [101, 102]. Hence, we also consider a very long pulse (116313) [36, 38] and a high-current (121123) discharge made before the advent of lithium conditioning. These five discharges span the range of thermal pressure profile peaking observed in NSTX H-modes. We note that there is considerable evidence from conventional aspect-ratio devices that the density peaking increases with decreasing

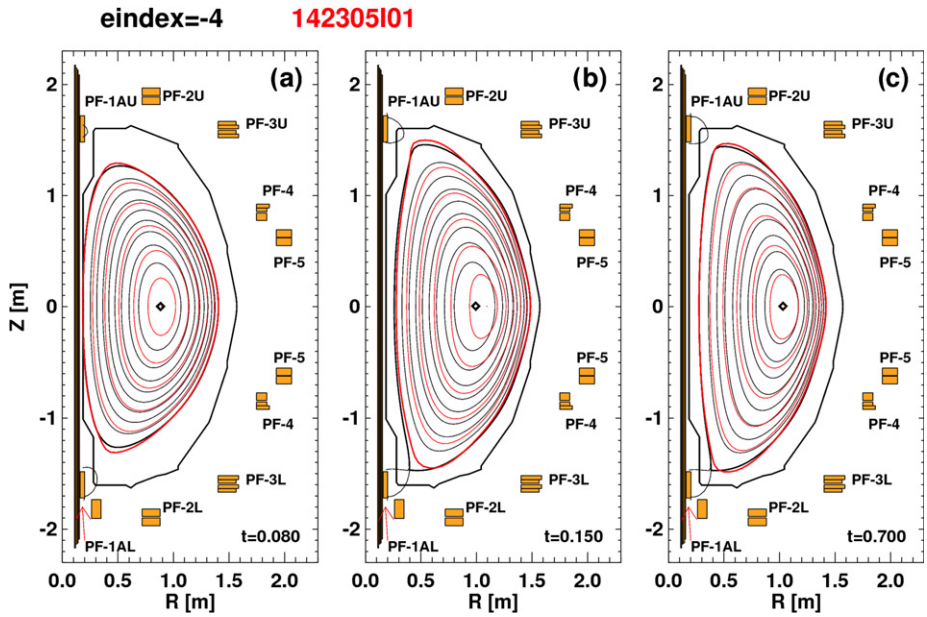

Figure 3. Comparison of the input (black) and calculated (red) equilibria using free-boundary TRANSP for discharge 142305. See the text for additional details.

collisionality [103, 104]. However, no experimental study has confirmed this trend for the ST, and we do not here attempt to project the profile shapes to the lower collisionality operating points of NSTX-Upgrade.

3.3. Global stability calculations

We have evaluated some of these NSTX-U scenarios for their global ideal $n = 1$ stability, both with and without an ideally conducting wall. In these cases, the equilibria generated by TRANSP are given to the fixed-boundary equilibrium code CHEASE [105], which refines the equilibrium in preparation for the stability calculation. The inverse-equilibria generated by CHEASE is then given to the DCON code [106]. DCON computes a stability metric δW for external modes that is positive for a stable configuration and negative for unstable configurations; the magnitude of the parameter can be taken as an indicator of proximity to the stability boundary. The calculation of δW can be done without a nearby conducting wall, or with an ideally conducting wall at the approximate location of the stabilizing passive plates. DCON also provides a binary answer regarding the stability of internal modes.

4. Comparison of the free boundary solver results with experimental equilibrium

Before considering simulations of NSTX-Upgrade, it is useful to test the free-boundary solver against actual NSTX equilibria. This exercise has been completed for a variety of NSTX discharges. The results of such a test are presented in this section.

As noted in section 3.1, these simulations are run in a slightly different manner than the NSTX-U simulations that are the focus of this paper. The time evolution of the plasma boundary, q-profile, electron, ion and carbon thermal profiles, and neutral beam heating sources are provided as input to the code. However, the time-history of the shaping and divertor coil currents is not used by code. The poloidal-field diffusion equation is not solved, since this information is present in the time-sequence of experimental equilibria. ISOLVER (in TRANSP) then uses the given q-profile, pressure profile computed as the summed experimental thermal pressure and computed fast-ion pressure, and target plasma boundary shape as inputs. The outputs of such an equilibrium calculation are the computed plasma boundary that best matches the target boundary and X-point locations in a least-squares sense, and the coil currents determined by the code. The plasma boundary and coil currents so computed by TRANSP can then be compared with the reconstructed experimental plasma boundary (the target boundary in TRANSP) and the actual coil currents. Note that the coil currents are determined at each time step independent of previous time step, resulting in some jitter in the computed currents that is not present in a real coil with finite inductance and power supply voltage.

Figure 3 shows the plasma boundary at three different times, for the discharge under consideration for this code demonstration, while figure 4 shows the coil currents for this case. This discharge was chosen because it is similar to the high-elongation and triangularity discharges utilized for NSTX-Upgrade simulations in the following sections, though at lower aspect ratio. The black curves show the experimental equilibrium as reconstructed by the LRDFIT reconstruction code [36]. These particular reconstructions are constrained by magnetic field and flux measurements at the vessel wall and a requirement that the magnetic surfaces are an isotherm (based on midplane Thomson scattering electron temperature data on both sides of the magnetic axis). The reconstruction is not constrained to match any measurement or estimate of the pressure profile, and there are no rotational effects that would lead to pressure not being a flux-surface function. The boundary of this reconstructed equilibrium is input to TRANSP/ISOLVER, which the free-boundary equilibrium code tries to match.

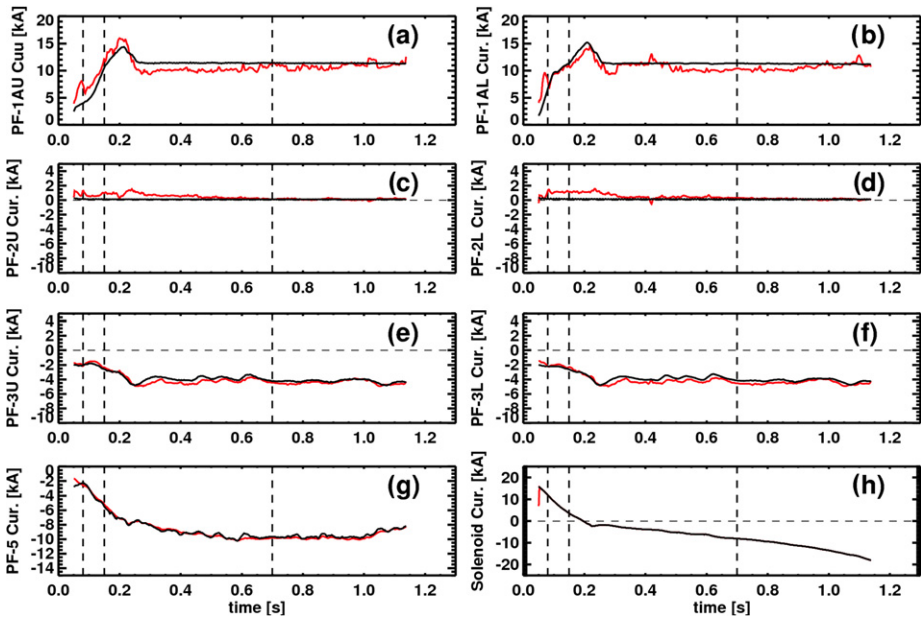

Figure 4. Comparison of the measured (black) and TRANSP-computed (red) coil currents for discharge 142305. The locations of the various coils are indicated in figure 3, and the dashed vertical lines correspond to the times in figure 3. See text for additional details.

This equilibrium computed by ISOLVER within TRANSP is shown in red in figure 3. The three times correspond to (a) the inner-wall limited phase just before the plasma is diverted, (b) just before the end of the current ramp and (c) well into the flat-top. A good match to the plasma boundary is generally achieved. The internal surfaces, on the other hand, do not always agree as well. This is due to mismatches in the pressure profile between those in LRDFIT and TRANSP; the pressure profile in TRANSP is more peaked due to the central fast-ion pressure. The problem is especially severe at earlier time in frame (*b*), where 4 MW of heating power into a lower density plasma results in a peaked pressure profile in TRANSP; the reconstruction do not have such a peaked profile, and have a smaller shift of the inner surfaces. Potential reasons for the discrepancy include (i) the presence of MHD activity in that early, low-density phase of the discharge leading to a broadening of the otherwise peaked fast-ion pressure profile predicted by TRANSP, and (ii) inaccuracy of the LRDFIT reconstruction, which has only the isotherm internal constraint, but no direct constraint on the pressure or current profile.

The experimental and computed coil currents are indicated in figure 4, with the vertical dashed lines corresponding to the times in figure 3. Frames (*a*) and (*b*) show the currents in the two active divertor coils (PF-1AU and -1AL). Frames (*c*) and (*d*) show the currents in divertor coils that were not used in this discharge. Reasonable agreement is found for all four divertor coils; in particular the code does not attempt to put a significant level of current in the coils that were not energized in the actual discharge. The PF-3 coils in frames (*e*) and (*f*) control the plasma elongation and vertical position, while the PF-5 coil in frame (*g*) provides the main vertical field [107] and controls the plasma outer-midplane radius. These coils also show good agreement between the actual currents and those computed by TRANSP. Finally, because the solenoid is not well coupled to the plasma shape, the solenoid current (frame (*h*)) in the TRANSP runs was forced to match to measured current evolution.

Note additionally that the TRANSP calculations do not have any vessel eddy currents. The actual experiments and reconstructions, however, have substantial vessel currents [108], especially during the early current ramp. These vessel currents are thus reflected in the coil currents computed by TRANSP, though this does not result in large discrepancies.

5. Parametric considerations for H-mode scenario optimization

A large number of parameters influence the relaxed equilibrium state of the plasmas. In this section, we explore a number of these dependences. In particular, the roles of the outer gap, plasma density and thermal confinement level, anomalous fast-ion diffusion, ion thermal transport level, $Z_{\rm eff}$, and profile shapes in determining the non-inductive current-drive profiles and magnitudes are addressed. Note that all profiles in this paper have shapes from H-mode discharges; this operating regime is well established on both MAST [109] and NSTX [110] and provides the broad profiles required for global stability. These scans will lay the foundation for the scenario optimizations discussed in section 6.

The sensitivity studies in this section will be shown in the context of three different scenario targets, listed in table 1, and denoted as S1–S3. These three discharge targets are broadly representative of the cases discussed in section 6. The first (S1) is a $B_{\rm T} = 1.0\,{\rm T}$, $I_{\rm P} = 1.0\,{\rm MA}$, $P_{\rm inj} = 12.6\,{\rm MW}$ scenario with $A = 1.73$ (except in 5.5, where it is studied at $A = 1.75$), designed to operate near 100% non-inductive current drive. The second (S2) is a $B_{\rm T} = 1.0\,{\rm T}$, $I_{\rm P} = 1.6\,{\rm MA}$, $P_{\rm inj} = 10.2\,{\rm MW}$ scenario with $A = 1.75$, designed to be sustained for $\sim$5 s at high current. The third (S3) is a $B_{\rm T} = 0.55\,{\rm T}$, $I_{\rm P} = 1.2\,{\rm MA}$, $P_{\rm inj} = 8.4\,{\rm MW}$ scenario designed to sustain high toroidal β of $\sim$25% for $\sim$3 s. All of these studies use the scaled electron temperature and density profiles from high aspect-ratio discharge 142301, except in section 5.6, where

Table 1. Scenarios utilized in the sensitivity studies of sections 5.2–5.6. All cases in section 5 have $H_{98y,2} = 1.0$ unless otherwise stated.

Label	Goal	I_P (MA)	B_T (T)	P_{inj} (MW)	f_{GW}	A	Symbol/linestyle in figures 11, 14 and 15.
S1	Very high non-inductive fraction	1	1	12.6 (six 90 kV beams)	0.72	1.73 (except for 5.6, when $A = 1.75$)	Diamond/solid
S2	High-current long-pulse	1.6	1	10.2 (six 80 kV beams)	0.72	1.75	Triangle/dashed
S3	Sustained high-β_T with $q_{min} > 1.1$	1.2	0.55	8.4 (four 90 kV beams	0.86	1.8	Squares/dotted

the sensitivity of these results to the thermal profile shapes is discussed.

Note that for these and all further NSTX-U simulations, the inputs to the simulations are the boundary shape and plasma current, electron temperature and density profiles, neutral beam parameters and magnitude of Z_{eff} with a flat profile. The poloidal-field diffusion equation is solved to develop the fully relaxed equilibrium. See section 3 for additional information regarding the simulation techniques.

5.1. Role of the outer gap

The plasma shape is a key parameter in determining the ability of a tokamak to achieve large bootstrap currents and sustain high-β [37, 39, 44, 111–114]; NSTX-Upgrade is no exception to this rule. In general, it is desirable to keep the inner plasma-wall gap as small as reasonably possible in order to maintain low aspect ratio; this results in the best utilization of the TF. The elongation is optimized by making the plasma tall, consistent with maintaining gaps at the top and bottom. The plasma triangularity is maintained at a high level, also to improve utilization of the TF [113].

This leaves the outer-midplane plasma-wall gap, referred to from here on as the 'outer gap', as the remaining low-order parameter for optimization (we note that the plasma 'squareness' can also be optimized to improve performance [115], provided sufficient shaping flexibility exists). A smaller value of outer-gap results in a plasma that fully fills the vessel. It also brings the plasma close to the passive stabilizing plates. A large value of outer gap increases the elongation and causes the $R_{tan} = 120$ and 130 cm sources to drive current farther off the magnetic axis.

A series of target plasma boundary shapes were created in order to understand this optimization. These double-null shapes, shown in figure 5, have identical X-point and inner-midplane radii, and identical X-point height. The outer gap was scanned from 5 to 20 cm, in 5 cm increments. The increase in the outer gap from 5 to 20 cm increase the elongation from 2.55 to 2.95, and the aspect ratio from 1.71 to 1.81.

An example of configurations utilizing these boundary shapes, shown in figure 6, has $I_P = 1$ MA and $B_T = 1$ T, with each of the six NB sources injecting 2.1 MW of power for a total of 12.6 MW injected. These scenarios have $H_{98y,2} = 1$ and Greenwald fractions $f_{GW} = 0.72$, and are optimized to have a very high non-inductive fraction. The colours in the figure are a match to the requested boundary shapes in figure 5. The electron temperature is largely the same for these discharges, but the density increases for large outer gap (small minor radius) since $f_{GW} \propto \bar{n}_e a^2$ for fixed I_P. Also note that the 10 cm outer gap case is the S1 scenario of table 1.

Considering the current profile constituents, we see that the neutral-beam-driven current becomes progressively less

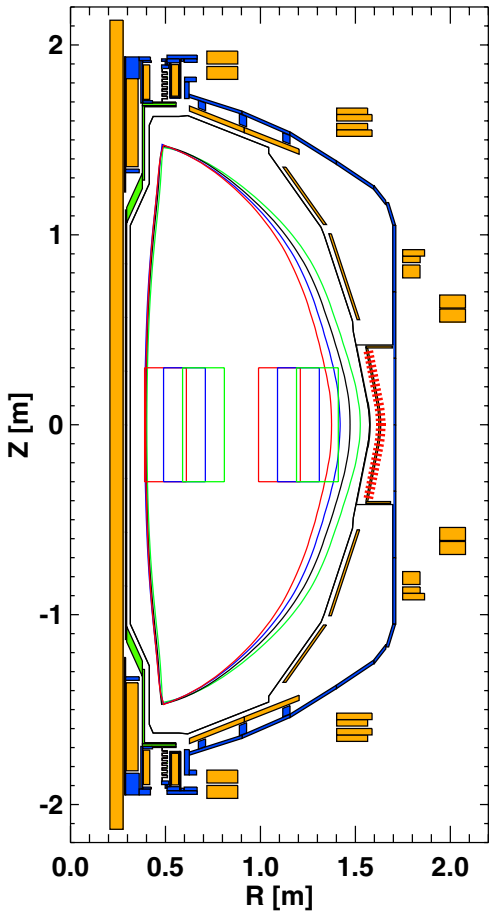

Figure 5. High-triangularity, double-null, target shapes used in the outer gap scan, as well as the NSTX-U vacuum vessel, HHFW antenna and coils. Also note the projections of the neutral beam footprints. The black outer contour represents the limiter boundary defined by the PFCs and HHFW antenna limiter.

peaked as the outer gap becomes larger. This is due to both the more tangential aiming of the outermost beams with the larger gap and the increased central density in this fixed f_{GW} example. The bootstrap current increases significantly for the larger outer gap, as the elongation is increased. The net result of these trends with increasing outer gap is to significantly reduce the residual ohmic current and significantly increase the central safety factor.

A similar set of trends is visible in figure 7, which studies a configuration optimized for high toroidal β. This is accomplished by operating at $I_P = 1200$ kA and $B_T = 0.55$ T. Four neutral beam sources with acceleration voltage of 90 kV are utilized, with $R_{tan} = [50, 60, 120, 130]$ cm. The 20 cm outer gap point is the scenario S3 from table 1. The omission of the centrally directed beams with $R_{tan} = 70$ and 110 cm is

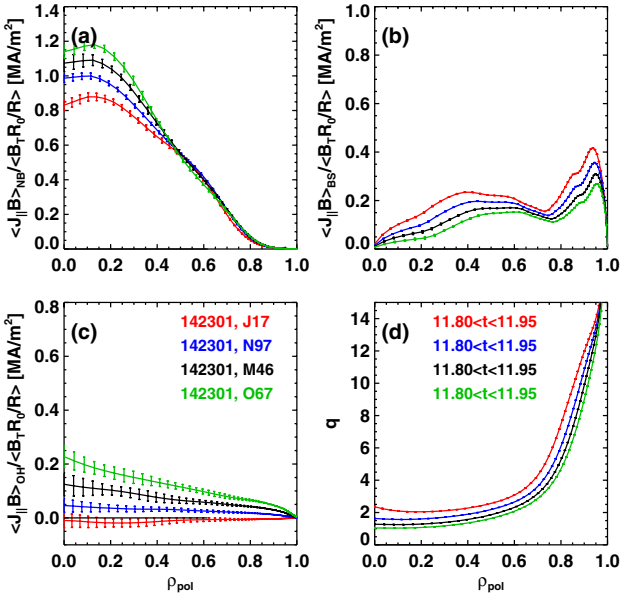

Figure 6. Variation of the current profile constituents with outer gap for a 12.6 MW near non-inductive configuration. These scenarios have $f_{GW} = 0.72$ and $H_{98y,2} = 1$, and the S1 scenario of table 1 is indicated in black.

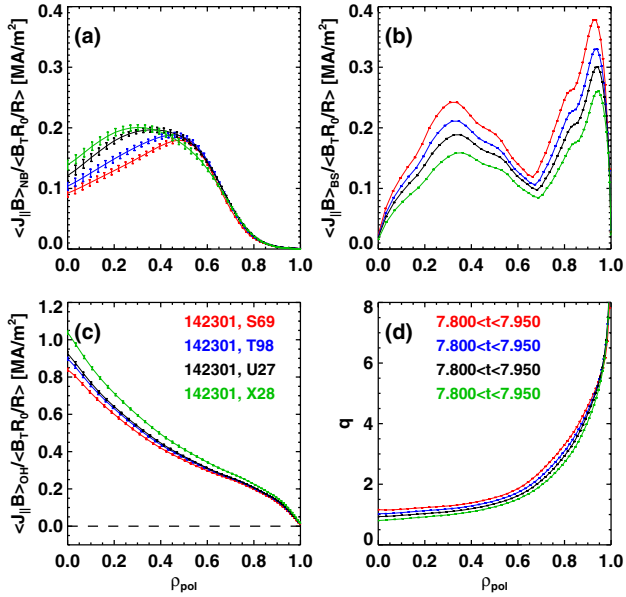

Figure 7. Variation in current profile constituents with outer gap for a $P_{inj} = 8.4$ MW, $B_T = 0.55$ T scenario designed to increase the sustainable β_T. These scenarios have $f_{GW} = 0.88$ and $H_{98y,2} = 1$, and the S3 scenario of table 1 is indicate in red.

critical in avoiding excessive NBCD on axis, which can drive down q_0 (the optimization of the source mix will be discussed in greater detail in later sections).

The effect of outer gap in these scenarios is quite similar to that in figure 6, despite the differences in the configuration. The NBCD profile is hollow in this case, with the peak in the driven current moving to successively larger radius as the outer gap is made larger, while the magnitude of the central current drive is reduced. Simultaneously, the bootstrap current increases as the outer gap is made larger and the elongation is increased. The inductive current on axis is thus reduced, though the effect is not as strong as in the previous example. The net effect is again to raise the central safety factor.

This dependence of q_{min} on the outer gap (for all other parameters fixed) is illustrated more clearly in figure 8(a). For the $I_P = 1.0$ MA, $B_T = 1.0$ T scan in red (see figure 6), the central safety factor drops from ~2 to 1.1 as the outer gap goes from 20 to 5 cm. The change in safety factor is less numerically dramatic, but perhaps more significant, in the $B_T = 0.55$ T case in blue, where $q_{min} > 1$ is only maintained for the largest outer gap. The maintenance of $q_{min} > 1$ is critical for the ST, so as to avoid the onset of non-resonant $m/n = 1/1$ kink modes, often coupled to 2/1 islands [36, 43, 44, 46, 116–119].

Figures 8(b)–(d) show the shine through, bad orbit, and charge exchange loss powers for the two configurations. A fixed edge neutral density of 5×10^{10} cm^{-3} is used in these calculations; this value of typical of that used in NSTX data analysis TRANSP runs. The shine-through power is small for the 5, 10 and 15 cm outer gaps, but becomes more significant for the 20 cm case. The bad-orbit loss is most significant for the small outer gap case, as the beams become effectively more perpendicular. This is somewhat compensated, however, by the reduction in charge exchange loss at small outer gap. Overall these studies indicate that the optimal outer gap is likely in the 10–15 cm range for most scenarios, with the 20 cm case having utility when further raising the minimum safety factor is a requirement.

5.2. *Importance of the plasma density and confinement level*

A second set of key variables impacting the scenario are the plasma density and confinement level. This is can be seen clearly in the left column of figure 9, where contours of the bootstrap fraction, NBCD fraction, total non-inductive fraction and q_{min} are plotted as a function of the Greenwald fraction and H-mode confinement multiplier $H_{98y,2}$, for fully evolved current profiles. The actual data points used in the calculation are shown as solid points, and the contours are an interpolation based on these points. This figure is for the S1 scenario with $B_T = 1.0$ T, $I_P = 1.0$ MA, $P_{NB} = 2.1$ MW from each of six NB sources (each at 90 kV for $P_{inj} = 12.6$ MW total power), and plasma boundary request with a 10 cm outer gap ($A = 1.73$ and $\kappa = 2.7$, corresponding to the black boundary in figure 5).

Contours of the bootstrap current fraction are shown in frame (a). In 0D analysis, the bootstrap fraction scales as $\sqrt{\varepsilon}\beta_P$, and so scales with the stored energy. Using the formulae in equations (1a) and (1b), we can write this dependence as roughly $Hn^{0.4}$ for either scaling expression. Thus, the bootstrap fraction increases with both variables in this figure, though more strongly with H. From figures 6 and 7, it is clear

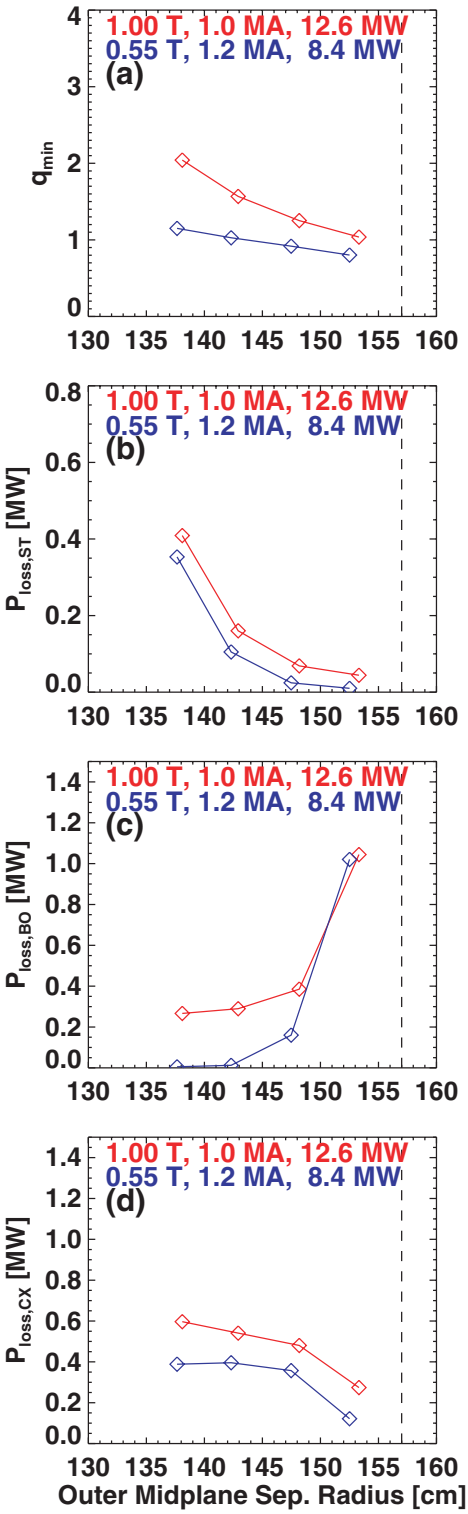

Figure 8. Variation of the (*a*) minimum safety factor, (*b*) the shine-through power, (*c*) the bad-orbit loss power and (*d*) the charge exchange loss power, as a function of the outer-midplane separatrix radius, for the scans in figures 6 and 7. The radius of the outboard limiter is shown as a vertical dashed line.

that increasing the bootstrap current will increase the amount of off-axis current, thus assisting in maintaining elevated $q_{\min}$.

The beam current drive fraction is shown in frame (*b*). The beam current drive scales as $(T_e^{3/2}/n_e)P$, where the leading ratio is a surrogate for the fast-ion slowing down time. Using $W = nT$, $W = HP\tau_{\text{scaling}}$ and $\tau_{\text{scaling}} \propto \sqrt{n_e}$ for either scaling expression, we can calculate that to lowest order, $f_{\text{NBCD}} \propto f_{\text{GW}}^{-2} H^{3/2}$. Hence, we see a strong inverse dependence of the beam current drive fraction on the density, and a positive dependence on the confinement multiplier (note that this scaling expression neglects variations in the beam penetration and deposition with density).

The net non-inductive fraction is shown in figure 9(*c*). This is the sum of the beam driven currents, bootstrap current, and the Pfirsch–Schlüter and diamagnetic currents. Interestingly, the total non-inductive current is roughly independent of the density for the range of densities and confinement assumptions considered here. For instance, increasing the density will decrease the NBCD, but increase the bootstrap current. A similar regime of non-inductive fraction independent of density was noted before, for instance, in [81]. This configuration is 100% non-inductive at $H_{98y,2} \approx 1.04$ for the considered range of density.

The central safety factor, shown in figure 9(*d*), is, however, not independent of the plasma density. Rather, reducing the density at fixed $H_{98y,2}$ tends to rapidly lower the central safety factor, as the central NBCD drives down $q_{\min}$. As noted above, maintaining $q_{\min} > 1$ is critical for the avoidance of $n = 1$ kink and coupled core/kink tearing modes. Hence, this trend in $q_{\min}$ provides a low-density limit for scenarios with fully relaxed current profiles.

Finally, a few comments are in order to provide context to this result of low $q_{\min}$ at low density. First, the higher T_e at lower density may assist in *transiently* assessing scenarios with lower density and $q_{\min} > 1$, as the current penetration will be slowed. This will enable a wide range of physics studies in discharge scenarios that may not relax to $q_{\min} > 1$. However, time dependent simulations that can accurately model the shape and profile evolution during the current ramp and early flat-top are out of scope for this work, which has focused on fully relaxed scenarios. Second, in next step STs, a larger fraction of the NBCD will likely be directed off-axis. This should result in $q_{\min} > 1$ for a much wider range of densities than in the present NSTX-U design.

5.3. *Impact of anomalous fast-ion diffusivity*

Because the neutral beams provide a substantial fraction of the current drive, it is worth considering what the effect of non-classical fast-ion diffusion would be on these scenarios. Possible sources of fast-ion diffusion include the underlying plasma turbulence [120–124], or, more likely for NSTX-Upgrade, modifications to the NBCD from energetic particle driven MHD.

We have generally found that in the absence of low-frequency MHD activity, the beam current drive appears to be classical [36, 43]. However, [43] shows that even in these MHD-quiescent cases, fast-ion diffusivities of up to $\sim 1\,\text{m}^2\,\text{s}^{-1}$ cannot be excluded. Reference [43] also analyses a discharge with rapid toroidal Alfvén eigenmode (TAE) avalanches [31, 32, 34, 35]. The avalanches are modelled with bursts of fast-ion diffusivity, with peak values of $\sim 50\,\text{m}^2\,\text{s}^{-1}$, but durations of typically 0.5–1.0 ms. This allows a match to both the typical neutron emission evolution over the avalanche

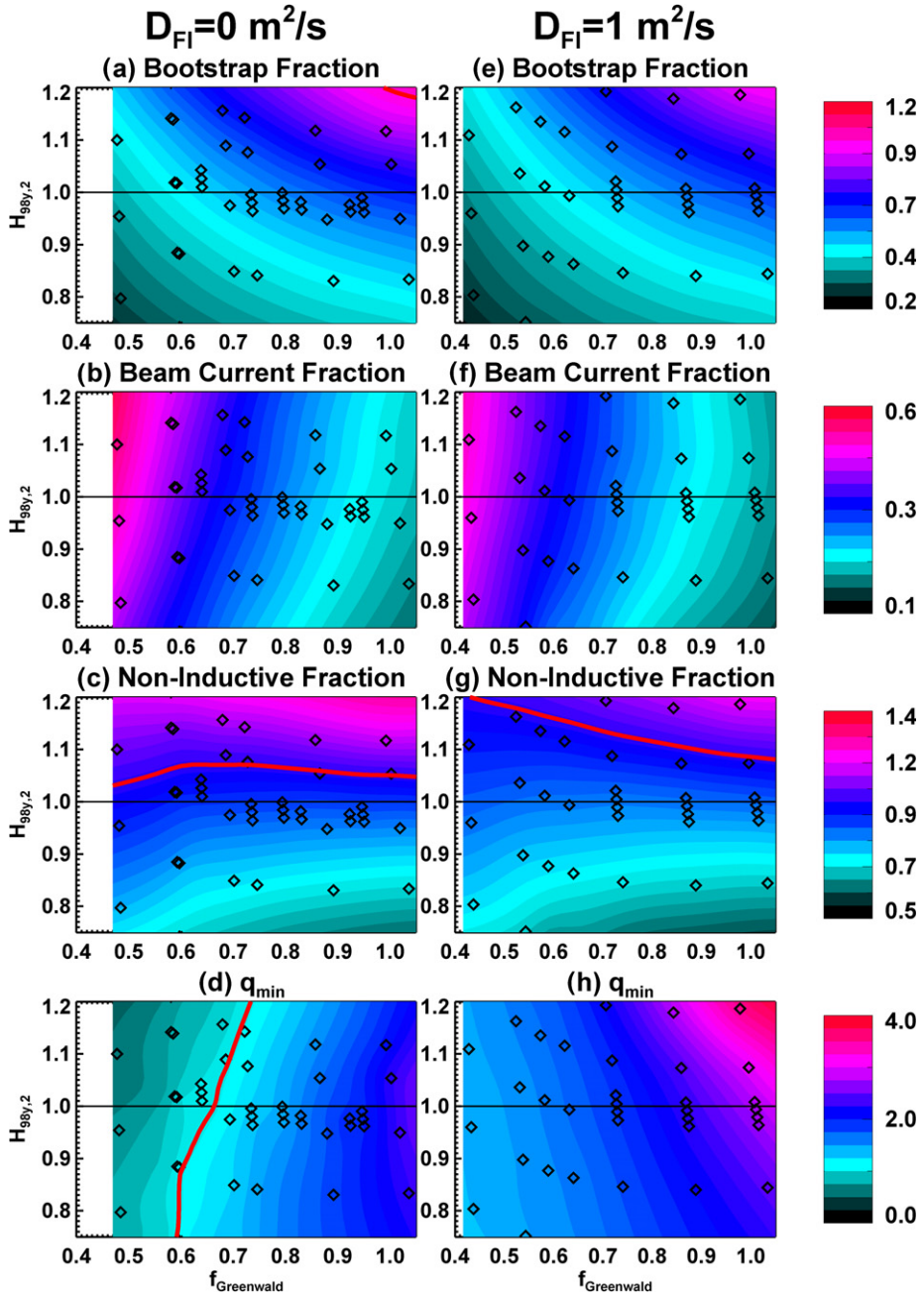

Figure 9. Comparison of the nearly 100% non-inductive S1 scenario without (left) and with (right) anomalous fast-ion diffusion. The rows show the bootstrap fraction, NB current fraction, the total non-inductive fraction and the minimum safety factor. The red lines corresponds to a bootstrap fraction of 1.0 in (*a*), a non-inductive fraction of 1.0 in frames (*c*) and (*g*), and $q_{\min}$ of 1.0 in (*d*).

and the average profile of neutral-beam-driven current drive. As part of this study, that discharge was analysed to determine a single spatially and temporally constant diffusion coefficient that would match the average neutron emission and current profile. It turns out that $D_{\rm FI} = 4\,{\rm m}^2\,{\rm s}^{-1}$ can achieve this match, and this value will be used below as what might be, on average, typical of a discharge with these modes.

To begin these studies, we have made calculations with a spatially uniform 'anomalous' fast-ion diffusivity $D_{\rm FI} = 1\,{\rm m}^2\,{\rm s}^{-1}$ for the S1 scenario with $B_{\rm T} = 1\,{\rm T}$, $I_{\rm P} = 1\,{\rm MA}$, $P_{\rm inj} = 12.6\,{\rm MW}$. The results of this calculation are shown in the right-hand column of figure 9; all other parameters are the same as in the left column. The bootstrap fraction in frames (*a*) and (*e*) is essentially the same. The beam current drive is reduced a meaningful amount on the low-density left-hand side of the plot, but less on the high-density right-hand side. Overall, the total non-inductive fraction for $H_{98y,2} = 1$ and this range of densities is decreased by 5–10% with $D_{\rm FI} = 1\,{\rm m}^2\,{\rm s}^{-1}$; the inclusion of $D_{\rm FI}$ also changes the previous trend of $f_{\rm NI}$ independence from density, since the NBCD can no longer compensate for the reduced bootstrap current at lower density. There is also a significant increase in the central safety factor when the fast-ion diffusivity is invoked, due to the reduction in central NBCD. Over the range of densities and confinement

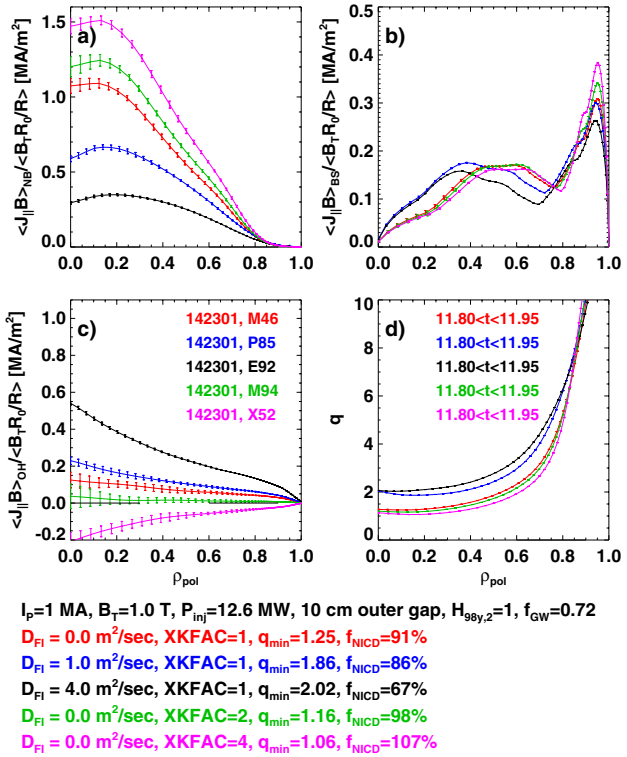

Figure 10. Profile comparison for the S1 scenario with $B_T = 1.0$ T, $I_P = 1$ MA, $H_{98y,2} = 1$, with a 10 cm outer gap. The injected power is from six sources operating at 90 kV, for a total power of 12.6 MW, and the Greenwald fraction is $f_{GW} = 0.72$. The different curves correspond to various levels of spatially uniform fast-ion diffusivity D_{FI} or multiplier XKFAC on the ion thermal diffusivity.

considered in figure 9(*h*), q_{min} is maintained greater than 1 for $D_{FI} = 1\,m^2\,s^{-1}$, compared with a significant region with $q_{min} < 1$ for $D_{FI} = 0\,m^2\,s^{-1}$ in figure 9(*d*).

The reasons for this elevated central safety factor are shown more clearly in figure 10, where profiles for $H_{98y,2} = 1$, $f_{GW} = 0.72$ scenarios are shown with various levels of fast-ion diffusivity. We see that for $D_{FI} = 0$ (the case in red), there is a highly peaked beam current drive profile. The central beam-driven current density is approximately 10 times larger than the ohmic current in this case, and has a significantly more narrow profile. Increasing D_{FI} to values of 1.0 and then $4.0\,m^2\,s^{-1}$ (black and blue curves) results in a significant reduction of the central beam drive current, with the central parallel current density reduced by more than a factor of 2. There is some increase in the core bootstrap current as the central safety factor is increased [77], and some reduction of the edge bootstrap current. However, most of the lost NBCD is replaced with ohmic current. The ohmic current profile is significantly broader than the NBCD profile, and the net effect is to raise the central safety factor.

Figure 11 shows select parameters as a function of this spatially and temporally uniform fast-ion diffusion coefficient. The grey region on the left indicates the range of D_{FI} that is consistent with MHD-quiescent discharges [43], while the grey region on the right represents the TAE avalanche case. The S1 scenario ($I_P = 1.0$ MA, $B_T = 1.0$ T, $P_{inj} = 12.6$ MW) considered so far in this section is indicated by solid lines and diamond symbols. Figure 11(*a*) illustrates that the total

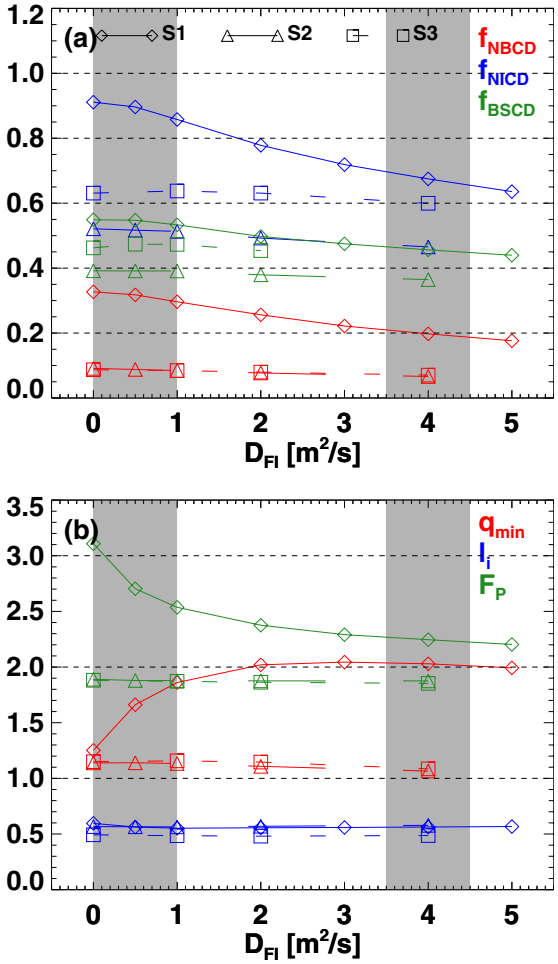

Figure 11. Various parameters as a function of the spatially and temporally constant fast-ion diffusion coefficient. The diamonds are for the S1 scenario with $B_T = 1$ T, $I_P = 1$ MA and $f_{GW} = 0.72$, the triangles are for the S2 scenario with 1.6 MA, 1.0 T, and $f_{GW} = 0.72$, and the squares are for the S3 scenario with 1.2 MA, 0.55 T and $f_{GW} = 0.86$. See text for additional details.

non-inductive fraction drops from ~91% to 65% as the fast-ion diffusivity is increased. The majority of this loss is due to the reduced beam current drive, although there is also some loss of bootstrap current.

Figure 11(*b*) shows some additional equilibrium parameters plotted against this same fast-ion diffusion coefficient. We define the pressure peaking factor F_P as the central total pressure normalized to the volume-average total pressure. The pressure peaking factor decreases substantially as the centrally peaked fast-ion pressure is reduced; the central safety factor increases rapidly over the same range of D_{FI}. The internal inductance decreases slightly over the scan, as the centrally peaked beam current is replaced by the broader inductive current.

The profile changes that result from even the rather small value of $D_{FI} = 1\,m^2\,s^{-1}$ are generally beneficial to the ideal $n = 1$ stability of the configuration, as shown in figure 12; this figure is based on the same TRANSP calculations as in figure 9. The left column of plots shows the parameters for $D_{FI} = 0$, while the right columns is for $D_{FI} = 1\,m^2\,s^{-1}$. The top row shows the value of β_N, while the second row shows the pressure

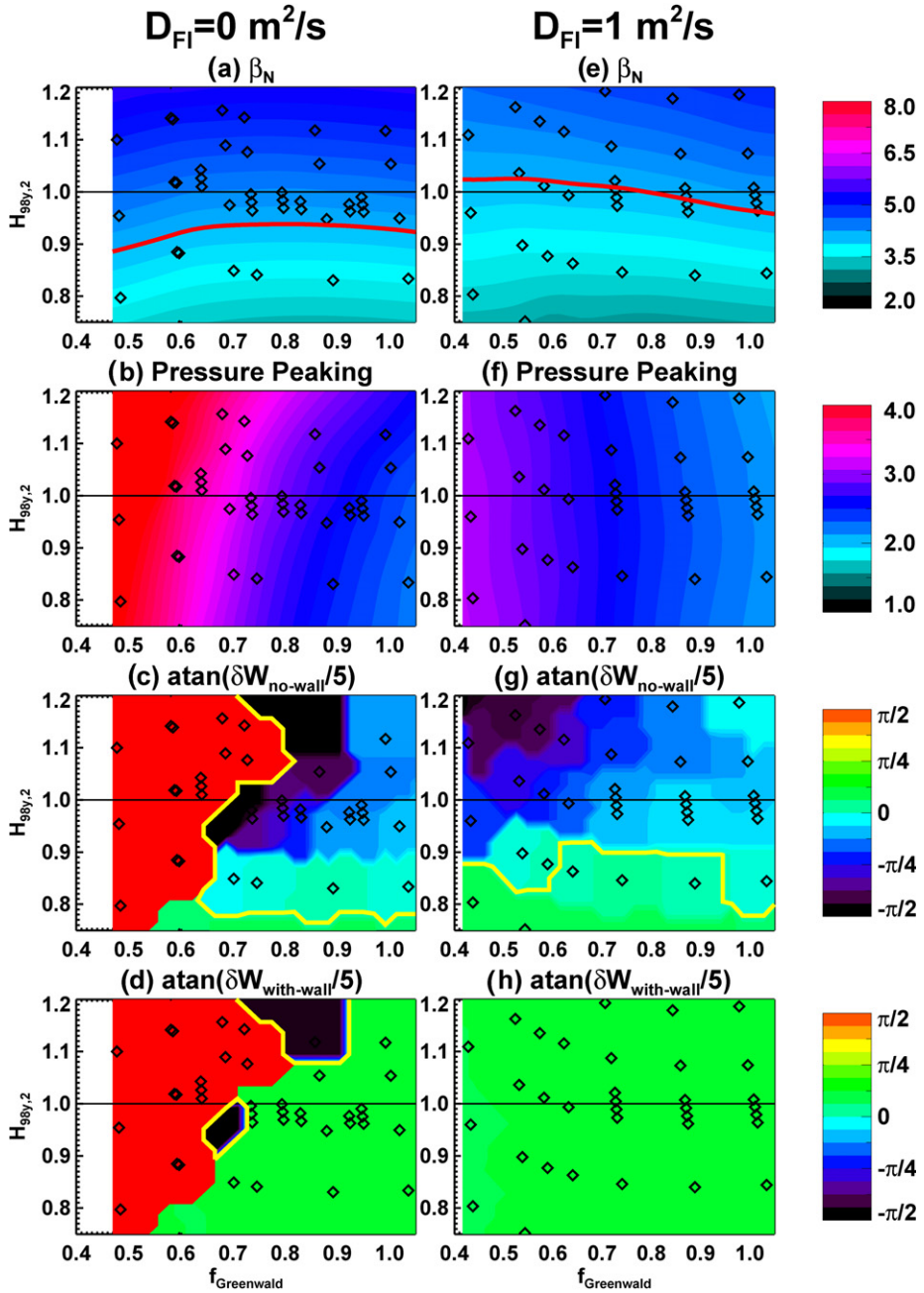

Figure 12. Stability-related parameters as a function of the confinement multiplier and Greenwald fraction. Shown are (*a*), (*e*): β_N, (*b*), (*f*): the total pressure peaking factor, (*c*), (*g*) the no-wall $n = 1$ stability parameter and (*d*), (*i*) the with-wall $n = 1$ stability parameter. The dark red colours for the stability plots correspond to internal modes becoming unstable. The red lines in frames (*a*) and (*e*) correspond to the $\beta_N = 4$ contour, while the yellow lines in frames (*c*) and (*d*) indicate the stability boundary. This figure is based on the same TRANSP runs as in figure 9.

peaking factor, both as a function of confinement multiplier and Greenwald fraction. It is clear that the normalized β is similar between the two cases, but that the total pressure peaking is significantly reduced at lower density when $D_{FI} \neq 0$. This reduction in pressure peaking is well known to have beneficial effects on the global ideal stability [44, 76, 125–133].

The effects of these profile modifications on the global stability are shown in the bottom two rows of figure 12. These frames show contours of a stability parameter atan($\delta W/5$), where δW is computed with DCON as described in section 3.3. The atan here is used to bound data, as the quantity δW can become very negative for strongly unstable configurations, causing a contour plot of δW itself to be difficult to interpret; the use of the atan compresses the data, while maintaining the rule that atan($\delta W/5$) > 0 is indicative of stability. DCON also predicts when purely internal modes are unstable, and these cases are shown in bright red in the figures.

Figure 12(*c*) shows contours of the stability parameter for the case with $D_{FI} = 0\,m^2\,s^{-1}$. The left side of the frame is dominated by internal instabilities due to the central safety factor becoming too low. The right side of the plot is found to be unstable to external modes for $H_{98,2} > 0.7$. The inclusion

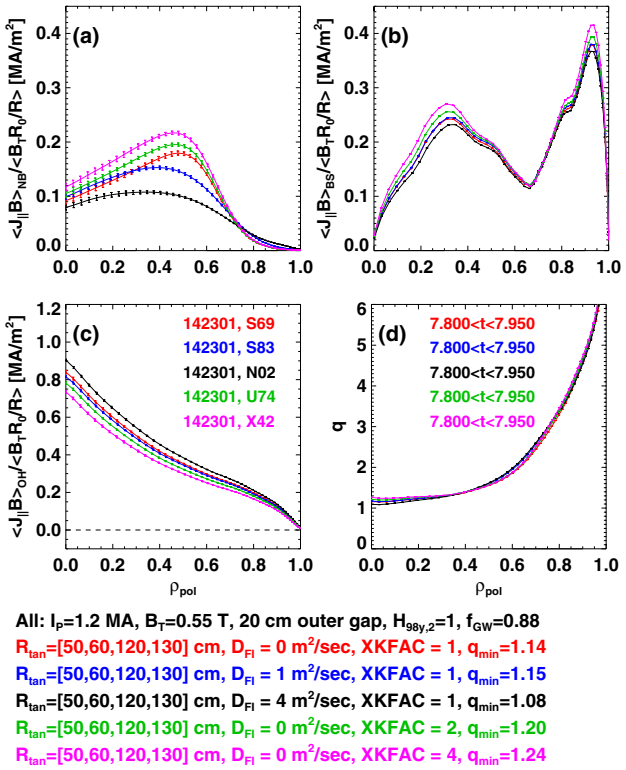

Figure 13. Example profiles for the S3 scenario with $B_T = 0.55$ T, $I_P = 1200$ kA, designed for maximizing the sustained β_T with four sources and 8.4 MW of input power. The different cases correspond to different assumptions on the fast-ion diffusivity and ion thermal transport.

of a superconducting wall changes the results as shown in figure 12(*d*). The internal modes at lower density are not modified by the addition of the wall. A stability window does open at higher density, though it appears to be somewhat limited by the large pressure peaking factor.

Figure 12(*g*) shows the no-wall stability for the case with $D_{FI} = 1\,m^2\,s^{-1}$. The increased central safety factor leads to an immediate improvement of the global stability, with the internal modes totally eliminated over this range of densities and confinement. However, confinement multipliers greater than $H_{98y,2} \sim 0.9$ lead to unstable external modes in the absence of a conducting wall. As shown in figure 12(*h*), these external modes can be eliminated by the conducting wall, and robust $n = 1$ ideal stability is predicted over this operating range.

Of course, when the value of β_N exceeds the no-wall limit, but is less than the with-wall limit, then the configuration is in the wall-stabilized regime [134, 135] where the resistive wall mode [136, 137] can be a performance limiting instability. Indeed, NSTX has observed and documented many features of the RWM stability in a ST [41, 131, 138–144]. Calculations of the resistive wall mode stability is not within the scope of the paper. However, we note that by sustaining the rotation with error-field correction [41, 42] and avoiding the RWM with fast $n = 1$ feedback [140, 143, 144], reliable operation in the wall-stabilized regime has been achieved.

The effect of additional fast-ion diffusivity on the S3 scenario is shown in figure 13; recall that S3 is the $B_T = 0.55$ T, $I_P = 1.2$ MA, $P_{inj} = 8.4$ MW scenario designed to study fully relaxed high toroidal β scenarios. The case with $D_{FI} = 0\,m^2\,s^{-1}$ in red has a hollow beam drive current profile, with the peak at $\rho \sim 0.5$ and the magnitude of the central value approximately half that of the peak (this case was also shown in figure 7). Imposing $D_{FI} = 1\,m^2\,s^{-1}$ (blue curve) actually raises the central current drive, while decreasing the midradius peak. $D_{FI} = 4\,m^2\,s^{-1}$ results in a significant drop in the core NB current drive (black curve), but a noticeable increase in the outer half of the plasma. Overall the minimum safety factor drops at D_{FI} is increased, but only from 1.14 to 1.08, with a slightly non-monotonic behaviour near $D_{FI} = 1\,m^2\,s^{-1}$.

These trends are illustrated with the squares and dotted lines in figure 11. Frame (*a*) shows that the non-inductive current drive components are largely independent of D_{FI} in this scenario. Furthermore, frame (*b*) shows that the variations in pressure peaking, q_{min}, and l_i are quite small.

Figure 11 also shows, with triangles and dashed lines, the impact of fast-ion diffusivity on the partial-inductive, long-pulse S2 scenario, with $I_P = 1600$ kA, $B_T = 1.0$ T, and six sources injecting with an acceleration voltage of 80 kV. This scenario is ~55% non-inductive at $D_{FI} = 0$, mostly from the bootstrap current. Hence, the current-drive components in this type of scenario are largely independent of the chosen D_{FI}. Similarly, the global parameters l_i and F_P, as well as the minimum safety factor, are largely independent of the fast-ion diffusivity at the levels studied.

It should be noted that fast-particle MHD, and the associated loss of fast particles, can be quite deleterious to scenarios even if they do not significantly impact the current drive. For instance, fishbone modes have been observed to trigger NTMs [117, 145] and RWMs [146], the latter presumably due to the loss of fast-particle stabilization [147–151]. Hence, it is likely necessary to develop operating regimes that are free of fishbones and TAE avalanches.

Finally, we note that there is some experimental evidence for the reduction of EPM and TAE activity as β_T is increased [28, 30], along with some theoretical expectations why this should be the case [28]; one might thus surmise that simulations with non-zero D_{FI} would be unwarranted at higher β_T. The cases shown in figure 9 generally have β_T in the range 8–12%, in the range where EPMs have been observed in MAST and START [28]. The NSTX experimental example described in [43] shows large fast-particle-driven modes at $\beta_T \sim 10\%$ that contribute to the modification of the current profile. Hence, we consider that these near non-inductive scenarios, such as the S1 scenario in this section, may indeed be susceptible to these modes. The higher β_T case scenario S3 discussed here and in greater detail in section 6.4 has β_T above the level where TAEs and EPMs have been observed in MAST and START. However, as described in [29, 32], these fast-ion instabilities have been observed in nearly all regimes of NSTX operation, including the very high β_T regime noted in [29]. We thus consider it appropriate to consider the effect of these modes on the high-β_T scenarios as well.

5.4. Impact of electron temperature variations at fixed global thermal confinement

Even when fixing the global confinement to have $H_{98y,2} = 1$, various values of the electron temperature are possible. For

instance, changes to the ion thermal transport level or plasma impurity content will result in modifications to T_e if the global confinement, and thus stored energy, are held fixed. This subsection discusses these two variations, using the profiles from high aspect-ratio discharge 142301.

We begin this study by changing the ion thermal transport. An example calculation is shown in figure 10, where the thermal ion diffusivity in increased by a factors of 2 and 4; these are denoted by XKFAC = 2 and XKFAC = 4 in the legend, and should be compared with the XKFAC= 1 curve in red. We see that increasing this multiplier results in an increase in the centrally peaked NB current drive profile. The fundamental reason for this is that fixing the overall confinement to match a scaling expectation will result in a fixed stored energy. If the ion transport is increased and the ion temperature decreases, the electron temperature must increase to compensate. This higher T_e then increases the NB current drive efficiency. The increased NB currents result in a decrease in the inductive current component, so that fully non-inductive or overdriven scenarios occur at high values of this ion confinement multiplier. However, this increased central NB current also drives down the central safety factor, with the XKFAC = 4 case perilously close to $q_{min} = 1$.

Similar trends with XKFAC are observed in figure 13, for the high-β_T S3 scenario. The beam current drive increases significantly at XKFAC is increases, leading to a significant drop in the inductive currents (compare the red curve with green and magenta). Given the hollow NB current profile, these trends result in the central safety factor increasing. This will tend to improve the global stability of the configuration.

Selected parameters are shown directly as a function of this multiplier in figure 14. The symbols and linestyles are the same as in figure 11 and are described in table 1. The near non-inductive S1 scenario with 1 MA, 1 T, P_{inj} = 12.6 MW case is illustrated by solid lines and diamonds. As noted above, this case has a non-inductive fraction of 91% with ion neoclassical thermal transport. Artificially increasing the ion thermal transport by a factor of ~2.3 at fixed $H_{98y,2} = 1$ yields fully non-inductive operation, as evidenced by the non-inductive fraction plot in frame (*a*) and the surface voltage in frame (*c*). Increasing the neoclassical ion transport by a full factor of 4 results in significant non-inductive overdrive. The ratio T_e/T_i goes from 0.6 with neoclassical ion transport, to above unity at the highest neoclassical multipliers considered.

The behaviour of the partial-inductive S2 and S3 scenarios is also illustrated in figure 14, and shows similar trends. The non-inductive fraction increases with the ion thermal transport multiplier, mainly due to increases in the bootstrap current (the NBCD is small in these cases). The ratio T_e/T_i increases by the same factor of ~1.5–1.8, and the surface voltage is reduced. Again, we emphasize that these model results are driven by the assumption of fixed ion thermal transport and global 0D confinement scaling, and may change if a validated model for electron transport were utilized.

The second variation to be considered is that of $Z_{eff} = (n_D Z_D^2 + n_C Z_C^2)/n_e$, where the subscript D and C refer to deuterium and carbon (the latter assumed to be the only impurity present due to the graphite PFCs in NSTX-U). The value of Z_{eff} can change the scenario, for instance, through collisionality effects on the bootstrap current and neoclassical

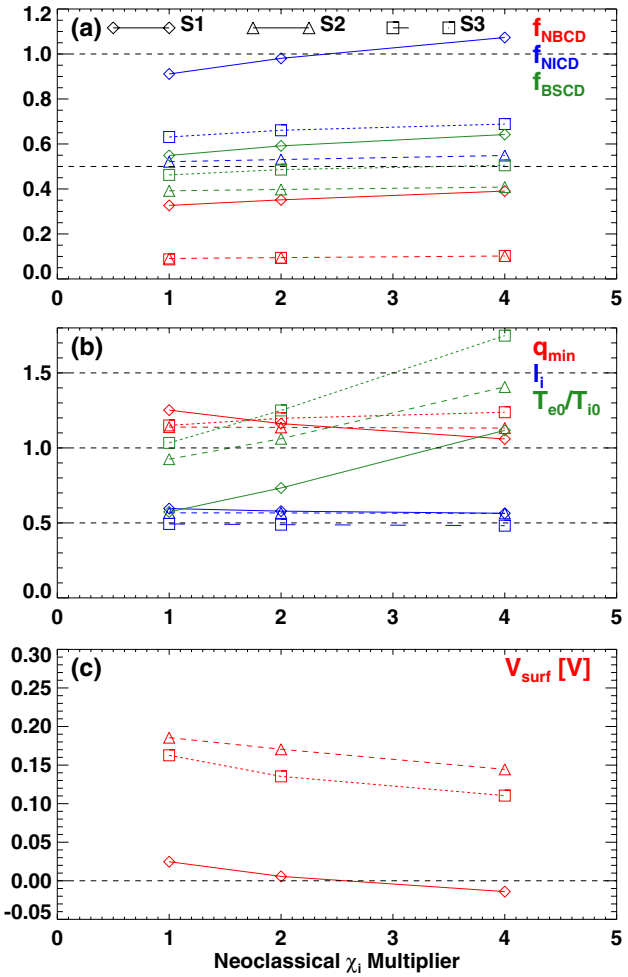

Figure 14. Variation of selected quantities as a function of the multiplier on the ion neoclassical thermal diffusion coefficient, for fixed overall thermal confinement. The symbols and linetypes correspond to the same discharge scenarios as in figure 11 and are explained in detail in table 1. See text for additional details.

resistivity [63] or the neutral beam current shielding factor [65, 66]. However, the assumption utilized here of following a given global confinement expression will somewhat modify the expectations from current drive theory alone. In particular, increasing Z_{eff} at fixed temperatures results in a decrease of the stored energy, as the deuterons are diluted. Hence, the plasma temperatures must increase with Z_{eff} if the global confinement is to be maintained. We emphasize that this is not a physics result, but rather the unavoidable consequence of using a 0D scaling assumption to set the temperature profile instead of a complete transport model.

With this caveat, the trends with Z_{eff} for the S1–S3 scenarios are shown in figure 15. The non-inductive current drive tends to be constant or increase slightly as Z_{eff} is increased. The beam driven currents provide the slight increase in the S1 scenario, with the bootstrap currents largely constant. The central electron temperature is shown in frame (*b*), and shows a significant increase in order to maintain constant global confinement. The minimum safety factor shows a slight increase with Z_{eff}, except for the S1 scenario, where is decreases and then flattens. The internal inductance is largely unchanged. For these reasons, we infer that the scenarios are

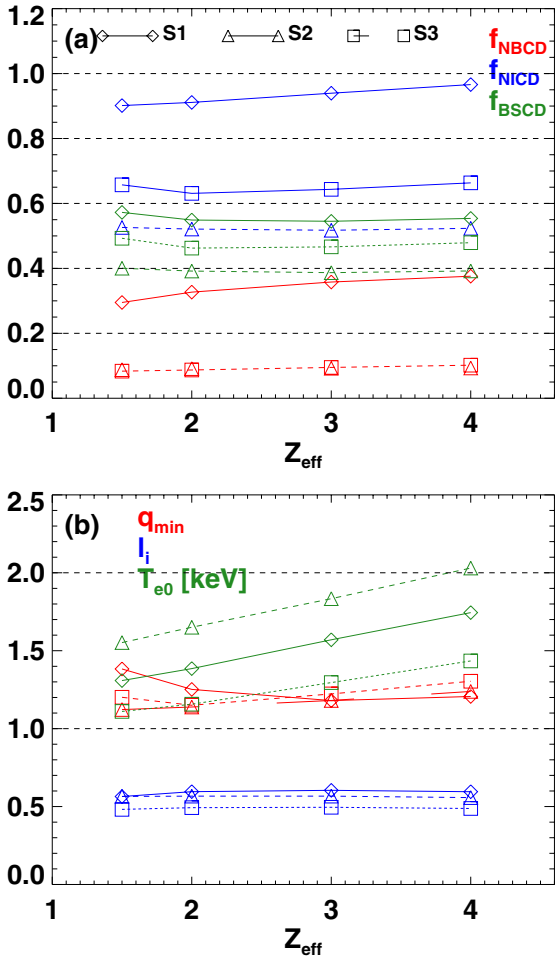

Figure 15. Variation of selected quantities as a function of $Z_{\rm eff}$, for fixed global confinement given by $H_{98y,2} = 1$. The symbols and linetypes correspond to the same discharge scenarios as in figure 11 and are explained in detail in table 1. See text for additional details.

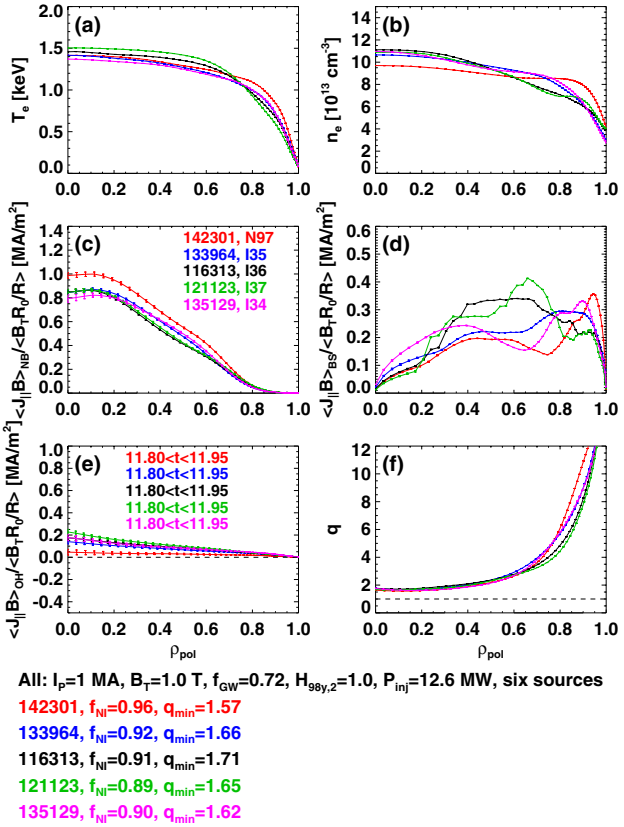

Figure 16. Examples of how various thermal density and temperature profile shapes impact the current profile constituents and non-inductive current level for the near non-inductive S1 scenario, for fixed $I_{\rm P}$, $B_{\rm T}$, H_{98y}, $f_{\rm GW}$, and neutral beam configuration.

largely insensitive to variations in $Z_{\rm eff}$ around the $Z_{\rm eff} = 2$ operating point assumed in this paper, provided the global confinement is not degraded with changes in $Z_{\rm eff}$.

5.5. Impact of variations in the H-mode thermal profile shape

The final sensitivity study to be completed here is with regard to the impact of various H-mode profile shape assumptions on these scenarios. We begin this study in figure 16 with the S1 scenario, which had with $I_{\rm P} = 1$ MA, $B_{\rm T} = 1.0$ T, and all six available sources injecting at 90 kV, for a total input power of 12.6 MW. However, this figure is for slightly higher elongation (2.8 instead of 2.7), and aspect ratio (1.75 instead of 1.73) that used previously. As noted in section 5.1, this change will tend to increase the non-inductive fraction. The confinement level is specified by $H_{98y,2} = 1$ for all cases, and the Greenwald fraction is ∼0.71.

With regard to non-inductive fraction, we observe that the preferred profiles are those from discharge 142301 in red, with a non-inductive fraction of 96%. This case has comparatively broad density and temperature profiles, and will be referred to below in this context. Note that these profiles were taken from a high aspect-ratio discharge designed to prototype NSTX-Upgrade operation [44]. The profiles from discharge 121123 are least favourable, in the sense of having the lowest non-inductive fraction for the given confinement multiplier $H_{98y,2} = 1$. Furthermore, the rather peaked temperature profile results in the relaxed ohmic current density profile becoming more peaked than other cases, which tends to drive down the central safety factor. This set of profiles will be referred to as 'peaked' in the discussion below.

We repeat this exercise in figure 17, for the high $\beta_{\rm T}$ S3 scenario at $I_{\rm P} = 1.2$ MA and $B_{\rm T} = 0.55$ T, and $P_{\rm inj} = 8.4$ MW from the $R_{\rm tan} = [50, 60, 120, 130]$ cm sources. The primary optimization in this high-current scenario is to increase the minimum safety factor. As with the near non-inductive cases described in figure 16, the profiles from discharge 142301 result in the largest value of $q_{\rm min}$. Furthermore, the profiles from 121123 result in the lowest value of $q_{\rm min}$, due to the peaking of the temperature and density profiles.

These results are summarized in figure 18, which shows various parameters as a function of the thermal profile peaking factor for the S1, S2 and S3 scenarios; this quantity has been shown to be a useful means of parametrizing profile shapes for non-inductive current calculations in DIII-D [77]. In frame (*a*), there is a clear drop in the central safety factor with pressure peaking for the S2 and S3 cases, and a clear increase in the internal inductance for all three scenarios. The non-inductive current fraction in frame (*b*) drops by 5–10% as the pressure peaking is increased, with the change mainly

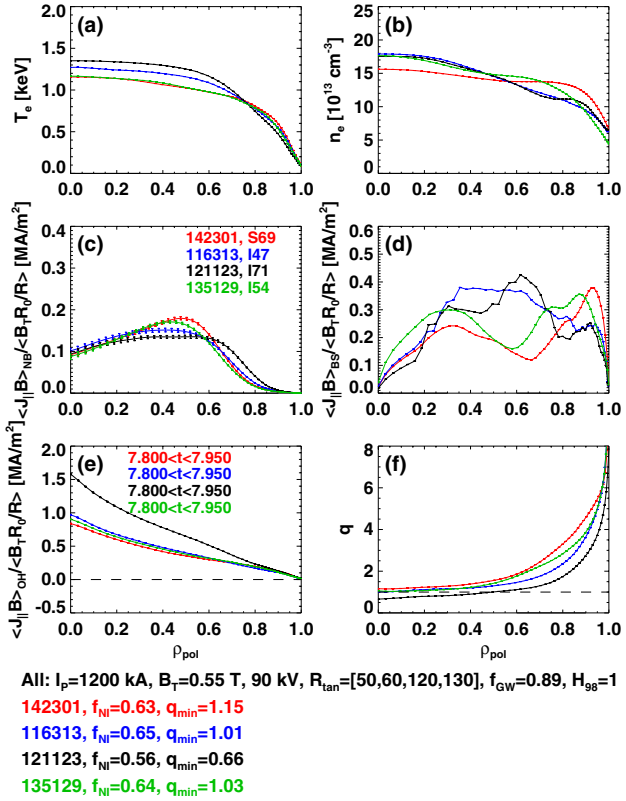

Figure 17. Effect of the various profile shape assumptions on the high-β_T scenario S3 for fixed I_P, B_T, H_{98y}, f_{GW}, and neutral beam configuration.

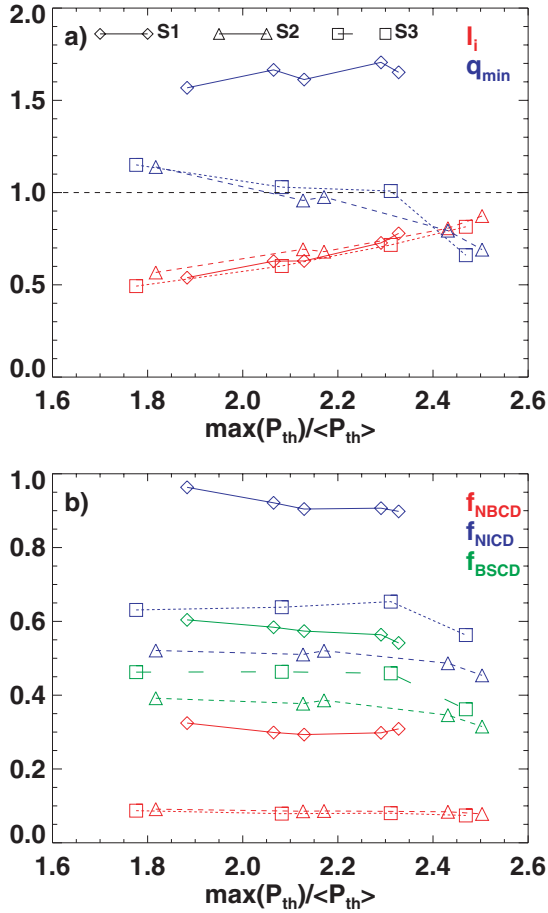

Figure 18. Various parameters as a function of the thermal pressure peaking factor, for the S1–S3 scenarios of table 1. Frame (*a*) shows the internal inductance and minimum safety factor, while frame (*b*) shows the non-inductive current components.

due to a reduction in the bootstrap current. The beam-driven current magnitude is largely independent of the thermal profile peaking for these scenarios. Given these results, we will use the profiles shapes from discharges 142301 (most broad) and 121123 (most narrow) to provide bounds on the performance in sections 6 and 7.

5.6. Summary of parametric dependences for scenario design

The results of these studies indicate the general trends that will be exploited below. In general, the desirable scenarios will have large outer gaps in order to maintain an elevated central safety factor. We will use 15 cm outer gaps for most of the studies described below. The exception will be the high β_T optimization at $B_T = 0.55$ T, where a 20 cm outer gap will be used.

The scenarios will also generally optimize to higher Greenwald fractions. Below, we will generally focus on cases with $0.7 < f_{GW} < 0.75$, though we will also consider some cases with higher values. These latter will be important when trying to keep the central safety factor elevated at very high plasma currents, as the high densities favour the bootstrap current, which goes to zero on the magnetic axis.

With regard to anomalous fast-ion diffusion, some scenarios are considerably more sensitive than others. The near non-inductive scenario with highly peaked fast-ion current (S1) appears to be quite sensitive to the imposed D_{FI}, with $D_{FI} = 1\ m^2\ s^{-1}$ having a major impact on the equilibrium and stability. The partial-inductive scenarios (S2 and S3), however, have a broader fast-ion current profile and a smaller fraction of the total current driven by those ions. These scenarios are not significantly affected by this level of fast-ion diffusivity.

The effects of scanning the ion transport level and Z_{eff} with fixed global confinement were studied in section 5.4. Increasing the ion thermal transport, or equivalently, the ratio T_e/T_i, was found to be beneficial for the configurations: the required inductive voltage dropped and the non-inductive fraction increased. The configurations were largely insensitive to changes in Z_{eff}, provided that the global transport is fixed. All simulations below will utilize $Z_{eff} = 2$, and ion thermal transport given by neoclassical theory without additional multiplier.

Finally, the profiles from the discharges 142301 and 121123 were picked as bounding the performance for all other parameters fixed. These tend to differ in their non-inductive current fraction of ~10%, but to have larger variations in the central safety factor. These two sets of profiles will be used in the studies in the following two sections.

6. Scenario optimizations for different physics studies

As noted in the introduction, this section addresses a number of important scenarios for NSTX-Upgrade that support the physics program.

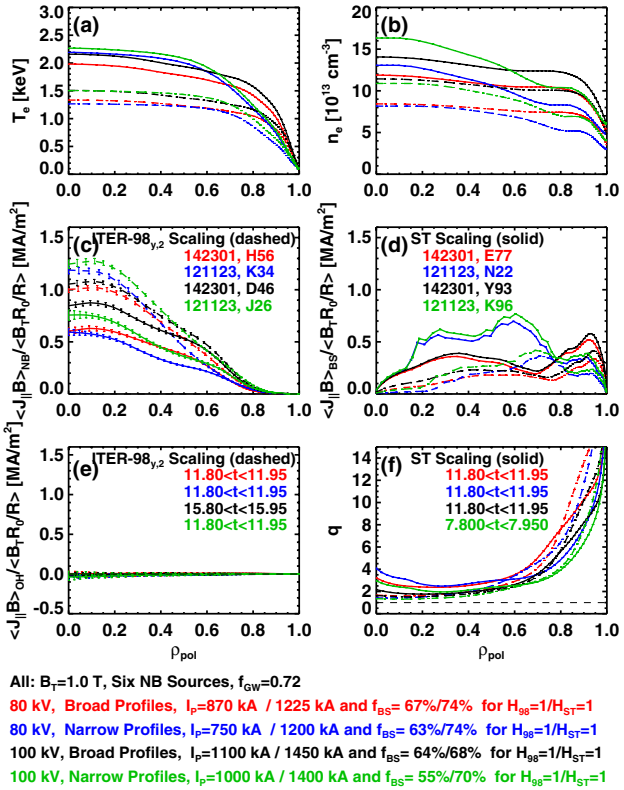

Figure 19. Example 100% non-inductive scenarios under different confinement and profile assumptions. Shown in this and similar figures are profiles of (*a*) the electron temperature, (*b*) the electron density, (*c*) the beam-drive current, (*d*) the bootstrap current, (*e*) the ohmic current and (*f*) the safety factor. The solid curves show the expectations assuming $H_{ST} = 1$ governs the confinement; the dashed curves are for $H_{98y,2} = 1$. See caption and text for further details of the different scenarios.

6.1. High-current 100% non-inductive scenarios at $B_T = 1.0$ T and 0.75 T

A major goal of the NSTX-U project is to demonstrate stationary 100% non-inductive operation, using pressure and neutral beam driven currents to sustain the configuration. In this section we explore 100% non-inductive current capability at $B_T = 1.0$ and 0.75 T, using various levels of acceleration voltages for the beam sources.

Figure 19 presents calculations of fully non-inductive operating points, in a format that will be common for many figures in the remainder of this paper. The content of the individual frames is the same as figures 16 and 17. Each colour represents a given configuration, where configuration refers to the boundary shape, heating power, TF and Greenwald fraction. The solid line corresponds to $H_{ST} = 1$ and the dashed line indicates the result with $H_{98y,2} = 1$. The data in this figure have $B_T = 1$ T, and utilize the 15 cm outer gap shape. Note that the ohmic current profiles in frame (*e*) are all flat and equal to zero, verifying that these scenarios would not require any inductive current (though we note that having the solenoid continue to help regulate the plasma current level against confinement transients could be advantageous for the stability of the configuration, as discussed in [152]).

The red curves correspond to the non-inductive level for each of six sources injecting 1.7 MW at 80 kV, using the broader profiles from discharge 142301. As indicated by the caption beneath the frames, confinement giving $H_{98y,2} = 1$ yields a non-inductive current level of ~870 kA, with a central electron temperature of ~1.3 keV. Assuming confinement equivalent to $H_{ST} = 1.0$ for these broad profiles yields electron temperatures of ~1.9 keV and non-inductive current levels of 1225 kA. The strong difference between these scaling expressions is due to the different B_T exponents: 0.15 for the ITER-98y, 2 scaling expression versus 1.08 for the ST scaling. The more peaked thermal profiles (blue curves) yield somewhat lower non-inductive current levels of 750 and 1200 kA for the ITER-98y, 2 and ST scaling expressions.

Also shown in the figure are calculations for cases with each of the neutral beams injecting at 100 kV, for a total power of 15.6 MW. The neutral beams are capable of operating up to 1.5 s in this configuration. For the broad thermal profiles, the current levels range between 1100 and 1450 kA, with temperatures ranging from 1.5 to 2.2 keV, depending on the thermal confinement scaling. The more narrow thermal profiles here reduce the non-inductive level by 50–100 kA, but raise the central electron temperature to 2.3 keV in the case with the ST confinement scaling.

We also note here that some of these scenarios tend to have a rather elevated minimum safety factor, and sometimes significant reversed magnetic shear. Reversed shear in NSTX has, in some instances, triggered the formation of electron internal transport barriers [153–155]. It is for these cases that the assumed profile shapes may be most marginal, as they came from scenarios with normal shear and minimum safety factors in the range 1.1–1.3.

We have done a similar optimization for 100% non-inductive scenarios with four beam sources at $B_T = 0.75$ T. In these cases, the four $R_{tan} = [50, 60, 120, 130]$ sources are used for the optimization (the choice of these beam sources will be discussed in greater detail in sections 6.4 and 6.5). As shown in table 2, for the acceleration voltages of 80 kV at this TF, the non-inductive current levels are found to be in the range 600–800 kA, depending on the profile and confinement assumptions. For 90 kV acceleration voltages, the range is 675–865 kA.

Additional features of these 100% non-inductive scenarios at $B_T = 1.0$ and 0.75 T are given in table 2. The $B_T = 1.0$ T cases all have $q_{min} > 1$; however, some of the $B_T = 0.75$ T scenarios can drop to $q_{min} < 1$ for unfavourable profiles and the $H_{98y,2} = 1$ scaling assumptions. Note that, as indicated by figure 9, the safety factor can be increased by slightly increasing the density.

The current redistribution times in these 100% non-inductive scenarios vary from 0.25 to 0.83 s, depending on the field, heating power, confinement, and profiles. For the 100 kV acceleration cases with 1.5 s heating pulse durations, the pulses are only 2–3 τ_{CR} long, and fully equilibrated profiles will likely not be achieved. On the other hand, for the 80 kV acceleration voltages, the pulse lengths are 7–15 τ_{CR} for $B_T = 1.0$ T, and 12–19 τ_{CR} for $B_T = 0.75$ T. Hence, these should allow the study of fully equilibrated 100% non-inductive scenarios.

We note that these scenarios all have pressure-drive currents dominant compared with neutral beam driven currents. This is largely a function of the desire to avoid NBCD overdrive on the magnetic axis driving down q_{min}. As

Table 2. Parameters of selected fully non-inductive scenarios for NSTX-Upgrade. The $B_T = 1.0$ T scenarios have six neutral beam sources, while the $B_T = 0.75$ T scenarios have four sources.

Voltage (kV)	Profiles	Scaling	B_T (T)	I_p (kA)	P_{inj} (MW)	f_{BS}	q_{min}	q_{95}	τ_{CR} (s)	β_N	β_P	W_{tot} (kJ)	W_{fast}/W_{tot}
80	Broad	$H_{98y,2}$=1	1	870	10.2	0.67	1.60	18.7	0.41	4.0	2.4	457	0.26
80	Broad	H_{ST}=1	1	1225	10.2	0.74	2.37	13.4	0.72	4.9	2.1	792	0.14
80	Narrow	$H_{98y,2}$=1	1	750	10.2	0.63	1.41	20.9	0.33	4.3	2.9	415	0.34
80	Narrow	H_{ST}=1	1	1200	10.2	0.74	2.48	12.8	0.72	5.3	2.2	828	0.16
90	Broad	$H_{98y,2}$=1	1	975	12.6	0.62	1.50	16.2	0.45	4.3	2.3	550	0.26
90	Broad	H_{ST}=1	1	1325	12.6	0.72	2.03	12.3	0.78	5.3	2.1	925	0.15
90	Narrow	$H_{98y,2}$=1	1	875	12.6	0.60	1.39	17.1	0.38	4.6	2.6	520	0.32
90	Narrow	H_{ST}=1	1	1300	12.6	0.70	2.10	11.6	0.75	5.6	2.2	948	0.17
100	Broad	$H_{98y,2}$=1	1	1100	15.6	0.64	1.52	14.4	0.49	4.8	2.2	689	0.23
100	Broad	H_{ST}=1	1	1450	15.6	0.68	1.76	11.1	0.83	5.7	2.0	1089	0.16
100	Narrow	$H_{98y,2}$=1	1	1000	15.6	0.55	1.31	14.5	0.42	4.9	2.5	632	0.31
100	Narrow	H_{ST}=1	1	1400	15.6	0.67	1.82	10.7	0.79	6.0	2.2	1093	0.18
80	Broad	$H_{98y,2}$=1	0.75	635	6.8	0.71	0.98	19.8	0.29	4.3	2.6	266	0.32
80	Broad	H_{ST}=1	0.75	800	6.8	0.73	1.53	15.5	0.41	4.8	2.3	374	0.23
80	Narrow	$H_{98y,2}$=1	0.75	600	6.8	0.70	0.81	21.0	0.26	4.9	3.1	286	0.40
80	Narrow	H_{ST}=1	0.75	770	6.8	0.71	1.72	15.6	0.39	5.3	2.6	396	0.27
90	Broad	$H_{98y,2}$=1	0.75	725	8.4	0.65	1.10	16.7	0.32	4.7	2.5	328	0.31
90	Broad	H_{ST}=1	0.75	865	8.4	0.69	1.36	14.2	0.43	5.2	2.3	435	0.24
90	Narrow	$H_{98y,2}$=1	0.75	675	8.4	0.64	0.90	17.6	0.29	5.2	2.9	342	0.37
90	Narrow	H_{ST}=1	0.75	850	8.4	0.68	1.54	13.7	0.42	5.6	2.5	469	0.27

a consequence, the values of β_N and β_P are comparatively high. However, as will be shown in section 7, these β_N values are not larger than presently achieved in NSTX. Furthermore, scenarios with $\beta_P = 2$ have recently be sustained for long periods in NSTX [44].

Note also that additional 100% non-inductive scenarios will be illustrated in section 6.5, in the context of modifying the current profile with various different combinations of neutral beams, and in section 6.6, in the context of very high bootstrap fraction scenarios.

6.2. High-current partial-inductive scenarios at $B_T = 1.0$ T and 0.75 T

While a steady-state plasma must be fully non-inductive, there are many physics studies facilitated by increasing the plasma current beyond the non-inductive level. These could include, for instance, studies of the collisionality dependence of core transport, or the current scaling of the divertor heat flux width. The centrally peaked relaxed inductive current tends to reduce q_{min}. Hence, it is instructive to consider what are the maximum current levels that can be sustained with $q_{min} > 1$, as a function of beam voltage, TF and density. This is the purpose of the present section.

A solution to this optimization, for $B_T = 1.0$ T, six neutral beam sources, a 15 cm outer gap, and Greenwald fraction $0.7 < f_{GW} < 0.75$, is shown in figure 20 and table 3. For 80 kV acceleration voltage, the maximum sustainable current is between 1250 and 1800 kA; the larger number corresponds to the broader profiles and $H_{ST} = 1$ thermal scaling, while the smaller number corresponds to the peaked profiles and $H_{98y,2} = 1$ thermal scaling. Central electron temperatures are between 1.7 and 2.3 keV. As indicted in figure 2, the neutral beams can provide heating for up to 5 s in this configuration.

The parameters of these scenarios are significantly increased when the acceleration voltage is increased to 100 kV

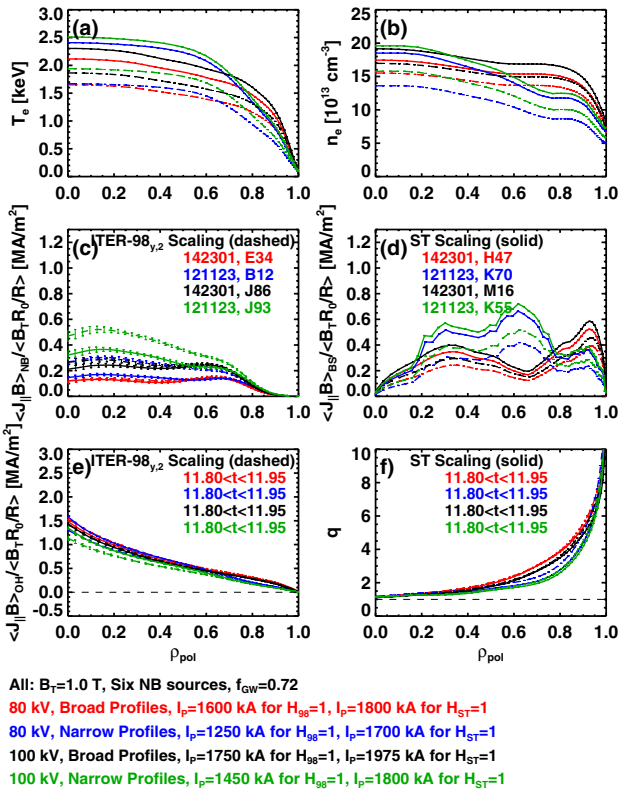

Figure 20. Examples of the maximum sustainable current for various profile and confinement assumptions, at $B_T = 1.0$ T. Optimizations are shown for 80 kV and 100 kV acceleration voltages, with six neutral beam sources in each case.

(black and green traces in figure 20). The projected currents increase to 1450–1975 kA, with peak electron temperatures of >2.5 keV for the ST confinement scaling and more peaked profiles.

Table 3. Parameters of selected high-current partial-inductive scenarios for NSTX-Upgrade. The $B_T = 1.0$ T scenarios have six neutral beam sources, while the $B_T = 0.75$ T scenarios have four sources.

Voltage (kV)	Profiles	Scaling	B_T (T)	I_p (kA)	P_{inj} (MW)	f_{GW}	f_{BS}	q_{95}	$\nu^*_{e,\rho=0.5}$	τ_{CR} (s)	β_N	W_{tot} (kJ)	W_{fast}/W_{tot}
80	Broad	$H_{98y,2}$=1	1	1600	10.2	0.74	0.39	8.4	0.08	0.55	3.8	796	0.09
80	Broad	H_{ST}=1	1	1800	10.2	0.73	0.47	7.8	0.06	0.79	4.8	1118	0.07
80	Narrow	$H_{98y,2}$=1	1	1250	10.2	0.73	0.40	8.9	0.06	0.44	3.8	598	0.17
80	Narrow	H_{ST}=1	1	1700	10.2	0.74	0.49	7.9	0.03	0.80	4.9	1092	0.08
90	Broad	$H_{98y,2}$=1	1	1700	12.6	0.74	0.40	7.9	0.07	0.62	4.3	937	0.10
90	Broad	H_{ST}=1	1	1900	12.6	0.73	0.47	7.4	0.05	0.85	5.1	1267	0.08
90	Narrow	$H_{98y,2}$=1	1	1350	12.6	0.73	0.42	8.5	0.05	0.50	4.3	723	0.17
90	Narrow	H_{ST}=1	1	1750	12.6	0.74	0.50	7.7	0.03	0.83	5.2	1190	0.10
100	Broad	$H_{98y,2}$=1	1	1750	15.6	0.74	0.42	7.9	0.06	0.66	4.6	1044	0.12
100	Broad	H_{ST}=1	1	1975	15.6	0.73	0.48	7.2	0.05	0.90	5.5	1406	0.09
100	Narrow	$H_{98y,2}$=1	1	1450	15.6	0.73	0.43	8.1	0.04	0.56	4.7	865	0.18
100	Narrow	H_{ST}=1	1	1800	15.6	0.74	0.50	7.5	0.03	0.86	5.6	1304	0.12
80	Broad	$H_{98y,2}$=1	0.75	1250	6.8	0.74	0.39	8.0	0.09	0.39	4.1	498	0.11
80	Broad	H_{ST}=1	0.75	1300	6.8	0.74	0.40	7.8	0.08	0.43	4.3	547	0.10
80	Narrow	$H_{98y,2}$=1	0.75	1025	6.8	0.73	0.39	8.2	0.06	0.34	4.2	406	0.19
80	Narrow	H_{ST}=1	0.75	1125	6.8	0.73	0.44	8.1	0.05	0.43	4.7	505	0.15
90	Broad	$H_{98y,2}$=1	0.75	1300	8.4	0.74	0.40	8.0	0.08	0.43	4.5	566	0.12
90	Broad	H_{ST}=1	0.75	1350	8.4	0.74	0.42	7.7	0.07	0.47	4.7	619	0.11
90	Narrow	$H_{98y,2}$=1	0.75	1125	8.4	0.75	0.42	9.0	0.05	0.38	4.5	500	0.18
90	Narrow	H_{ST}=1	0.75	1250	8.4	0.75	0.44	8.1	0.04	0.46	4.9	600	0.15
80	Broad	$H_{98y,2}$=1	1	1850	10.2	1.05	0.41	7.3	0.16	0.46	4.5	1079	0.03
80	Broad	H_{ST}=1	1	2000	10.2	1.03	0.49	7.1	0.12	0.61	5.4	1417	0.03
80	Narrow	$H_{98y,2}$=1	1	1450	10.2	1.03	0.42	7.6	0.10	0.39	4.2	757	0.07
80	Narrow	H_{ST}=1	1	1850	10.2	1.04	0.50	6.9	0.06	0.63	5.5	1307	0.04
80	Broad	$H_{98y,2}$=1	0.75	1425	6.8	1.05	0.41	7.2	0.20	0.32	4.7	650	0.04
80	Broad	H_{ST}=1	0.75	1425	6.8	1.05	0.43	7.3	0.19	0.33	4.8	675	0.04
80	Narrow	$H_{98y,2}$=1	0.75	1150	6.8	1.04	0.43	7.7	0.11	0.29	4.6	504	0.09
80	Narrow	H_{ST}=1	0.75	1250	6.8	1.04	0.46	7.4	0.09	0.34	5.0	602	0.07

Some additional parameters of these and related scenarios are given in table 3. As with the fully non-inductive scenarios, the pulse durations for the 1.0 T, 100 kV cases are between 1.5 and 3 τ_{CR} in duration. This may be advantageous, as it will facilitate even higher current operation if the current profile cannot fully relax before the end of the beam heating pulse. The 80 kV cases have pulse durations of 6–12 τ_{CR} for $B_T = 1.0$ T, and 11–14 τ_{CR} for $B_T = 0.75$ T, and the requirement for scenarios with fully evolved $q_{min} > 1$ is likely more strict.

The bottom of table 3 also shows the results with 80 kV beams but a Greenwald fraction just above 1.0. This increases the central safety factor for fixed I_P, or allows operation at higher current for fixed q_{min}. These cases allow 5 s operation at $I_P = 2$ MA and $B_T = 1.0$ T for favourable confinement and profiles. The fast-ion pressure is at most 10% of the total pressure in these cases, compared with values of W_{fast}/W_{tot} of ∼20% in the $f_{GW} = 0.74$ cases. Note that these very high-density scenarios may be favourable for divertor power handling, though it remains unclear if there will be any degradation of confinement at the higher densities.

6.3. Partially inductive sustained long pulse at $B_T = 0.75$ T and reduced current

Many studies will be interested in testing the behaviour of the longest possible discharges, even if this requires a reduction in the plasma current. These include, for instance, particle retention studies or the study of RWM control and high-β disruption avoidance for the longest possible duration. In this section, we present scenarios that may allow a single discharge to be sustained for 8–10 s. The TF strength for these cases is $B_T = 0.75$ T, such that the heating limit of the TF coil is not exceeded for pulses of the target duration.

We will study two different beam configurations to facilitate this very long-pulse goal. The first utilizes 80 kV for each source, modulated so that only three sources are on at any given time. With a five second duration for any single source and a duty cycle of 50%, we can sustain the configuration for a full 10 s. A second configuration uses all six sources configured for 65 kV operation, allowing an 8 s heating pulse.

The current and heating limit of the ohmic solenoid coil play a key role in determining this optimization. In order to assess this, we have estimated the solenoid current evolution as follows. The solenoid pre-charge waveform is determined from the OH circuit and power supply characteristics. The plasma current ramp-up times, ramp-up flux and ramp-down times, all as a function of flat-top plasma current, are given in table 1 of [47]. The flat-top surface voltage, and hence rate of solenoid current change, is taken from the TRANSP simulations. A voltage of −0.5 V is assumed for the ramp-down. These parameters are sufficient to form a simple solenoid current waveform. The resulting solenoid current evolution can be compared with the maximum allowed current, and the $\int I_{OH}^2\,dt$ can be compared with the limit on that quantity set by coil heating.

As noted above, one long-pulse scenario uses 80 kV acceleration voltages with a 50% duty cycle, for a total duration

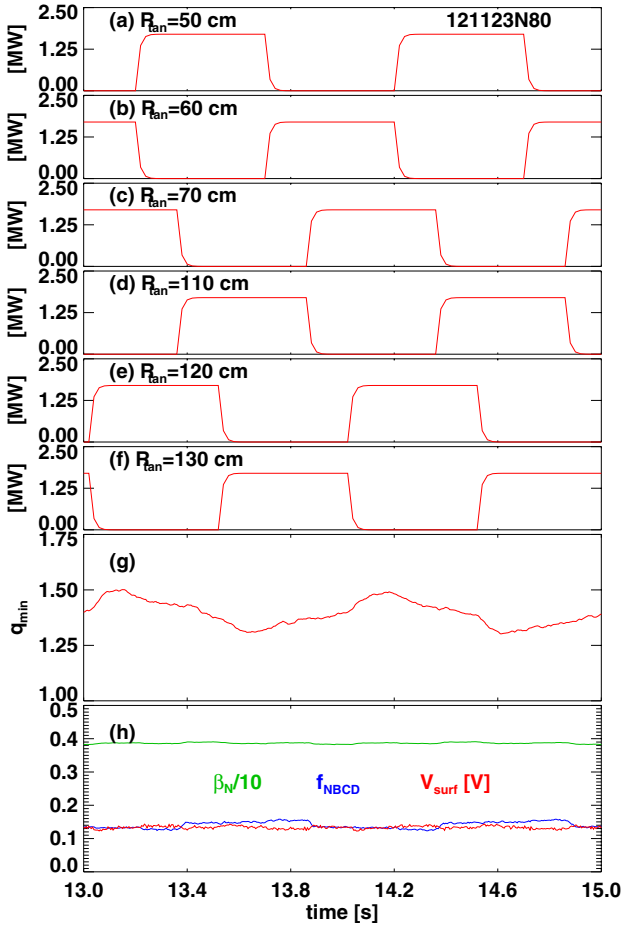

Figure 21. Effect of neutral beam modulations on a fully evolved very long-pulse scenario. Shown are the neutral beam powers in frames (a)–(f), the minimum safety factor ($q_{\min}$) in frame (g), and the normalized beta (β_N), beam current drive fraction (f_{NBCD}) and surface voltage (V_{surf}) in frame (h).

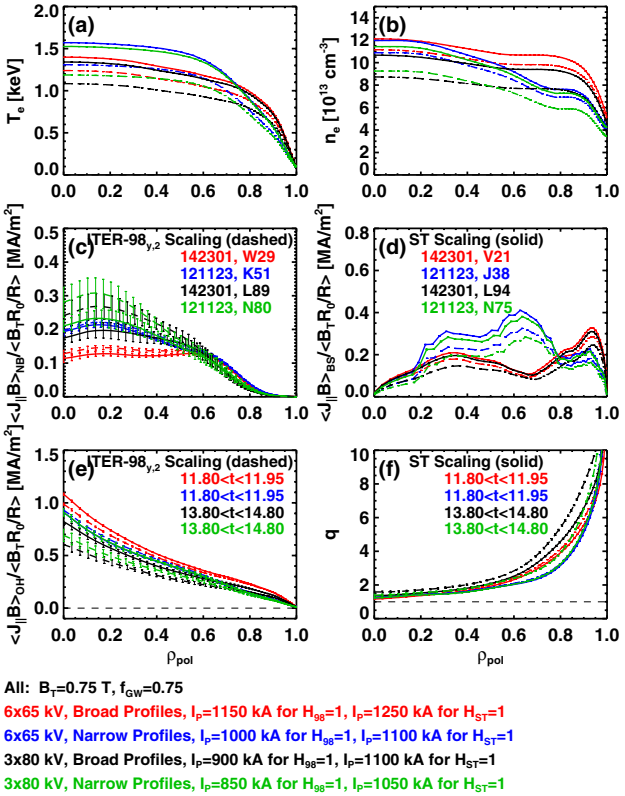

Figure 22. Example profiles for configurations optimized for very long pulse. The plasma current level varies among the different configurations, which all have $0.7 < f_{GW} < 0.75$.

of the heating pulse of 10 s. We also wish to reduce the total number of modulations to 20 [156]. The key question to answer is whether this modulation will produce unacceptable variations in the central safety factor and other parameters. An example calculation is shown in figure 21, for an $I_P = 850$ kA scenario based on profiles from the discharge 121123. Frames (a)–(f) show the neutral beam power. Each source is modulated with 0.5 s on followed by 0.5 s off, staggered such that the total input power is constant at 5.1 MW. The evolution of the central safety factor is illustrated in frame (g), and shows a modulation of about 0.15 units. The normalized β_N is nearly constant, reflecting that modulations in the total pressure due to the different beam geometries are quite small. The modulations in the surface voltage are also quite negligible. The beam current drive fraction does show some modulation, mainly due to the oscillation between the $R_{tan} = 70$ cm and $R_{tan} = 110$ beams, which have significantly different current drive efficiencies [47].

With this background, the profiles which provide 8–10 s operation are shown in figure 22, and the model solenoid current waveforms are shown in figure 23. The colour scheme and line types are the same in the two figures. Again, the different profile and confinement assumptions are tested; these result in various levels of plasma current pending the assumptions.

For the modulated 80 kV scenarios in green and black with 5.1 MW of injected power, the level of plasma current varies between 850 and 1100 kA. As before, the highest allowed level is for the broad thermal profiles and ST scaling, and the lowest level is for the more peaked thermal profiles and $H_{98y,2} = 1$ scaling. These cases generally have somewhat elevated $q_{\min}$. This is because the $\int I_{OH}^2 \, dt$ limit on the solenoid generally constrains the maximum plasma current for scenarios designed for sustainment up to 10 s. This is most easily seen in the green and black curves of figure 23(b), where there is a rapid increase in $\int I_{OH}^2 \, dt$ towards the end of the pulse. The plasma current can generally be increased by 50–100 kA while maintaining $1.1 < q_{\min} < 1.2$, but the solenoid coil heating limit is invariably exceeded before the full 10 s heating phase.

For the 65 kV acceleration voltage scenarios in red and blue (corresponding the broad and peaked thermal profile), the total input power is 6.6 MW, sustainable for up to 8 s. This results in sustainable current levels between $I_P = 1000$ kA for narrow profiles and $H_{98y,2} = 1$ and $I_P = 1250$ A for broader profiles and $H_{ST} = 1$. The $\int I^2 t$ limit of the solenoid coil is not generally a constraint in these cases. Rather, the maximum current is set by the requirement to operate with $q_{\min} > 1$.

Figure 23 also shows the solenoid and plasma current traces for discharge 129125 [41, 44] This $I_P = 750$ kA discharge has the longest I_P flat-top duration ever achieved in NSTX. The performance of the projected NSTX-Upgrade very long-pulse plasmas is 10–60% better in terms of plasma current level, and 4.5–5.5 times better in terms of pulse duration.

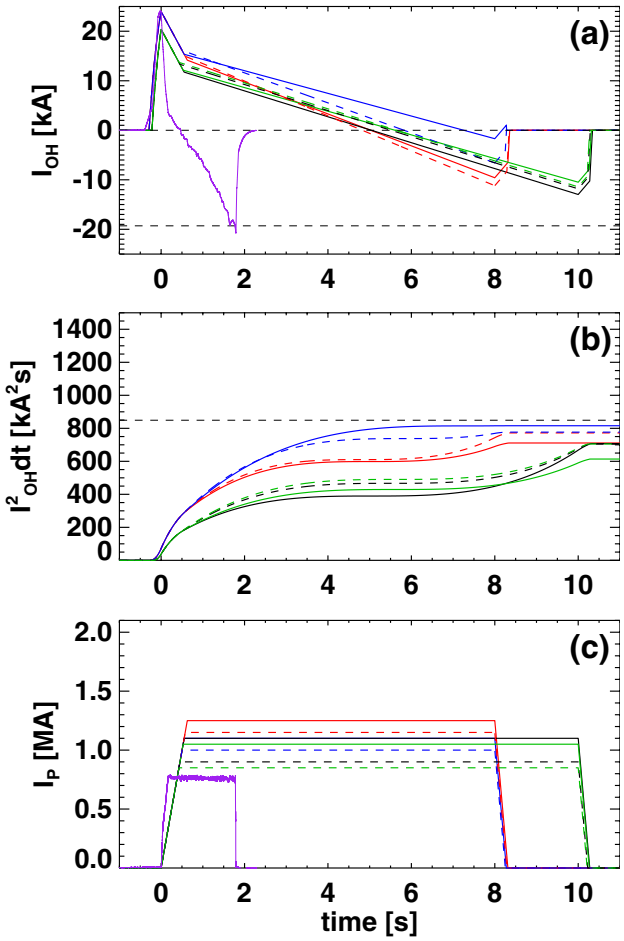

Figure 23. (*a*) Model solenoid current, (*b*) $\int I_{OH}^2\,dt$, and (*c*) plasma current evolution for the scenarios in figure 22. Also shown in frames (*a*) and (*c*) are the solenoid and plasma currents for NSTX discharge 129125.

We also note that these simulations were done assuming that the ion thermal transport remained at the neoclassical level. The discussions in section 5.4 demonstrate that at long as the overall confinement level is maintained, increasing the ion thermal transport can be beneficial. If this were to occur for the scenarios listed here, it would reduce the required induction, potentially allowing higher currents for these pulse durations.

Additional parameters for these scenarios are given in table 4. The key observation is that the pulse lengths are between 18 and 34 τ_{CR} in duration, all with β_N above the no-wall limit and >50% of the current driven non-inductivly.

6.4. Sustained highest toroidal β

It is desirable to operate a fusion system at the highest possible value of β_T, since the fusion power scales as $\beta_T^2 B^4$ [11]. The requirements for operating a tokamak or ST at high toroidal β have been clearly articulated in previous research. The key step is to operate at high normalized current $I_N = I_P/aB_T$, since Troyon scaling [126, 157] implies $\beta_T = I_N\beta_N$. The normalized current cannot, however, be made arbitrarily large, as this would result in the edge safety factor becoming too low; a cylindrical safety factor $q^* = (\varepsilon\pi aB_T(1+\kappa^2))/\mu_0 I_P$ less than ~1.8 has been shown theoretically to be a good boundary for the resulting external kink [135]. Given that q^* and I_N are related as $q^* = (\varepsilon\pi(1+\kappa^2))/\mu_0 I_N$, it is clear that increasing I_N at fixed q^* requires that either the elongation must be increased, or the aspect ratio decreased. Following this recipe of high current and strong shaping has resulted in transiently very high values of β_T in an ST. For instance, START plasmas developed scenarios with transient β_T values of ~40% [112], a value that has been matched for short durations in the highest β NSTX plasmas [113, 116]. For these NSTX cases, these were typically accomplished with plasma currents in the vicinity of 1.2–1.3 MA and TFs in the vicinity of 0.3–0.35 T, and the duration at very high β_T was typically no longer than a single energy confinement time. These scenarios were typically limited by the current limit at low q^*, or the tendency of core $n = 1$ modes to become unstable as q_{min} approached 1 [116].

For these reasons, while operating at high I_N may facilitate the achievement of transient very high-β_T, the configuration may not be sustainable. An additional requirement is that the fully evolved current profile yield $q_{min} > 1$ [36, 43, 44, 46, 116–119]. For the present device, this condition implies that the density of the centrally peaked ohmic current not become too large, and that the NBCD be configured to drive current off-axis. To this end, a study to optimize β_T using a 0.55 T TF has been completed. This value of TF was chosen because it overlaps with the largest value ever routinely run in NSTX, albeit with flat-top durations of <1 s. The TF flat-top duration at this field in NSTX-Upgrade is significantly longer than the longest conceivable plasma discharge given other facility limitation.

As will be seen below, these scenarios have some significant differences from the 100% non-inductive scenarios discussed above. For instance, the NBCD profile tends to become hollow, and the plasma elongation is quite high. As a consequence, section 6.4.1 will revisit some issues of current profile optimization and MHD stability for these scenarios. Section 6.4.2 will then show the results of this optimization for the various profile and confinement assumptions.

6.4.1. Parameters the high-β_T optimization. Many parametric dependences of the high-β_T optimization were studied as part of the S3 scenario in section 5. This scenario has 1200 kA of plasma current and a TF of 0.55 T, four sources with 90 kV injection energy, capable of injecting 2.1 MW per source for up to 3 s. We utilize the 20 cm outer gap shape illustrated in figure 5, and the four beam sources are the $R_{tan} = [50, 60, 120, 130]$ sources; both of these choices elevate q_{min} as much as possible, the latter by driving a hollow NB current drive profile. The results of section 5, also shows that this scenario was largely insensitive to choices of D_{FI}, the ion thermal confinement, and Z_{eff}, provided that a given confinement multiplier ($H_{98y,2} = 1$, for instance) is maintained.

The left-hand column of figure 24 shows additional calculations of plasmas fitting this scenario, where various parameters are again plotted in the space of $H_{98y,2}$ and f_{GW}. It is clear that this optimizations can produce quite high values of β_N, with values of ~6 anticipated at the higher Greenwald fraction with $H_{98y,2} = 1$. These correspond to values of β_T in the range of 25%. The non-inductive fraction is again largely independent of the density, and is in the range ~50–60% for

Table 4. Parameters of scenarios optimized for very long pulses.

Beam Config.	Profiles	Scaling	I_p (kA)	f_{NICD}	f_{BS}	τ_{CR} (s)	β_N	β_P	q_{min}	q_{95}	V_{surf} (V)	W_{tot} (kJ)
Six 65 kV	Broad	$H_{98y,2}$=1	1150	0.54	0.40	0.36	3.9	1.3	1.25	9.0	0.18	439
Six 65 kV	Broad	H_{ST}=1	1250	0.56	0.42	0.43	4.3	1.3	1.16	8.3	0.16	524
Six 65 kV	Narrow	$H_{98y,2}$=1	1000	0.60	0.42	0.33	4.1	1.6	1.24	10.1	0.15	396
Six 65 kV	Narrow	H_{ST}=1	1100	0.66	0.48	0.43	4.6	1.6	1.27	9.2	0.12	498
3 Staggered 80 kV	Broad	H_{98}=1	900	0.61	0.45	0.30	3.6	1.5	1.58	11.7	0.13	317
3 Staggered 80 kV	Broad	H_{ST}=1	1100	0.60	0.46	0.41	4.1	1.4	1.37	9.6	0.13	444
3 Staggered 80 kV	Narrow	H_{98}=1	850	0.63	0.44	0.29	3.9	1.8	1.39	11.9	0.13	321
3 Staggered 80 kV	Narrow	H_{ST}=1	1050	0.64	0.47	0.41	4.4	1.6	1.23	9.6	0.12	452

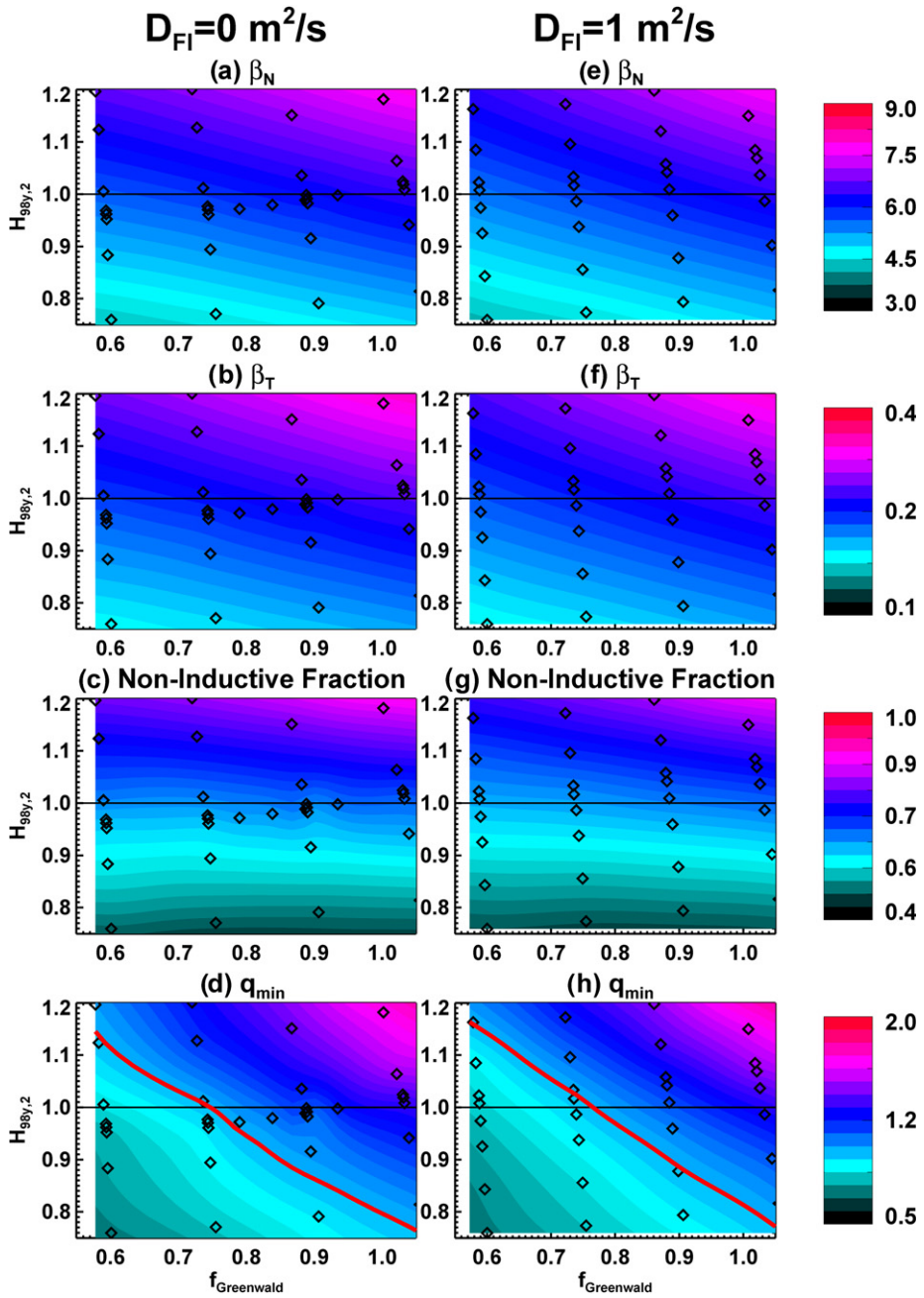

Figure 24. Contours of β_N, β_T, the non-inductive fraction, and q_{min} versus the confinement factor $H_{98y,2}$ and Greenwald fraction. These configurations have $I_P = 1200$ kA, $B_T = 0.55$ T with $R_{tan} = [50, 60, 120, 130]$, 90 kV beams and a target boundary shape with $A = 1.81$ and $\kappa = 2.95$. The left column has $D_{FI} = 0\,m^2\,s^{-1}$, while the right column has $D_{FI} = 1\,m^2\,s^{-1}$. The $q_{min} = 1$ contour is illustrated in the bottom row.

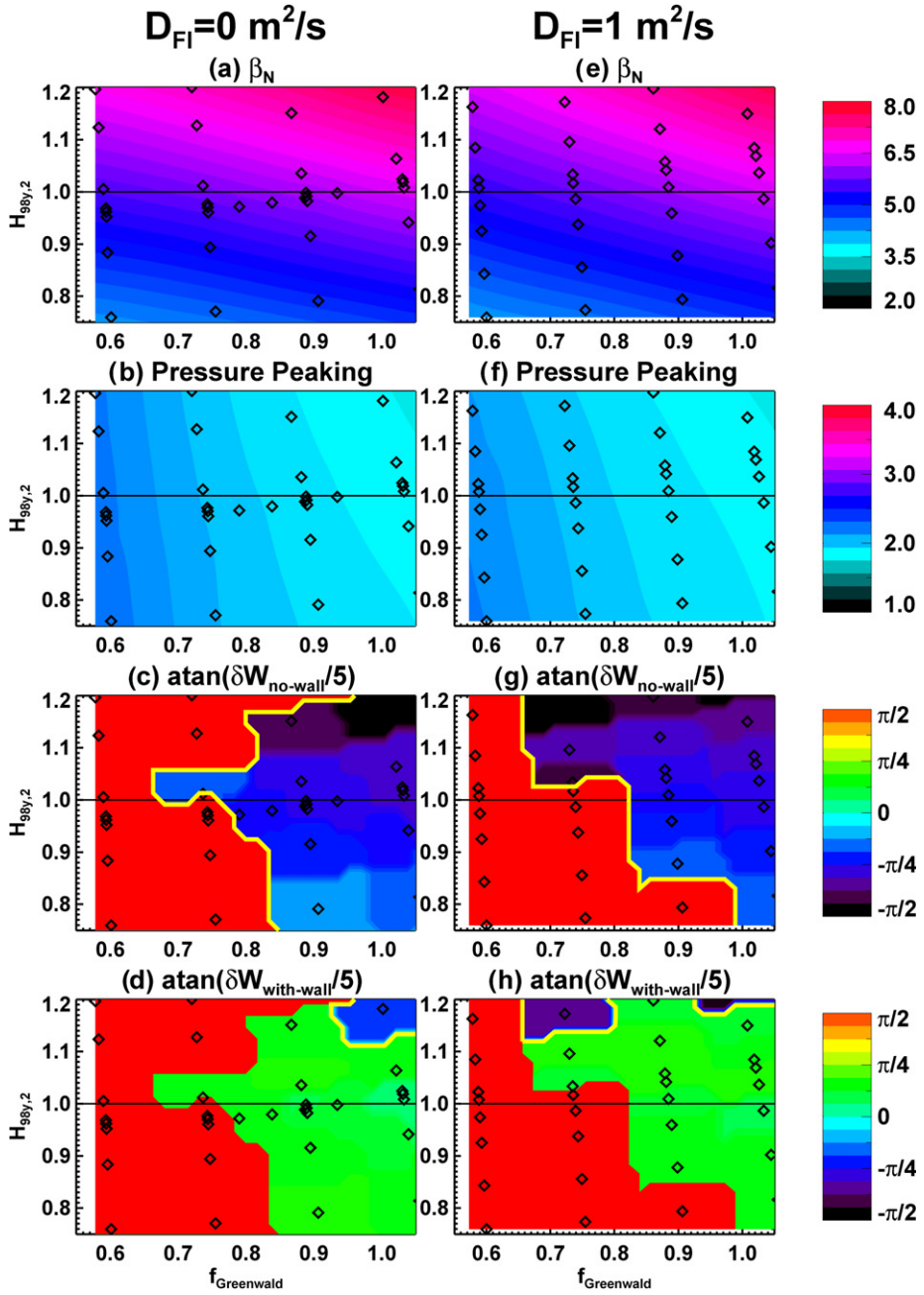

Figure 25. Ideal stability parameters for configurations in figure 24. See text for further details.

these cases. Most importantly, the minimum safety factor in figure 18(*d*) tends to drop beneath 1 for densities below $f_{GW} = 0.8$ (again, at $H_{98y,2} = 1$).

The right-hand column shows the same data, but for calculations with an applied fast-ion diffusivity of $1\ m^2\ s^{-1}$. Recall that this value represents the maximum value compatible with measurements in MHD-quiescent discharges in NSTX [43], and was large enough to have a significant impact on the near non-inductive S1 scenario in section 5. However, for the present scenario, the values of non-inductive current fraction, β_N, and q_{min} are largely unchanged by this value of D_{FI} over the full range of confinement and density.

The global stability parameters for these scenarios are shown in figure 25, for the same calculations as in figure 24; see discussion of figure 12 for a detailed description of the stability parameter. The left-hand column corresponds to the case with purely classical beam physics, while the right column has an imposed $D_{FI} = 1\ m^2\ s^{-1}$. The pressure peaking in these scenarios is substantially lower than the six-source 1 MA, 1 T scenario in figure 12, for two reasons: (i) the thermal pressure, which has a broad profile in H-mode, is a larger fraction of the total pressure, and (ii) the fast-ion pressure in more broad than in figure 12, due to the dominantly off-axis injection. Furthermore, the total pressure peaking is not particularly impacted by the fast-ion diffusion, for the same two reasons.

As a consequence, the stability maps are not significantly different between these two cases. As is shown in the no-wall stability calculation in the third row, a large fraction of

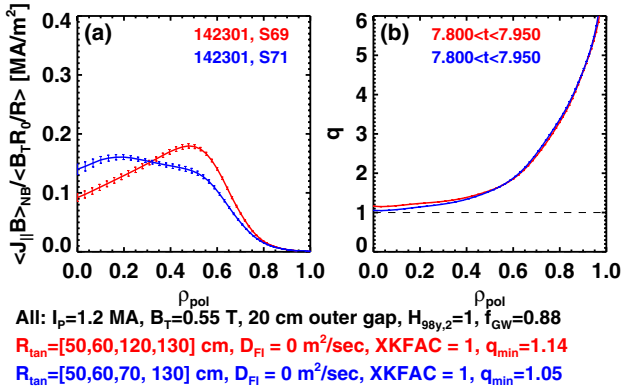

Figure 26. Test of two different neutral beam source combinations for maintaining elevated $q_{\min}$ in the high-β_T scenario optimization.

confinement versus density space is precluded by $q_{\min}$ being close to or less than unity. All the other operating points are unstable without a wall. The inclusion of a wall in the lower row opens up a significant operating space at $H_{98y,2} = 1$ and higher density, and it is this operating space that is of interest for scenario development.

The beam tangency radii of 50, 60, 120 and 130 cm in these cases were chosen to provide substantial heating while eliminating the central current drive as much as possible. One might think, however, that the $R_{\tan} = 70$ source might be a better choice than the $R_{\tan} = 120$ beam, given that the $R_{\tan} = 120$ cm source is directed near the magnetic axis. That this is not true is shown in figure 26. Using the $R_{\tan} = 70$ sources tends to increase the central NBCD, lower the safety factor profile, and reduce the bootstrap current. The net result is to decrease the central safety factor by ~0.1 units, which would have a deleterious effect on the stability of the configuration.

6.4.2. Scenarios that maximize β_T with $q_{\min} > 1$. With these results in mind, we have determined the maximum levels of current that allow $q_{\min} > 1$ operation for the $R_{\tan} = [50, 60, 120, 130]$ cm neutral beam configuration at $B_T = 0.55$ T, knowing that this optimization will maximize β_T. This optimization was done for both 90 and 100 kV acceleration voltages, for different profile shapes and thermal confinement scalings. The Greenwald fraction was fixed at 0.7 for all cases. The results of this optimization are shown in figure 27, and additional parameters are given in table 5.

For the 90 kV acceleration voltage cases (capable of producing up to 3 s long heating pulses), the β_T values range from 18% to 22%, with corresponding plasma currents ranging between 900 and 1100 kA. The non-inductive fraction ranges between 65% and 75% for these scenarios. For the 100 kV acceleration voltage cases (capable of producing up to 1.5 s long heating pulses), the β_T values range from 20% to 27%, with corresponding plasma currents ranging between 925 and 1200 kA. The non-inductive fraction in these cases ranges between 62% and 82%. None of these scenarios challenge the current limit on the OH coil for the allowed pulse duration.

There are a few other features to note about these scenarios. The central beam current drive is always higher with the peaked profiles, due to the higher central electron temperature and lower edge density; this is similar to the results

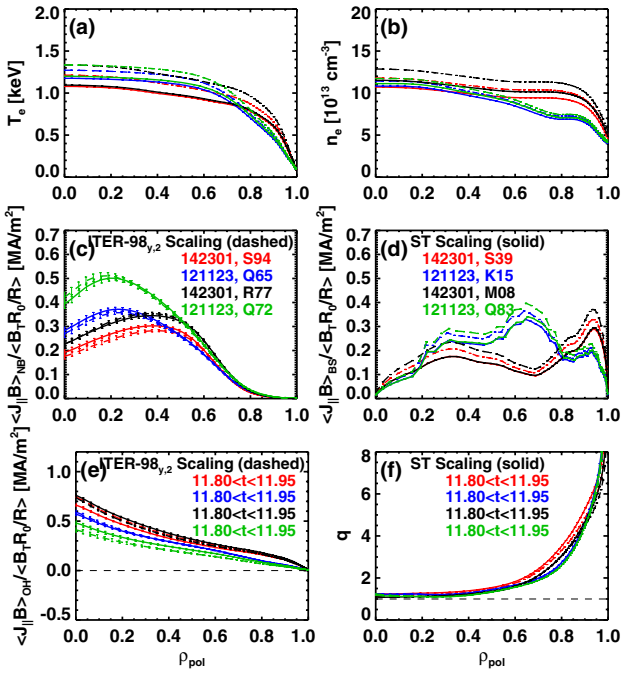

Figure 27. Profiles for a range of scenarios designed to maximize the sustainable β_T. All cases have $f_{GW} = 0.7$, with an $A \approx 1.8$ plasma boundary and 8.4 MW of injected power.

with other optimizations. Unlike previous optimizations, the higher temperatures are projected using the ITER-98y, 2 confinement scaling expression. The strong B_T dependence in the ST scaling expression results in a significant confinement enhancement at stronger TF. These scenarios, with lower B_T of 0.55 T, cannot take advantage of that dependence.

Additional parameters of these scenarios are given in table 5. The pulses are ~$10\tau_{CR}$ in duration for 90 kV and ~$6\tau_{CR}$ for 100 kV cases. The current profile should thus be fully equilibrated. The values of β_N are the highest discussed in this paper, as is fitting for scenarios designed to challenge MHD stability physics and control. This high value of β_N, combined with the large value of I_P/B_T, results in the large values of β_T. Finally, we emphasize that while these β_T values are substantially less than achieved transiently in MAST, START and NSTX, this difference is not driven by the slight increase in aspect ratio of the NSTX-U device. Rather, it is driven by the desire to maintain the relaxed $q_{\min} > 1.1$–1.2, which results in the value of normalized current being considerably less than those transient cases.

6.5. Current profile control using different NB combinations

An underlying concept in the above sections has been the selection of shapes, densities and beam configurations that achieve some given scenario goal with $q_{\min} > 1$. In this section, we evaluate the prospects for current profile control at fixed shape and plasma density, using varying combinations of neutral beam sources. These simulations demonstrate

Table 5. Parameters of very high β_T discharges at $B_T = 0.55$ T and elongation of ~ 2.9.

Voltage (kV)	Profiles	Scaling	B_T (T)	I_p (kA)	f_{NICD}	q_{95}	q^*	τ_{CR} (s)	β_N	β_T	β_P	W_{tot} (kJ)	W_{fast}/W_{tot}
90	Broad	$H_{98y,2}=1$	0.55	1100	0.66	7.0	3.4	0.32	5.6	0.22	1.5	438	0.14
90	Broad	$H_{ST}=1$	0.55	1000	0.66	7.7	3.7	0.27	5.2	0.19	1.5	368	0.17
90	Narrow	$H_{98y,2}=1$	0.55	950	0.75	8.0	4.1	0.29	5.9	0.20	1.9	397	0.21
90	Narrow	$H_{ST}=1$	0.55	900	0.73	8.4	4.4	0.26	5.6	0.18	1.9	359	0.23
100	Broad	$H_{98y,2}=1$	0.55	1200	0.71	6.4	3.1	0.37	6.3	0.27	1.5	535	0.15
100	Broad	$H_{ST}=1$	0.55	1075	0.64	7.0	3.4	0.27	5.4	0.21	1.5	409	0.18
100	Narrow	$H_{98y,2}=1$	0.55	975	0.83	7.9	3.9	0.31	6.6	0.23	2.0	452	0.23
100	Narrow	$H_{ST}=1$	0.55	925	0.78	8.2	4.2	0.27	6.1	0.20	2.0	398	0.25

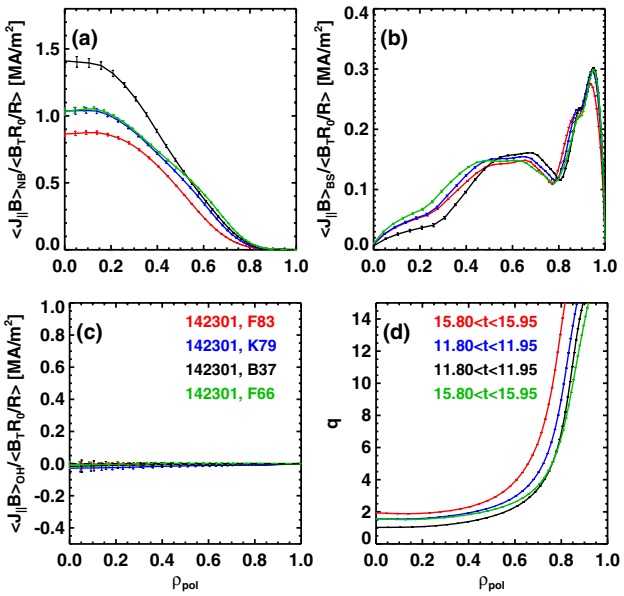

Figure 28. Variation of the safety factor profile with various beam tangency radii, for 100% non-inductive scenarios at $B_T = 1.0$ T. The plasma current is allowed to vary in order to maintain the non-inductive state.

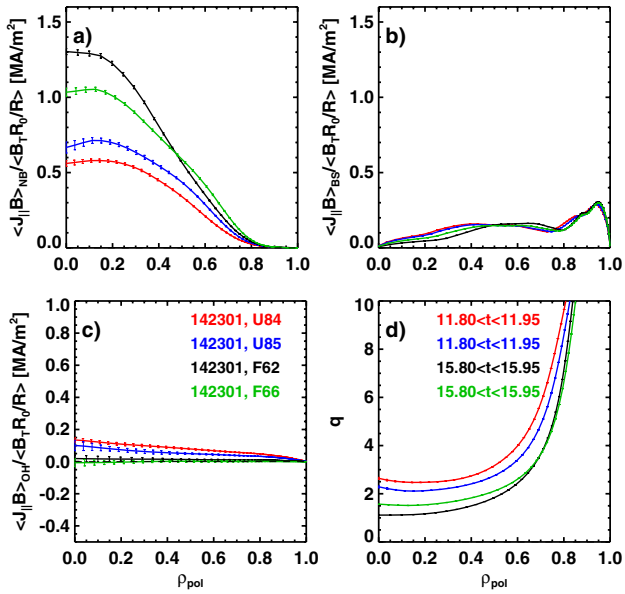

Figure 29. Variation of the safety factor profile with various beam tangency radii, for 800 kA scenarios at $B_T = 1.0$ T. The non-inductive current fraction varies from 87% to 99%.

the potential for closed-loop control of the current profile [158, 159], though the design details for such a controller are out of scope for this work.

An important detail in this study is deciding what should be held fixed. The plasma current can be held fixed allowing the non-inductive current fraction to vary with different beam combinations. Alternatively, the loop voltage can be set to zero, allowing the plasma current to vary at fixed 100% non-inductive fraction. Both contingencies are addressed below. Note that these studies will utilize the broad thermal profiles from 142301 and ITER-98y, 2 scaling on the thermal energy, in order to focus on the effects of the various beam configurations on the current profile.

Figure 28 shows the results of such a study for $B_T = 1.0$ T and $f_{NI} = 100\%$; the plasma current as allowed to vary. The central safety factor is largest, and the plasma current smallest, with tangency radii of [50, 60, 70, 130]; this configuration has eliminated the $R_{tan} = 110$ and 120 cm beams, which have the highest current drive efficiency but also tend to drive current on the magnetic axis. The highest non-inductive plasma currents come from the $R_{tan} = [70, 110, 120, 130]$ combination, which utilizes the four beams with the best current drive efficiency to produce $q_{min} = 1.57$. The lowest values of q_{min} are achieved with the $R_{tan} = [60, 70, 110, 120]$ configuration, with the minimum safety factor falling just above unity.

Figure 29 shows the results of a similar scan, where the plasma current is held fixed at 800 kA. In this case, the $R_{tan} = [70, 110, 120, 130]$ scenario is fully non-inductive with $q_{min} = 1.5$. On the other hand, the $R_{tan} = [50, 60, 70, 130]$ scenario has a non-inductive fraction of only 87%, but a central safety factor of almost 2.5. The $R_{tan} = [60, 70, 110, 120]$ has the lowest minimum safety factor, with $q_{min} = 1.1$ in a near non-inductive state. We note that the calculations in figures 28 and 29 were done with neoclassical fast-ion physics only. The inclusion of some additional anomalous fast-ion diffusivity would likely reduce the difference in q_{min} between these scenarios.

Table 6. Parameters of discharges designed to vary the q-profile using different NB injection geometry.

R_{tan} (cm)	Profiles	Scaling	B_T (T)	I_p (kA)	f_{NICD}	f_{NBCD}	τ_{CR} (s)	β_N	β_P	q_{95}	q_0	q_{min}
[50,60,70,130]	Broad	$H_{98y,2}$=1	1	675	1.00	0.27	0.32	3.5	2.6	25.2	1.93	1.88
[50,60,120,130]	Broad	H_{ST}=1	1	740	1.02	0.30	0.35	3.7	2.6	22.4	1.57	1.55
[60,70,110,120]	Narrow	$H_{98y,2}$=1	1	770	1.01	0.30	0.36	3.8	2.5	21.0	1.03	1.03
[70,110,120,130]	Narrow	H_{ST}=1	1	800	1.00	0.35	0.36	3.8	2.4	19.8	1.57	1.51
[50,60,70,130]	Broad	$H_{98y,2}$=1	1	800	0.87	0.24	0.35	3.5	2.2	19.9	2.64	2.47
[50,60,120,130]	Broad	H_{ST}=1	1	800	0.92	0.28	0.35	3.6	2.3	19.7	2.29	2.11
[60,70,110,120]	Narrow	$H_{98y,2}$=1	1	800	0.98	0.29	0.37	3.8	2.4	19.9	1.11	1.11
[70,110,120,130]	Narrow	H_{ST}=1	1	800	1.00	0.35	0.36	3.8	2.4	19.8	1.57	1.51
[50,60,70,130]	Broad	$H_{98y,2}$=1	0.75	650	1.01	0.26	0.29	4.5	2.7	19.6	1.27	1.23
[50,60,120,130]	Broad	H_{ST}=1	0.75	725	0.99	0.30	0.32	4.7	2.5	16.7	1.12	1.10
[60,70,110,120]	Narrow	$H_{98y,2}$=1	0.75	765	0.99	0.30	0.34	4.8	2.4	15.5	0.68	0.68
[70,110,120,130]	Narrow	H_{ST}=1	0.75	775	1.00	0.34	0.33	4.9	2.4	15.2	0.94	0.93
[50,60,70,130]	Broad	$H_{98y,2}$=1	0.75	800	0.85	0.23	0.33	4.4	2.1	14.5	1.93	1.77
[50,60,120,130]	Broad	H_{ST}=1	0.75	800	0.89	0.27	0.33	4.6	2.2	14.5	1.56	1.46
[60,70,110,120]	Narrow	$H_{98y,2}$=1	0.75	800	0.93	0.28	0.34	4.7	2.3	14.4	0.79	0.79
[70,110,120,130]	Narrow	H_{ST}=1	0.75	800	0.99	0.33	0.34	4.9	2.3	14.6	1.04	1.00

The parameters of these scenarios, and similar scenarios at $B_T = 0.75$ T, are shown in table 6. Given the 3 s pulse duration for 90 kV beams, these scenarios are typically 8.5–10 τ_{CR} in duration. Hence, it is anticipated that the equilibrium will be able to fully respond to variations in the beam configuration during the discharge, and feedback control of the current profile in this way should be possible.

6.6. Prospects for very high bootstrap fraction scenarios with neutral beam heating alone

As a final optimization, we consider the possibility of generating equilibria with very high pressure-driven current fractions using neutral beam heating. In particular, we look for equilibria where the sum of the bootstrap current and the toroidal components of the Pfirsch–Schlueter and diamagnetic currents exceeds 80%. Because neutral beams drive current, a scenario with pressure-driven current magnitude equal to the total current will have negative loop voltage; in this case, the ohmic currents cancel the neutral-beam-driven currents. Ideally, the NBCD and ohmic current profiles would have similar profile shapes, so that the cancellations would be uniform across the profile. These constant I_P scenarios will thus 'recharge' the solenoid, as opposed to non-inductive current ramp-up [47, 160–162], where $V_{loop} = 0$ and the plasma current increases.

All of the simulations considered here use the 15 cm outer gap target boundary with a TF of 1.0 T. Four different values of heating power are considered, all using 90 kV neutral beams: 12.6 MW using all available sources, 8.4 MW using the R_{tan} = [50, 60, 70, 130] sources, 6.3 MW using the R_{tan} = [60, 70, 130] sources and 4.2 MW using the R_{tan} = [60, 130] sources. For each power, the chosen source configuration was optimized to broaden the beam current drive and total pressure profile. High values of Greenwald fraction were typically chosen, since the higher density tends to decrease the central beam current drive and increase the bootstrap fraction.

Figure 30 shows the profile shapes as a function of the plasma current, for fixed heating power of 8.4 MW and a Greenwald fraction of 0.8. The lowest plasma current case clearly shows a negative ohmic current profile, and also a very

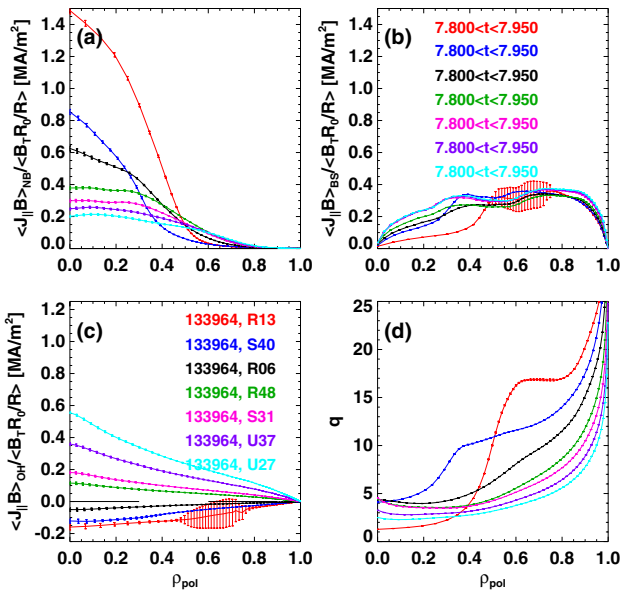

Figure 30. Examples of profile variations as the pressure-driven current fraction approaches unity. Shown are profiles of (*a*) the neutral beam currents, (*b*) the bootstrap current, (*c*) the ohmic currents and (*d*) the safety factor. Note that these simulations are at a fixed Greenwald fraction of 0.85.

low value of q_{min} due to the strong central NBCD. The total current has a local minimum at $\rho_{pol} \sim 0.6$, and a resulting region of higher safety factor at the same radius. Further reductions in the plasma current or increases in confinement often result in even more severe local current minimal and excursions in the q-profile, and often cause the equilibrium code to crash. Indeed, the ability of the equilibrium code to converge has set the upper limit on confinement and lower limit

on the plasma current in the scenarios discussed in this section. Note that the profile of beam-driven currents in this example is much more narrow than the ohmic current profile, a situation which exists for any combination of beams yet tested.

The configuration has a bootstrap fraction of 98% at 700 kA and a non-inductive fraction of 118%. As the plasma current is increased above that value, we see that the central neutral-beam-driven currents rapidly decrease, resulting in a rapid increase in the central safety factor. The minimum safety factor drops as I_P is increased, resulting in a more conventional q-profile for currents above 800 kA. Further increases in the plasma current would result in a further drop in q_{min} as described in section 6.2.

The trends shown in figure 30 are illustrated for a much larger database of simulations in figure 31. In this figure, each column corresponds to a given heating power, while each row corresponds to a given 0D equilibrium quantity. The colour codes correspond to the confinement multiplier with regard to the $H_{98y,2}$ scaling; scenarios with $H_{98y,2}$ up to 1.3 have been examined. The different symbols correspond to different H-mode thermal profile shapes. Note that due to the large TF, the confinement multiplier with respect to the ST scaling expression (1*b*) is typically in the range 0.6–0.8.

The top row shows that scenarios with pressure-driven current fractions equal to or exceeding 80% have been identified for a wide range of heating powers, provided that the confinement multipliers are sufficiently large. At the lower powers, the required confinement multiplier is typically 1.2–1.3, while the higher power points allow high pressure-driven fraction operation with confinement multipliers closer to 1.1.

The second row of the figure shows the total non-inductive fraction. These figures confirm the results of section 6.1, that the non-inductive current level for $H_{98y,2} = 1$ confinement scaling is approximately 900 kA for $P_{inj} = 12.6$ MW (frame (*q*)), and 700 kA for $P_{inj} = 8.4$ MW (frame (*l*)). Total non-inductive fractions of up to 1.5 have been found for the 12.6 MW scenarios at 800 kA and $H_{98y,2}$ in the vicinity of 1.25.

The 3rd and 4th rows of figure 31 show metrics related to the global stability of the configurations. The value of β_N in the 3rd row increases with both heating power (compare columns) and confinement multiplier (compare colours at fixed power). The 12.6 MW cases generally have β_N above 4.5 for $H_{98y,2} > 1$, with this value dropping to $\beta_N > 3$ for the 4.2 MW cases. The pressure peaking factors, defined as the central pressure normalized to the volume-average pressure ($F_P = p_0/\langle p \rangle$), are shown in the 4th row. As expected from the NBCD trends in figure 30, there is a dramatic increase in the total pressure peaking as the plasma current is dropped.

The results to be discussed in section 8 show that the maximum stable β_N is a strong function of the pressure peaking. For instance, the cases with $P_{inj} = 12.6$ MW cases with $\beta_N > 4$ will be ideally unstable for $F_P > 3.5$. This provides an additional lower limit on the plasma current of ~800 kA and will eliminate many of the highest bootstrap fraction cases. Similar conditions apply for all the other powers, underscoring the challenge of maintaining good MHD stability in these configurations. These lower current cases do have large fast-ion energy fractions, with W_{fast}/W_{tot} exceeding 25%. It is possible that fast-particle-driven instabilities could result in a redistribution of the fast ions, decreasing the central NBCD and pressure peaking as described in relation to figure 12 and improving the global stability. However, this scenario has not been evaluated, and only the eventual experiments can determine if this beneficial modification of the fast-ion profile is possible.

The final row in figure 31 illustrates the neutral beam power absorbed by the plasma. As the plasma current is lowered, the beam loss power due to orbit loss and charge exchange increase rapidly. This power would go to heating and sputtering of in-vessel components, and may provide an additional lower limit on the plasma current.

In summary, equilibria with pressure-driven current fractions approaching or exceeding unity have been found for NSTX-Upgrade beam heated scenarios. However, the loss beam power and excessive pressure peaking will likely present a significant barrier to realizing these scenarios. It appears likely that heating with HHFW will be an important component in these types of scenarios. Indeed, very high bootstrap current fractions have been found in low current plasmas with HHFW heating [162]. Simulations of these HHFW scenarios are, however, out of scope for this work.

7. Comparison of scenarios with the existing NSTX database

The scenarios discussed above represent a significant increase in device capabilities compared with the present NSTX. This increment is best illustrated by comparing the parameters of these scenarios with those already achieve in NSTX. This is facilitated by an already existing database of TRANSP analysis of high-performance discharges in NSTX, covering the 2008–2010 run campaigns [44]. The data from that database are shown in figures 32–36 as black discreet points, with the cyan points with orange boundaries corresponding to $A > 1.63$ discharges designed to study higher aspect-ratio plasmas [44]. Note that while the thermal energy content was approximately constant during the time window when these experimental points were taken, the current profile was often slowly evolving to $q_{min} < 1$ and eventual disruption.

The coloured four-cornered shapes in each of figure 32–36 correspond to a particular scenario for NSTX-Upgrade. The neutral beam configuration, Greenwald fraction, TF and target plasma boundary are the same for all points of a given shape and colour, but the plasma current may vary. The four corners correspond to the two profiles shape assumptions (broad from 142301 and narrow from 121123) and two confinement assumptions (the $H_{98y,2}$ and H_{ST} scaling expressions of equations (1*a*) and (1*b*)). Hence, each of these four-cornered shapes shows the range of operating points possible for a given set of machine parameters and scenario optimizations. All NSTX-Upgrade and NSTX data here have $f_{GW} > 0.55$.

The increased plasma current is a key capability of the upgrade. Hence, the parameters of 100% non-inductive scenarios in NSTX-Upgrade and existing NSTX data are plotted against I_P in figure 32; these data are a subset of that in table 2. The stored energy in NSTX was at most ~ 460 kJ [44]. The projected stored energies for fully non-inductive scenarios in NSTX-U range from 630–1100 kJ for the $B_T = 1$ T cases with six sources at 100 kV each, to 260–400 kJ

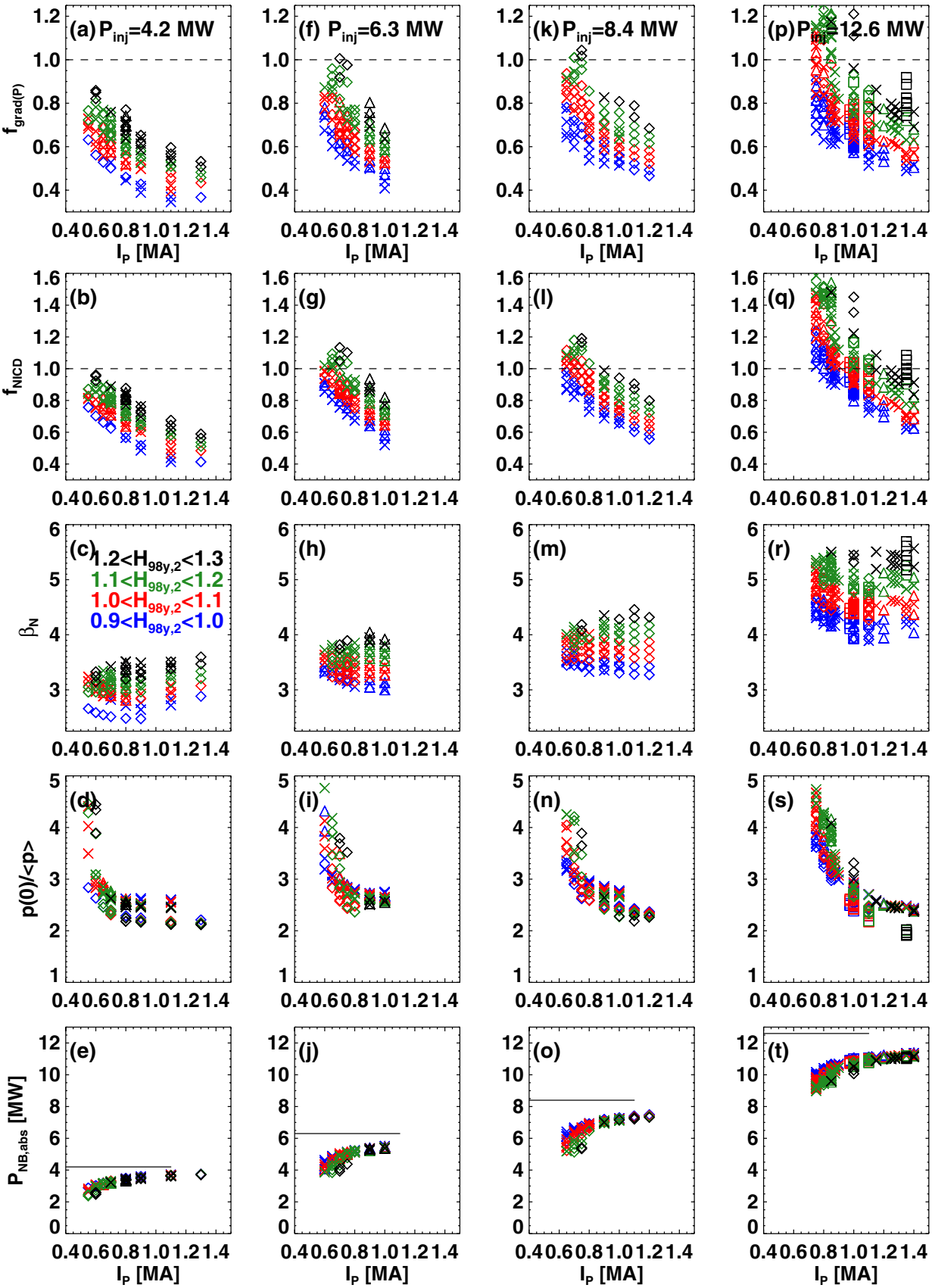

Figure 31. Various parameters as a function of the plasma current. The columns correspond the injected powers of 4.2, 6.3, 8.4 and 12.6 MW. The rows show the total pressure-drive current fraction, the total non-inductive current fraction, the normalized β, the pressure peaking, and the absorbed neutral beam power. The colour codes are indicated in frame (*c*). The horizontal lines in frames (*e*), (*j*), (*o*) and (*t*) correspond to the total injected power. See text for further details.

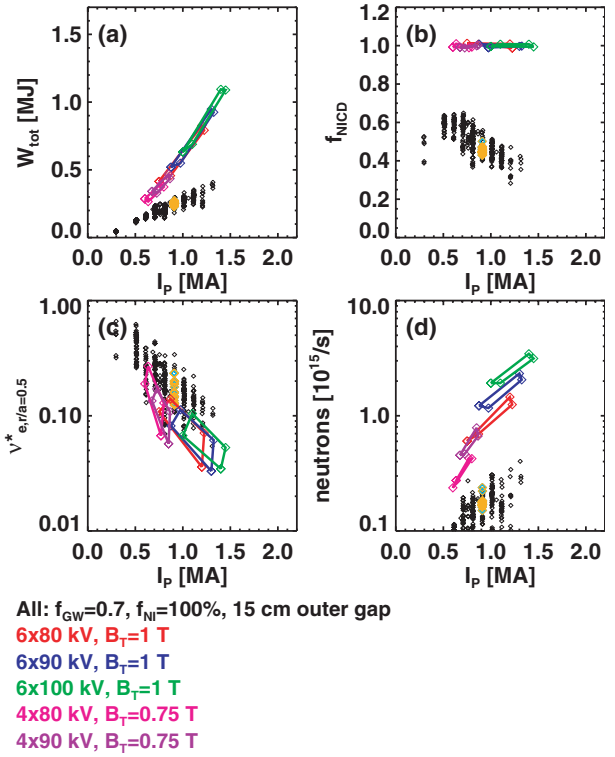

Figure 32. Comparison between 100% non-inductive scenarios for NSTX-Upgrade and achieved NSTX scenarios, as a function of plasma current. The (*a*) stored energy, (*b*) non-inductive current fraction, (*c*) midradius collisionality and (*d*) neutron emission rate, as a function of the plasma current. The black points are NSTX data at lower aspect ratio, while the cyan points with orange boundaries represent NSTX high aspect-ratio discharges designed to prototype NSTX-U.

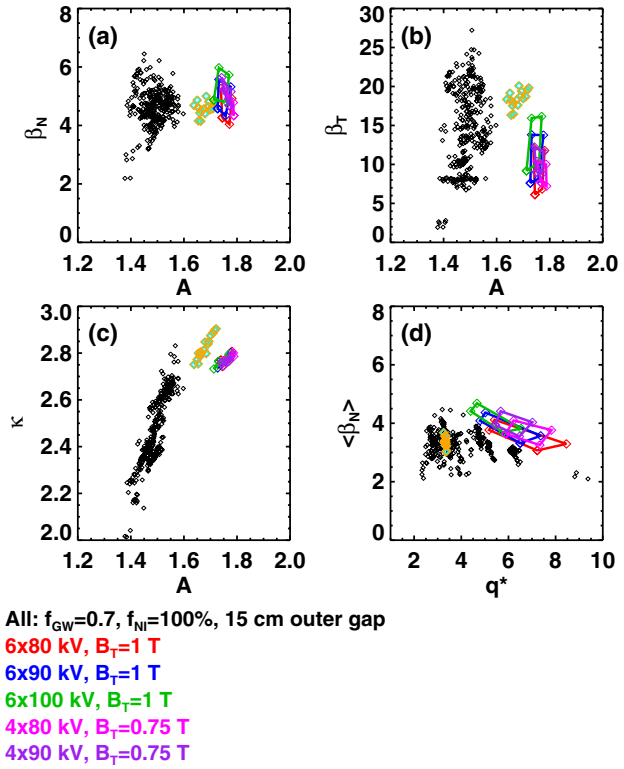

Figure 33. Comparison of stability-related parameters between 100% non-inductive scenarios for NSTX-Upgrade and achieved NSTX scenarios. Shown are the (*a*) the normalized β (β_N) versus aspect ratio, the (*b*) the toroidal β (β_T) versus aspect ratio, (*c*) the elongation versus aspect ratio and (*d*) the volume-averaged normalized β ($\langle\beta_N\rangle$) versus cylindrical safety factor. The black points are NSTX data at lower aspect ratio, while the cyan points with orange boundaries represent NSTX high aspect-ratio discharges designed to prototype NSTX-U scenarios.

for $B_T = 0.75$ T with four sources at 80 kV. The highest non-inductive fractions achieved in NSTX were 65–70%, in 700–750 kA discharges. NSTX-Upgrade is projected to achieve full non-inductive current sustainment in the range of $I_P = 1000$–1400 kA for $B_T = 1.0$ T and six 100 kV neutral beam sources, down to $I_P = 675$–865 kA for $B_T = 0.75$ T and six 80 kV neutral beam sources.

The midradius collisionality and total neutron emission are shown in figures 32(*c*) and (*d*). We see that the collisionality of these fully non-inductive upgrade scenarios is comparable to the lowest ever achieved in NSTX. The neutron emission rate is up to a factor of 10 larger than the maximum value in this database of high-performance NSTX discharges.

Some stability-related metrics for these 100% non-inductive scenarios are shown in figure 33. The most significant change related to global stability for NSTX-Upgrade is the increase in aspect ratio. As shown in figure 33(*a*), the values of β_N anticipated for these scenarios are not larger than has been achieved in many discharges in NSTX at lower aspect ratio. The larger aspect-ratio points in cyan with orange boundaries show $\beta_N \sim 4$–4.5 has been achieved without passing disruptive β limits [44], and no effort was made in that experiment to determine the maximum experimentally achievable β_N at this higher aspect ratio. The toroidal β values for these scenarios are less than the largest values achieved in NSTX, due to the comparatively large values of q_{95}.

The increased aspect ratio of the Upgrade also results in a reduction of the 'natural elongation' [1, 16, 18] of the configuration. Natural elongation refers to the elongation that the plasma cross-section would achieve in a perfectly straight vertical field, and as the natural elongation is reduced, the $n = 0$ passive stability margin is likely reduced as well. This issue was a primary motivation for the high-A NSTX-U prototype experiments described in [44]. Figure 33(*c*) shows that the 100% non-inductive scenarios presented here are at lower elongation, and only somewhat higher aspect ratio, than was already achieved in the NSTX-U prototype experiments. While this would seem to imply that these scenarios would not have trouble with vertical stability, that conclusion does not include the effects of varying profiles. In particular, the high aspect-ratio experiments in NSTX [44] determined that vertical stability is often lost for $l_i \gtrsim 0.65$ when $A > 1.7$. The value of l_i is determined by the current drive sources and thermal profiles, and the calculations in figure 18 indicate that peaked thermal profiles may result in l_i too high for stable vertical position control with the present control system [163].

A number of steps have been taken to remedy this potential vertical stability problem. An improved observer of the vertical position has been implemented in the plasma control system, utilizing additional magnetic sensors to better resolve the motion of these high-κ shapes. An algorithm

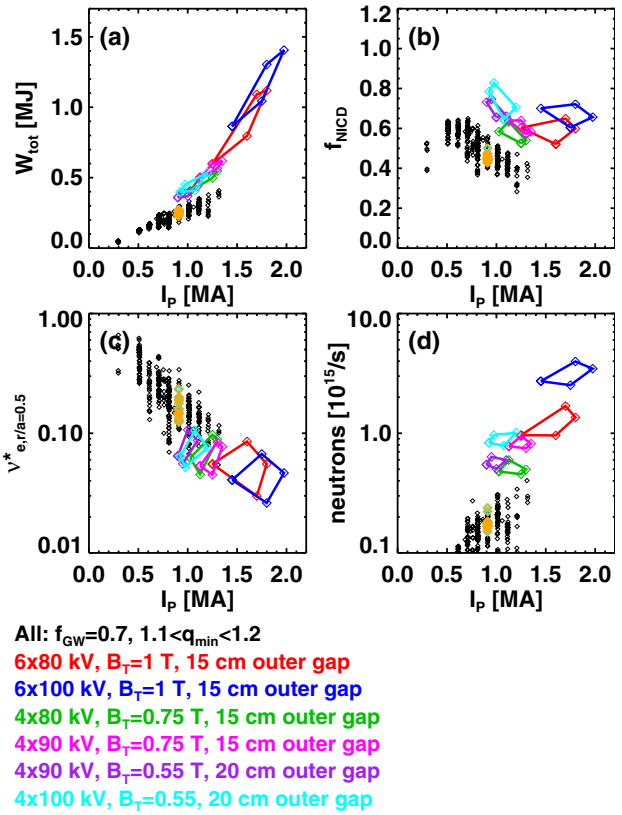

Figure 34. Comparison between $q_{min} > 1.1$, partial-inductive scenarios at $f_{GW} = 0.7$ for NSTX-Upgrade and achieved NSTX scenarios, as a function of plasma current. The quantities plotted are the same as in figure 32.

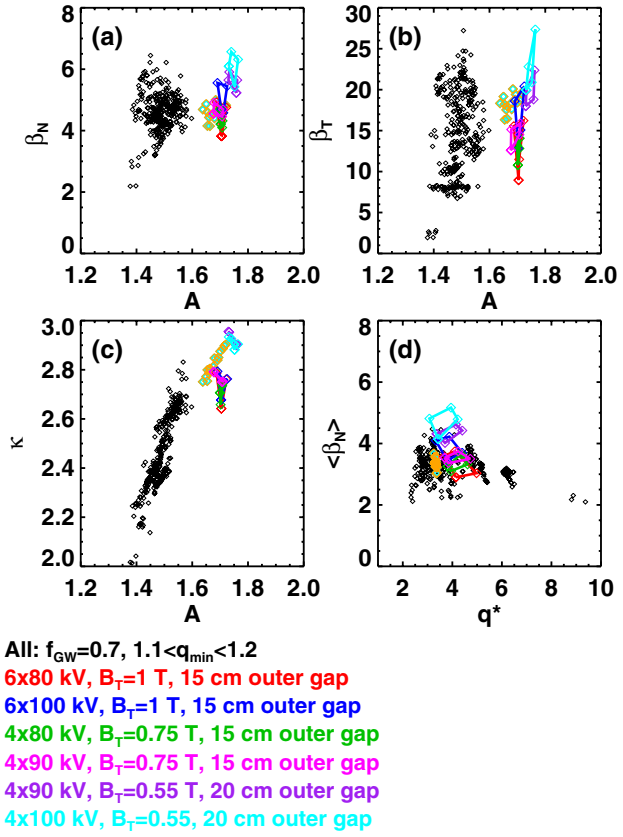

Figure 35. Global stability metrics for the $f_{GW} = 0.7$ partial-inductive scenarios in figure 34. The quantities plotted are the same as in figure 33.

has been implemented to apply radial field with the midplane RWM coils, to supplement that from the larger PF-3 coils. These midplane coils have a significantly faster response. Additionally, steps are being taken to reduce the latency in the control response of the large radial field coils. Finally, we are considering the inclusion of additional PF coils in the vertical stabilization loop.

Finally, the so-called volume-average β_N for NSTX data and NSTX-U scenarios is plotted against the cylindrical safety factor q^* in figure 31(d). As described in section 6.4, q^* has been previously identified as a good aspect-ratio independent measure of the current limit [135], with the no-wall β_N limit dropping precipitously for $q^* < 1.8$. Further, the volume average β_N, denoted $\langle\beta_N\rangle$, is defined as $\langle\beta_N\rangle = \langle\beta_T\rangle I_P a/B_{T0}$, with $\langle\beta_T\rangle = \langle p\rangle 2\mu_0/\langle B^2\rangle$. Reference [135] shows that $\langle\beta_N\rangle$ is a good aspect-ratio independent indicator of the no-wall stability limit. The data in figure 33(d) show that these 100% non-inductive scenarios optimize to rather high q^*, significantly above most of the NSTX data in the database and well away from the low-q limit. The values of $\langle\beta_N\rangle$ are comparable to, or, in the case with six 100 kV beams injecting 15.6 MW, only slightly higher than has been achieved in many occasions in NSTX.

We next consider the high-current partial-inductive scenarios at $f_{GW} = 0.7$, and $B_T = 1.0$, 0.75, and 0.55. As described in sections 6.2 and 6.4, these scenarios were designed to find the highest current for each TF, heating scheme, Greenwald fraction, and confinement and profile assumption, consistent with a relaxed $q_{min} > 1.1$. The 0.55 T cases in section 6.4 were also run with a large outer gap of 20 cm, in order to maximize the elongation and off-axis current drive.

Figure 34 shows the parameters of these partial-inductive cases as a function of plasma current. The stored energy of these scenarios is vastly higher than the present NSTX cases, exceeding 1.4 MJ for the most favourable cases with six 100 kV beams ($P_{inj} = 15.6$ MW) at $I_P = 1.975$ MA and $B_T = 1$ T. Interestingly, these Upgrade scenarios have substantially higher non-inductive fractions than the NSTX cases at the same plasma current, due to the increase in both the beam current drive and the TF. The collisionality is shown on a log scale in figure 34(c), and generally decreases along the trend of the existing NSTX data. Note that the higher Greenwald fractions in these scenarios, desired for keeping q_{min} elevated, tend to increase the collisionality, and a scenario with lower collisionality will be discussed below. Finally, the neutron emission is 10–15 times larger than in the present NSTX scenarios.

The global stability metrics of these $f_{GW} = 0.7$ partial-inductive scenarios are shown in figure 35. Figure 35(a) shows that the $B_T = 1$ and 0.75 T scenarios generally have β_N values comparable to those already achieved, while the 0.55 T case pushes to higher values. This contrast is made more clear in figure 35(d) where the values of $\langle\beta_N\rangle$ for the $B_T = 0.55$ T, 100 kV cases are significantly in excess of previous achievements. The value of β_T in figure 35(b) are comparable to that achieved in NSTX. However, all the highest

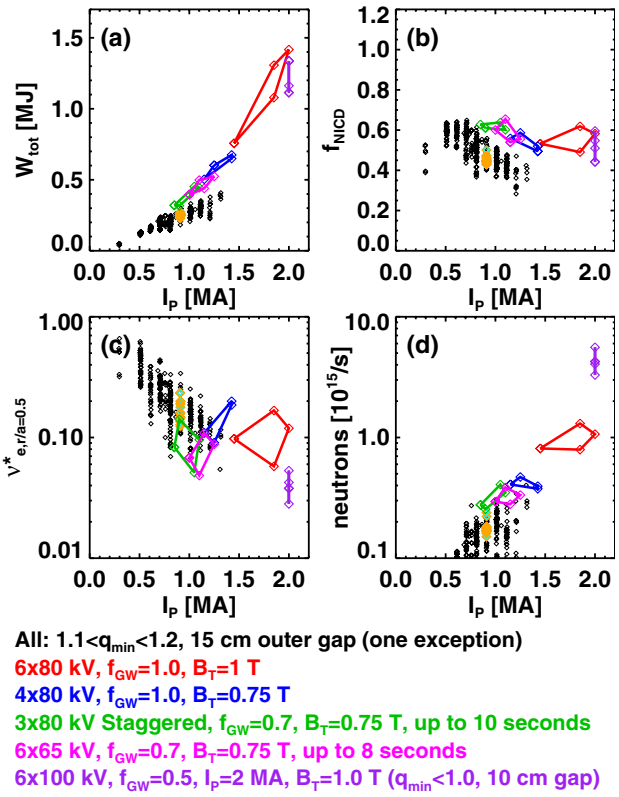

Figure 36. Comparison between various partial-inductive scenarios for NSTX-Upgrade and achieved NSTX scenarios, as a function of plasma current. The quantities plotted are the same as in figure 32. See text for additional details.

β_T experimental points in that figure have q_{min} evolving to less than unity, while the NSTX-Upgrade scenarios maintain $q_{min} > 1.1$. The values of aspect ratio and elongation in figure 35(*c*) are not an extension beyond that already achieved, except for the $B_T = 0.55$ scenarios at higher elongation of 2.8–3.0; the vertical stability of these configurations will be impacted by the profile shapes, as discussed above. It is clear that these $B_T = 0.55$ scenarios will provide a severe test of $n = 0$ and $n = 1$ stability control.

The performance parameters for a number of additional partial-inductive scenarios are considered as a function of the plasma current in figure 36. The first two cases are the $f_{GW} = 1.0$, $E_{inj} = 80$ kV scenarios at $B_T = 1.0$ and 0.75 T, discussed in section 6.2. These are designed to achieve the longest possible pulses with 80 kV beams for high values of plasma current. For $B_T = 1.0$, the device goal of 2 MA can be sustained with $q_{min} > 1$ for 5 s with six 80 kV beams, provided that the confinement and profiles are sufficiently favourable. These scenarios have stored energies of ~1 MJ with 50–60% of the current generated non-inductively, but with comparatively high collisionality. For $B_T = 0.75$ T and $f_{GW} = 1.0$, current levels of up to 1.425 MA can be sustained with $q_{min} > 1.1$ using four 80 kV beams for the 5 s heating pulse duration

We also show in this figure parameters for the very long-pulse configurations described in section 6.3, designed to operate with pulse lengths of 8–10 s. Both the scenarios with six 65 kV beams or staggered triplets of 80 kV beams have stored energies comparable to or larger than the best previously achieved in NSTX, with non-inductive fractions significantly larger than in NSTX for the given values of the plasma current. The collisionality tends to be on the low end of that already achieved in NSTX, with neutron emission rates comparable to the largest typically achieved.

Finally, a key programmatic goal of NSTX-U is to achieve reduced collisionality for electron transport and MHD stability studies. It is clear that the achievement of low collisionality is facilitated by reducing the plasma density, increasing the neutral beam power, and operating at high field and current. We show in figure 36 the parameters for an $I_P = 2$ MA, $B_T = 1$ T, $f_{GW} = 0.55$ scenario heated by six 100 kV beams. With the higher current, the central safety factor evolves to be less than 1; recall that it is only the fully evolved state which is computed in this modelling. This q_{min} value is likely unrealistic, due to the MHD activity that would onset as q_{min} approached 1 in a real discharge. Hence, for these calculations, the midradius collisionality computed by TRANSP is multiplied by $f = 1.15/q_{min}$ for all cases where $q_{min} < 1.15$, the assumption being that the lowest collisionality point in the actual experiment will be just before q_{min} reaches an unstable value. The lowest midradius collisionality so computed is a factor of 2 less than that achieved in NSTX or the other NSTX-Upgrade scenarios. These scenarios also have the highest neutron emission of any studies here. Note that the current penetration time is in the range $\tau_{CR} = 0.9$–1.1 s for these scenarios, compared with heating pulse durations of 1.5 s. Hence, it should be possible to complete the necessary physics studies and terminate the discharge before the evolution of q_{min} results in the crossing of a stability boundary. Note also that the Greenwald fraction was limited to $f_{GW} > 0.55$ in these calculations; operation at lower values of f_{GW} will result in a further significant reduction in collisionality.

8. Summary and discussion

This paper has documented many of the key elements in developing scenarios for NSTX-Upgrade. Key among them include:

- We generally find a comparatively large outer gap to be advantageous for the scenario; a value of 15 cm appears optimal in most circumstances for elevating q_{min} without producing unacceptable shine-though loss of the largest tangency-radius beam.
- The plasma density plays a key role in determining the central safety factor. For the scenarios discussed here, Greenwald fractions less that 0.65–0.75 generally result in $q_{min} < 1$.
- Modest levels of anomalous fast-ion diffusivity ($D_{FI} < 1\,m^2\,s^{-1}$) would not pose a significant problem for the scenarios discussed here. In cases where there is significant on-axis NBCD, small anomalous diffusivity values reduce the central current drive, raise q_{min}, and decrease the pressure peaking. This in turn assists the stability properties, though at the expense of somewhat reduced total beam current drive and non-inductive fraction.
- Increases in the thermal ion transport or Z_{eff} compared with the values assumed in the simulations will typically not have a deleterious effect on the scenario, provided that the global confinement is maintained.

- The thermal profile pressure peaking plays a key role in determining $q_{\min}$ and l_i, with broad profiles providing favourable equilibrium and stability properties.

In addition, this paper has documented a large number of fully equilibrated plasma scenarios that can assist in physics explorations relevant to next-step STs. These include the following.

- There are a large number of scenarios with 100% of the plasma current driven non-inductively. For $B_T = 1.0$ T, we have identified such scenarios with currents ranging from 750 to 1450 kA, depending on the beam voltage, profile shapes and confinement assumptions. For $B_T = 0.75$ T scenarios, the equivalent range is 635–850 kA. These scenarios should allow the study of transport and stability with fully equilibrated, 100% non-inductive current drive. See section 6.1 and table 2.
- High-current partial-inductive scenarios with fully relaxed $q_{\min} > 1.1$ were studied, in order to examine the long-pulse high-current capabilities of the device. For $f_{GW} = 0.7$ and $B_T = 1.0$ T, configurations with currents in the range $1300 < I_P < 1800$ kA can be sustained for 5 s, while $1500 < I_P < 2000$ can be sustained for 1.5 s. As before, the ranges on the plasma current are due to the different heating system used and various assumptions regarding the profile shapes and global confinement. These scenarios will allow the study of stability, transport, divertor, and SOL physics at higher current and significantly reduced collisionality. See section 6.2 and table 3.
- Scenarios exist with the potential for 8–10 s pulse duration, albeit at reduced plasma currents of 850–1250 kA. These scenarios use either six neutral beams with 65 kV acceleration voltage, or 80 kV beams modulated so that only three sources are on at any time. These scenarios should allow studies of particle transport and disruption avoidance for long pulse. See section 6.3 and table 4.
- By further increasing the elongation compared with those in the previous cases, very high β_T scenarios with relaxed $q_{\min} > 1.1$ can be achieved. Typical values are $18\% < \beta_T < 20\%$ with $I_P = 900$–1200 kA at $B_T = 0.55$ T. These scenarios will allow the study of MHD control with strong shaping and high β_N. See section 6.4 and table 5.
- The safety factor profile can be modified by varying the beam mix at fixed shape, density, and heating power. For instance, at $B_T = 1.0$ T, $q_{\min}$ can be changed between 1.1 and 2.5 with $P_{inj} = 8.4$ MW and $I_P = 800$ kA by choosing various combinations of four neutral beam sources. These scenarios will allow studies of the optimal current profile for MHD stability and transport, as will as provide a basis for q-profile control using the neutral beam as an actuator. See section 6.5 and table 6.

When considered as a complete set, the large database of equilibria and stability calculations allows an assessment of the 'typical' ideal MHD $n = 1$ no-wall and with-wall β_N limits for NSTX-Upgrade scenarios. An example of this calculation is shown in figure 37, where β_N is plotted against the total pressure peaking factor. Red points are indicative of unstable configurations, while green points indicate stability. These

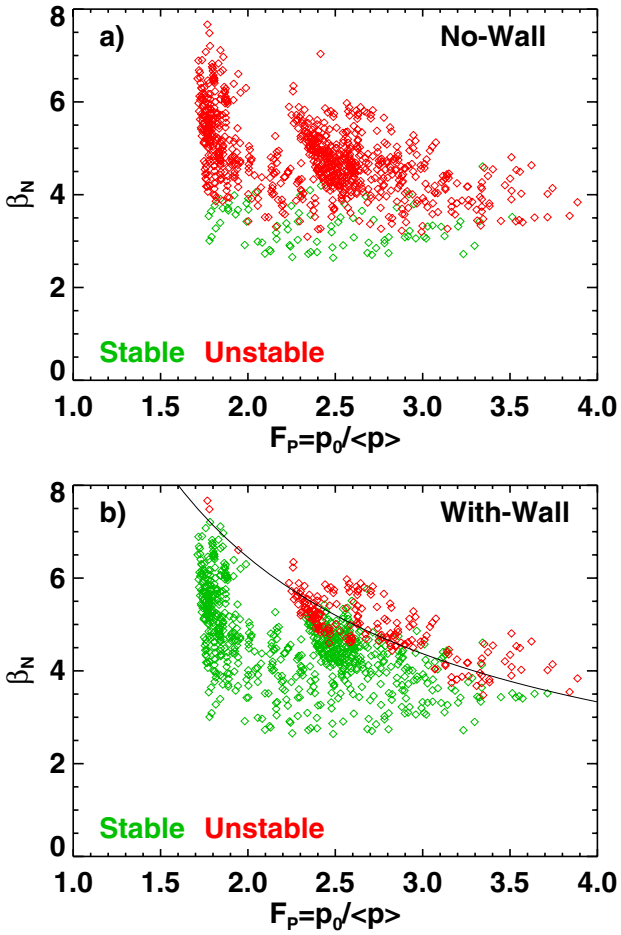

Figure 37. Plots of the normalized-β versus total pressure peaking factor. The colours are indicative of the $n = 1$ ideal stability, without a wall in (a) and with an ideally conducting wall at the location of the passive plates in (b).

points come from a variety of scenarios, for instance, with $0.35 < f_{NI} < 1.2$ and $1.1 < q_{\min} < 3.7$.

Frame (a) shows the results without any conducting walls in the vicinity of the plasma. The β_N limit in this case is generally in the vicinity of 3.5, which is a substantial reduction compared with the more typical NSTX values of 4.0–4.5 [36, 44] due to the increase in the aspect ratio [44, 135]. More importantly, the vast majority of points fall in the unstable regime. Figure 35(b) shows the same data, but with a conducting wall included in the stability analysis. The majority of points in these cases are now stable. There is also a clear dependence of the stability boundary on the pressure peaking, in this case parametrized as $0.2 + 12.5/F_P$. Stable configurations with $\beta_N = 7$ have been found when the pressure peaking is sufficiently low. These two frames make it clear that RWM stability, either passively [147–151] or via feedback [41, 140, 143, 144] will be critical for high-performance operation.

As is clear from the discussion in sections 3 and 5, there are a number of ways that this modelling could be improved. The obvious potential improvement is to use a validated model for the electron thermal transport. This could result in substantial modifications to some results in this paper. For instance, the cases with reversed shear could lead

to the formation of internal transport barriers. A validated electron transport model could also provide more reasonable expectations about the equilibrium trends with Z_{eff}. Work is presently underway to compare non-linear transport estimates from micro-turbulence with NSTX experimental fluxes [88]. However, considerable progress is required before a validated reduced transport model is available for scenario modelling purposes.

The stability modelling described in this paper is also insufficient to guarantee globally stable scenarios. Given that virtually all scenarios have β_N greater than the no-wall limit, resistive wall mode stability is a factor. Calculation of RWM stability is an area of active research, and has not been attempted for these scenarios. Those calculations would require knowledge of the fast-particle population (which is included in the context of the TRANSP runs), but also a prediction of the rotation profile. This in turn emphasizes the needs for proper reduced transport models. We also note that while this paper has focused on scenarios with $q_{min} > 1.1$ for the avoidance of non-resonant core kinks, the actual required increment of q_{min} above 1 will likely increase with aspect ratio [119], and depend on quantities like the rotation shear, magnetic shear, and possibly the energetic particle population.

This work has also treated non-classical fast-ion transport in a simplified way, with spatially and temporally constant fast-ion diffusivity. As noted in section 5, large TAE avalanches are documented to have a major effect on the current profile [43], severely reducing the central NB current drive. Furthermore, these modes may directly or indirectly modify the spectrum of low-frequency disruptive MHD. The onset conditions for these modes has not been documented in a way that allows their existence in these scenarios to be predicted. However, the scenarios discussed here often have small values of fast-ion β and large values of the plasma density, which should make these modes more stable.

We finally note that these calculations have generally assumed that the divertor will tolerate the power fluxes for pulses of the given duration, without deleteriously impacting the core performance. Accomplishing these divertor solutions, and studying their compatibility with the high-performance plasma core, will be a major part of the research program. Candidate solutions under consideration include partial detachment [164, 165] or snowflake divertors [47, 166–168].

Acknowledgments

The authors would like to thank the TRANSP team for their assistance in these simulations. In particular, we are grateful for the support provided by the late Doug McCune. We would also like to thank S. Kaye and W. Guttenfelder for helpful discussion. This research was funded by the United States Department of Energy under contract DE-AC02-09CH11466.

Appendix

The tables in this paper utilize data from given runs of the TRANSP code. Each run of the code is indicated by the shot number and a 'run-ID' given by a letter and two number, for instance 'A12' or 'Z52'. The TRANSP runs, and the times during each run run, are indicated in the tables below.

Table A1. TRANSP runs and basic parameters corresponding to the data in table 2.

Shot	ID	t_{min}	t_{max}	I_p (kA)	B_T (T)	P_{inj} (MW)	f_{GW}	$H_{98y,2}$	H_{ST}	q_{min}	f_{NICD}	l_i	A	κ
142301	H56	11.8	11.95	870	0.99	10.20	0.72	1.03	0.70	1.60	1.01	0.50	1.77	2.78
142301	E77	11.8	11.95	1225	0.99	10.20	0.70	1.31	0.99	2.37	0.99	0.40	1.78	2.81
121123	K34	11.8	11.95	750	1.00	10.20	0.72	1.00	0.63	1.41	1.01	0.70	1.74	2.74
121123	N22	11.8	11.95	1200	1.00	10.20	0.70	1.40	1.02	2.48	1.01	0.63	1.74	2.77
142301	B85	11.8	11.95	975	0.99	12.60	0.72	1.00	0.70	1.50	0.99	0.54	1.76	2.76
142301	E72	11.8	11.95	1325	0.99	12.60	0.70	1.27	1.00	2.03	1.00	0.42	1.78	2.80
121123	R42	11.8	11.95	875	1.00	12.60	0.73	1.01	0.66	1.39	1.01	0.75	1.73	2.74
121123	Q62	11.8	11.95	1300	1.00	12.60	0.71	1.34	1.00	2.10	1.00	0.66	1.73	2.76
142301	D46	15.8	15.95	1100	0.99	15.60	0.77	1.01	0.74	1.52	1.01	0.52	1.76	2.77
142301	Y93	11.8	11.95	1450	1.00	15.60	0.71	1.24	1.00	1.76	0.99	0.44	1.77	2.80
121123	J26	11.8	11.95	1000	1.00	15.60	0.74	0.98	0.67	1.31	1.00	0.80	1.71	2.73
121123	K96	11.8	11.95	1400	1.01	15.60	0.71	1.30	1.00	1.82	1.01	0.67	1.73	2.76
142301	V91	11.8	11.95	635	0.74	6.80	0.72	1.00	0.80	0.98	1.01	0.45	1.79	2.79
142301	U76	11.8	11.95	800	0.74	6.80	0.71	1.17	1.00	1.53	0.99	0.42	1.79	2.80
121123	Q03	11.8	11.95	600	0.74	6.80	0.71	1.00	0.77	0.81	0.99	0.59	1.77	2.76
121123	Q52	11.8	11.95	770	0.75	6.80	0.70	1.22	0.99	1.72	0.99	0.61	1.75	2.77
142301	E55	11.8	11.95	725	0.74	8.40	0.72	0.99	0.82	1.10	0.99	0.52	1.77	2.77
142301	B58	11.8	11.95	865	0.74	8.40	0.71	1.14	1.00	1.36	1.00	0.46	1.78	2.79
121123	B90	11.8	11.95	675	0.74	8.40	0.72	1.00	0.79	0.90	0.99	0.68	1.75	2.75
121123	D48	11.8	11.95	850	0.75	8.40	0.71	1.20	1.01	1.54	1.00	0.65	1.74	2.76

Table A2. TRANSP runs and basic parameters corresponding to the data in table 3.

Shot	ID	t_{min}	t_{max}	I_p (kA)	B_T (T)	P_{inj} (MW)	f_{GW}	$H_{98y,2}$	H_{ST}	q_{min}	f_{NICD}	l_i	A	κ
142301	E34	11.8	11.95	1600	1.01	10.20	0.74	1.00	0.78	1.14	0.52	0.57	1.71	2.74
142301	H47	11.8	11.95	1800	1.01	10.20	0.73	1.22	1.00	1.16	0.60	0.51	1.72	2.76
121123	B12	11.8	11.95	1250	1.01	10.20	0.73	1.00	0.68	1.19	0.60	0.83	1.70	2.64
121123	K70	11.8	11.95	1700	1.01	10.20	0.74	1.28	1.00	1.10	0.65	0.77	1.69	2.79
142301	J82	11.8	11.95	1700	1.01	12.60	0.74	1.01	0.81	1.09	0.56	0.56	1.71	2.73
142301	J92	11.8	11.95	1900	1.01	12.60	0.73	1.19	1.01	1.10	0.62	0.51	1.72	2.76
121123	N93	11.8	11.95	1350	1.01	12.60	0.73	1.01	0.72	1.17	0.65	0.83	1.70	2.66
121123	N39	11.8	11.95	1750	1.01	12.60	0.74	1.24	0.99	1.12	0.68	0.77	1.69	2.79
142301	J86	11.8	11.95	1750	1.01	15.60	0.74	0.99	0.81	1.11	0.60	0.56	1.71	2.75
142301	M16	11.8	11.95	1975	1.01	15.60	0.73	1.16	1.00	1.12	0.66	0.51	1.73	2.76
121123	J93	11.8	11.95	1450	1.01	15.60	0.73	1.01	0.75	1.16	0.70	0.82	1.70	2.68
121123	K55	11.8	11.95	1800	1.01	15.60	0.74	1.20	0.98	1.13	0.72	0.77	1.69	2.79
142301	W93	11.8	11.95	1250	0.76	6.80	0.74	1.00	0.92	1.12	0.53	0.57	1.71	2.74
142301	W88	11.8	11.95	1300	0.76	6.80	0.74	1.05	0.98	1.10	0.54	0.56	1.71	2.74
121123	D06	11.8	11.95	1025	0.76	6.80	0.73	1.01	0.83	1.10	0.58	0.84	1.70	2.66
121123	R32	11.8	11.95	1125	0.76	6.80	0.73	1.14	0.98	1.15	0.63	0.80	1.70	2.71
142301	W84	11.8	11.95	1300	0.76	8.40	0.74	1.00	0.94	1.14	0.57	0.57	1.71	2.75
142301	C15	11.8	11.95	1350	0.76	8.40	0.74	1.05	1.01	1.11	0.58	0.56	1.71	2.75
121123	Q42	11.8	11.95	1125	0.76	8.40	0.75	1.01	0.89	1.19	0.64	0.84	1.68	2.79
121123	B96	11.8	11.95	1250	0.76	8.40	0.75	1.09	1.00	1.08	0.64	0.82	1.68	2.79
142301	E59	3.8	3.95	1850	1.01	10.20	1.05	1.00	0.81	1.12	0.49	0.52	1.72	2.74
142301	O46	3.8	3.95	2000	1.00	10.20	1.03	1.19	1.01	1.24	0.58	0.47	1.73	2.77
121123	Q16	3.8	3.95	1450	1.01	10.20	1.03	0.99	0.70	1.14	0.53	0.78	1.71	2.64
121123	D18	3.8	3.95	1850	1.01	10.20	1.04	1.25	0.99	1.12	0.62	0.72	1.70	2.74
142301	E81	3.8	3.95	1425	0.76	6.80	1.05	0.99	0.95	1.13	0.49	0.52	1.72	2.75
142301	E83	3.8	3.95	1425	0.76	6.80	1.05	1.03	1.00	1.18	0.52	0.51	1.72	2.76
121123	Q39	3.8	3.95	1150	0.76	6.80	1.04	1.03	0.88	1.17	0.56	0.78	1.70	2.70
121123	Q29	3.8	3.95	1250	0.76	6.80	1.04	1.11	0.99	1.15	0.59	0.76	1.70	2.72

Table A3. TRANSP runs and basic parameters corresponding to the data in table 4.

Shot	ID	t_{min}	t_{max}	I_p (kA)	B_T (T)	P_{inj} (MW)	f_{GW}	$H_{98y,2}$	H_{ST}	q_{min}	l_i	f_{NICD}	A	κ
142301	W29	11.8	11.95	1150	0.76	6.60	0.74	0.99	0.89	1.25	0.54	0.56	1.71	2.75
142301	V21	11.8	11.95	1250	0.76	6.60	0.74	1.07	0.99	1.16	0.56	0.55	1.71	2.75
121123	K51	11.8	11.95	1000	0.76	6.60	0.75	0.99	0.83	1.24	0.60	0.83	1.68	2.79
121123	J38	11.8	11.95	1100	0.76	6.60	0.74	1.15	1.00	1.27	0.66	0.78	1.69	2.80
142301	L89	13.8	14.8	900	0.75	5.10	0.74	1.00	0.83	1.58	0.61	0.55	1.72	2.75
142301	L94	13.8	14.8	1100	0.75	5.10	0.73	1.14	1.01	1.37	0.60	0.53	1.72	2.76
121123	N80	13.8	14.8	850	0.76	5.10	0.75	1.01	0.80	1.39	0.63	0.81	1.69	2.79
121123	N75	13.8	14.8	1050	0.76	5.10	0.74	1.19	1.01	1.23	0.64	0.80	1.69	2.79

Table A4. TRANSP runs and basic parameters corresponding to the data in table 5.

Shot	ID	t_{min}	t_{max}	I_p (kA)	B_T (T)	P_{inj} (MW)	f_{GW}	$H_{98y,2}$	H_{ST}	q_{min}	f_{NICD}	l_i	A	κ
142301	S94	11.8	11.95	1100	0.55	8.40	0.74	0.98	1.15	1.15	0.66	0.54	1.76	2.90
142301	S39	11.8	11.95	1000	0.55	8.40	0.74	0.91	1.03	1.24	0.66	0.56	1.76	2.90
121123	Q65	11.8	11.95	950	0.56	8.40	0.74	1.00	1.09	1.20	0.75	0.79	1.73	2.95
121123	K15	11.8	11.95	900	0.56	8.40	0.75	0.94	1.01	1.21	0.73	0.81	1.73	2.96
142301	R77	11.8	11.95	1200	0.55	10.40	0.74	0.99	1.21	1.09	0.71	0.54	1.76	2.90
142301	M08	11.8	11.95	1075	0.56	10.40	0.74	0.85	0.99	1.08	0.64	0.59	1.75	2.88
121123	Q72	11.8	11.95	975	0.56	10.40	0.74	1.01	1.13	1.11	0.83	0.78	1.74	2.93
121123	Q83	11.8	11.95	925	0.56	10.40	0.75	0.92	1.01	1.10	0.78	0.82	1.73	2.93

Table A5. TRANSP runs and basic parameters corresponding to the data in table 6.

Shot	ID	t_{min}	t_{max}	I_p (kA)	B_T (T)	P_{inj} (MW)	f_{GW}	$H_{98y,2}$	H_{ST}	q_{min}	f_{NICD}	l_i	A	κ
142301	F83	15.8	15.95	675	0.98	8.40	0.71	0.98	0.61	1.88	1.00	0.42	1.79	2.80
142301	K79	11.8	11.95	740	0.99	8.40	0.72	1.00	0.64	1.55	1.02	0.48	1.78	2.78
142301	B37	11.8	11.95	770	0.99	8.40	0.73	1.00	0.65	1.03	1.01	0.52	1.77	2.76
142301	F66	15.8	15.95	800	0.99	8.40	0.73	0.99	0.64	1.51	1.00	0.56	1.76	2.76
142301	U84	11.8	11.95	800	0.99	8.40	0.71	1.00	0.65	2.47	0.87	0.48	1.77	2.78
142301	U85	11.8	11.95	800	0.99	8.40	0.72	0.99	0.64	2.11	0.92	0.51	1.76	2.77
142301	F62	15.8	15.95	800	0.99	8.40	0.73	1.01	0.66	1.11	0.98	0.52	1.77	2.76
142301	F66	15.8	15.95	800	0.99	8.40	0.73	0.99	0.64	1.51	1.00	0.56	1.76	2.76
142301	Q91	11.8	11.95	650	0.74	8.40	0.71	0.99	0.80	1.23	1.01	0.43	1.79	2.80
142301	E55	11.8	11.95	725	0.74	8.40	0.72	0.99	0.82	1.10	0.99	0.52	1.77	2.77
142301	M21	11.8	11.95	765	0.74	8.40	0.73	1.00	0.84	0.68	0.99	0.55	1.76	2.75
142301	C50	15.8	15.95	775	0.74	8.40	0.73	0.99	0.82	0.93	1.00	0.59	1.75	2.75
142301	M32	11.8	11.95	800	0.75	8.40	0.72	1.00	0.84	1.77	0.85	0.50	1.76	2.78
142301	M42	11.8	11.95	800	0.75	8.40	0.72	1.00	0.84	1.46	0.89	0.53	1.76	2.77
142301	M26	11.8	11.95	800	0.74	8.40	0.73	1.00	0.84	0.79	0.93	0.56	1.75	2.75
142301	G89	11.8	11.95	800	0.74	8.40	0.73	1.00	0.84	1.00	0.99	0.58	1.75	2.75

References

[1] Peng Y.K.M. and Strickler D.J. 1986 *Nucl. Fusion* **26** 769
[2] Goldston R.J. *et al* 2008 *Proc. 22nd Int. Conf. on Fusion Energy 2008 (Geneva, Switzerland, 2008)* (Vienna: IAEA) FT/P3-12 and http://www-naweb.iaea.org/napc/physics/FEC/FEC2008/html/index.htm
[3] Abdou M. 1995 *Fusion Eng. Des.* **27** 111
[4] Peng Y.-K.M. *et al* 2005 *Plasma Phys. Control. Fusion* **47** B263
[5] Wilson H.R. *et al* 2004 *Proc. 20th Int. Conf. on Fusion Energy 2004 (Vilamoura, Portugal, 2004)* (Vienna: IAEA) FT/3-1Ra and http://www-naweb.iaea.org/napc/physics/fec/fec2004/datasets/index.html
[6] Voss G.M. *et al* 2008 *Fusion Eng. Des.* **83** 1648
[7] Peng Y.-K.M. *et al* 2008 *Proc. 22nd Int. Conf. on Fusion Energy 2008 (Geneva, Switzerland)* (Vienna: IAEA) FT/P3-14 and http://www-naweb.iaea.org/napc/physics/FEC/FEC2008/html/index.htm
[8] Peng Y.-K.M. *et al* 2009 *Fusion Sci. Technol.* **56** 957
[9] Peng Y.-K.M. *et al* 2010 *Proc. 23rd Int. Conf. on Fusion Energy 2010 (Daejeon, Korea, 2010)* (Vienna: IAEA) CD-ROM file FT/P2-Ra and http://www-naweb.iaea.org/napc/physics/FEC/FEC2010/html/index.htm
[10] Stambaugh R.D. *et al* 2010 Candidates for a Fusion Nuclear Science Facility (FDF and ST-CTF) *37th EPS Conf. on Plasma Physics (Dublin, Ireland, 2010)* paper P2.110 and http://ocs.ciemat.es/EPS2010PAP/pdf/P2.110.pdf
[11] Stambaugh R.D. *et al* 1998 *Fusion Technol.* **33** 1
[12] Akers R.J. *et al* 2000 *Nucl. Fusion* **40** 1223
[13] Najmabadi F. and the ARIES Team 2003 *Fusion Eng. Des.* **65** 143
[14] Wilson H.R. *et al* 2004 *Nucl. Fusion* **44** 917
[15] Menard J.E. *et al* 2011 *Nucl. Fusion* **51** 103014
[16] Roberto M. 1992 *Nucl. Fusion* **32** 1666
[17] Miller R.L. *et al* 1997 *Phys. Plasmas* **4** 1783
[18] Menard J.E. *et al* 1997 *Nucl. Fusion* **37** 595
[19] Ono M. *et al* 2000 *Nucl. Fusion* **40** 557
[20] Sykes A. *et al* 2001 *Nucl. Fusion* **41** 11
[21] Kaye S.M. *et al* 2006 *Nucl. Fusion* **46** 848
[22] Kaye S.M. *et al* 2007 *Phys. Rev. Lett.* **98** 175002
[23] Kaye S.M. *et al* 2007 *Nucl. Fusion* **47** 499
[24] Valovic M. *et al* 2009 *Nucl. Fusion* **49** 075016
[25] Valovic M. *et al* 2011 *Nucl. Fusion* **51** 073045
[26] Gorelenkov N.N. *et al* 2004 *Phys. Plasmas* **11** 2586
[27] Fredrickson E.D. *et al* 2004 *Phys. Plasmas* **11** 3563
[28] Gryaznevich M.P. and Sharapov S.E. 2004 *Plasma Phys. Control. Fusion* **46** S15
[29] Fredrickson E.D. *et al* 2005 Scaling of kinetic instability induced fast ion losses in NSTX *32nd EPS Plasma Physics Conf. (Tarragona, Spain, 2005)* paper P1.061 and http://epsppd.epfl.ch/Tarragona/pdf/P1_061.pdf
[30] Sharapov S.E. *et al* 2005 *Nucl. Fusion* **45** 1168
[31] Fredrickson E.D. *et al* 2006 *Nucl. Fusion* **46** S926
[32] Fredrickson E.D. *et al* 2006 *Phys. Plasmas* **13** 056109
[33] Gryaznevich M. *et al* 2008 *Nucl. Fusion* **48** 084003
[34] Podesta M. *et al* 2009 *Phys. Plasmas* **16** 056104
[35] Fredrickson E.D. *et al* 2009 *Phys. Plasmas* **16** 122505
[36] Menard J.E. *et al* 2006 *Phys. Rev. Lett* **97** 095002
[37] Gates D.A. *et al* 2006 *Phys. Plasmas* **13** 056122
[38] Menard J.E. *et al* 2007 *Nucl. Fusion* **47** S645
[39] Gates D.A. *et al* 2007 *Nucl. Fusion* **47** 1376
[40] Gates D.A. *et al* 2009 *Nucl. Fusion* **49** 104016
[41] Menard J.E. *et al* 2010 *Nucl. Fusion* **50** 045008
[42] Gerhardt S.P. *et al* 2010 *Plasma Phys. Control. Fusion* **52** 104003
[43] Gerhardt S.P. *et al* 2011 *Nucl. Fusion* **51** 012001
[44] Gerhardt S.P. *et al* 2011 *Nucl. Fusion* **51** 073031
[45] Buttery R. *et al* 2004 *Nucl. Fusion* **44** 1027
[46] Chapman I.T. *et al* 2011 *Nucl. Fusion* **51** 073040
[47] Menard J.E. *et al* 2012 *Nucl. Fusion* **52** 083015
[48] Stevenson T. *et al* 2002 A neutral beam injector upgrade for NSTX *PPPL Report* 3651
[49] Grisham L. *et al* 1987 *Nucl. Instrum. Methods Phys. Res.* B **24/25** 741
[50] Grisham L.R. for the TFTR group 1994 *Plasma Devices Oper.* **3** 187
[51] Grisham L. *et al* 1995 *Nucl. Instrum. Methods Phys. Res.* B **99** 353
[52] Suzuki T. *et al* 2008 *Nucl. Fusion* **48** 045002
[53] Park J.M. *et al* 2009 *Phys. Plasmas* **16** 092508
[54] Suzuki T. *et al* 2011 *Nucl. Fusion* **51** 083020
[55] Chapman I.T. *et al* 2008 *Plasma Phys. Control. Fusion* **50** 045006
[56] Chapman I.T. *et al* 2009 *Phys. Plasmas* **16** 072506
[57] Turnyanski M. *et al* 2009 *Nucl. Fusion* **49** 065002
[58] Hawryluk R.J. *et al* 1980 An empirical approach to tokamak transport *Physics of Plasmas Close to Thermonuclear*

Conditions ed B. Coppi *et al* (Brussels: CEC) vol 1, pp 19–46
[59] Bickerton R.J., Connor J.W. and Taylor J.B. 1971 *Nature Phys. Sci.* **229** 110
[60] Galeev A.A. 1971 *Sov. Phys.—JETP* **32** 752
[61] Zarnstorff M.C. and Prager S.C. 1984 *Phys. Rev. Lett.* **53** 454
[62] Peeters A.G. 2000 *Plasma Phys. Control. Fusion* **42** B231
[63] Sauter O., Angioni C. and Lin-Liu Y.R. 1999 *Phys. Plasmas* **6** 2834
[64] Ohkawa T. 1970 *Nucl. Fusion* **10** 185
[65] Fisch N.J. 1987 *Rev. Mod. Phys.* **59** 175
[66] Lin-Liu Y.R. and Hinton F.L. 1997 *Phys. Plasmas* **4** 417
[67] Pankin A. *et al* 2004 *Comput. Phys. Commun.* **159** 157
[68] Zarnstorff M.C. *et al* 1990 *Phys. Fluids* B **2** 1852
[69] Wilson J.R. 2003 *Phys. Plasmas* **10** 1733
[70] Hosea J. *et al* 2008 *Phys. Plasmas* **15** 056104
[71] Taylor G. *et al* 2010 *Phys. Plasmas* **17** 056114
[72] Mazzucato E. *et al* 2008 *Phys. Rev. Lett.* **101** 075001
[73] Yuh H. *et al* 2011 *Phys. Rev. Lett.* **106** 055003
[74] Liu D. *et al* 2010 *Plasma Phys. Control. Fusion* **52** 025006
[75] Staebler G.M. *et al* 2008 *Proc. 22nd Int. Conf. on Fusion Energy 2008 (Geneva, Switzerland, 2008)* (Vienna: IAEA) TH/P8-43 and http://www-naweb.iaea.org/napc/physics/FEC/FEC2008/html/index.htm
[76] Luce T.C. 2011 *Phys Plasmas* **18** 030501
[77] Ferron J.R. *et al* 2011 *Nucl. Fusion* **51** 063026
[78] Waltz R.E., Staebler G.M., Dorland W., Hammett G.W., Kotschenreuther M. and Konings J.A. 1997 *Phys. Plasmas* **4** 2482
[79] Kinsey J.E., Staebler G.M. and Waltz R.E. 2008 *Phys. Plasmas* **15** 055908
[80] Murakami M. *et al* 2005 *Nucl. Fusion* **45** 1419
[81] Voitsekhovitch I. *et al* 2009 *Nucl. Fusion* **49** 055026
[82] Kinsey J.E. *et al* 2011 *Nucl. Fusion* **51** 083001
[83] Smith D.R. *et al* 2009 *Phys. Rev. Lett.* **102** 225005
[84] Smith D.R. *et al* 2009 *Phys. Plasmas* **16** 112507
[85] Ren Y. *et al* 2011 *Phys. Rev. Lett.* **106** 165005
[86] Wong K.L. *et al* 2007 *Phys. Rev. Lett.* **99** 135003
[87] Wong K.L. *et al* 2008 *Phys. Plasmas* **15** 056108
[88] Guttenfelder W. *et al* 2011 *Phys. Rev. Lett.* **106** 155004
[89] Stutman D. *et al* 2009 *Phys. Rev. Lett.* **102** 115002
[90] Wagner F. *et al* 1982 *Phys. Rev. Lett.* **49** 1408
[91] Snyder P. *et al* 2009 *Phys Plasmas* **16** 056118
[92] Maingi R. *et al* 2009 *Phys. Rev. Lett.* **103** 075001
[93] Sontag A.C. *et al* 2011 *Nucl. Fusion* **51** 103022
[94] Boyle D.P. *et al* 2011 *Plasma Phys. Control. Fusion* **53** 105011
[95] Diallo A. *et al* 2011 *Nucl. Fusion* **51** 103031
[96] Dickinson D. *et al* 2011 *Plasma Phys. Control. Fusion* **53** 115010
[97] Greenwald M. *et al* 1988 *Nucl. Fusion* **28** 2199
[98] Greenwald M. 2002 *Plasma Phys. Control. Fusion* **44** R27
[99] Chang C.S. and Hinton F.J. 1982 *Phys. Fluids* **25** 1493
[100] ITER Physics Experts Groups 1999 *Nucl. Fusion* **39** 2175
[101] Kugel H. *et al* 2008 *Phys. Plasmas* **15** 056118
[102] Bell M. *et al* 2009 *Plasma Phys. Control. Fusion* **51** 124054
[103] Angioni C. *et al* 2007 *Nucl. Fusion* **47** 1326
[104] Greenwald M. *et al* 2007 *Nucl. Fusion* **47** L26
[105] Lutjens H. *et al* 1996 *Comput. Phys. Commun.* **97** 219
[106] Glasser A.H. and Chance M.C. 1997 *Bull. Am. Phys. Soc.* **42** 1848
[107] Wesson J. 1997 *Tokamaks* (Oxford: Clarendon)
[108] Gates D.A., Menard J.E. and Marsala R.J. 2004 *Rev. Sci. Instrum.* **75** 5090
[109] Akers R. *et al* 2002 *Phys. Rev. Lett* **88** 035002
[110] Maingi R. *et al* 2002 *Phys. Rev. Lett* **88** 035003
[111] Lazarus E. *et al* 1991 *Phys. Plasmas* B **3** 2220
[112] Gryaznevich M. *et al* 1998 *Phys. Rev. Lett.* **80** 3972
[113] Gates D.A. *et al* 2003 *Phys. Plasmas* **10** 1659
[114] Gates D.A. *et al* 2006 *Nucl. Fusion* **46** S22
[115] Holcomb C.T. *et al* 2009 *Phys. Plasmas* **16** 056116
[116] Menard J.E. *et al* 2005 *Nucl. Fusion* **45** 539
[117] Gerhardt S.P. *et al* 2009 *Nucl. Fusion* **49** 032003
[118] Breslau J. *et al* 2011 *Nucl. Fusion* **51** 063027
[119] Chapman I.T. *et al* 2010 *Nucl. Fusion* **50** 045007
[120] Gunter S. *et al* 2007 *Nucl. Fusion* **47** 920
[121] Heidbrink W.W. *et al* 2009 *Phys. Rev. Lett.* **103** 175001
[122] Heidbrink W.W. *et al* 2009 *Plasma Phys. Control. Fusion* **51** 125001
[123] Zhang W. *et al* 2008 *Phys. Rev. Lett* **101** 095001
[124] Hauff T. *et al* 2009 *Phys. Rev. Lett.* **102** 075004
[125] Howl W. *et al* 1992 *Phys. Fluids* B **4** 1724
[126] Strait E.J. 1994 *Phys. Plasmas* **1** 1415
[127] Lazarus E. *et al* 1996 *Phys. Rev. Lett* **77** 2714
[128] Sabbagh S.A. *et al* 1996 *Proc. 16th Int. Conf. on Fusion Energy (Montreal, Canada, 7–11 October 1996)* (Vienna: IAEA) AP2-17
[129] Sabbagh S.A. *et al* 2002 *Phys. Plasmas* **9** 2085
[130] Menard J.E. *et al* 2003 *Nucl. Fusion* **43** 330
[131] Sabbagh S.A. *et al* 2004 *Nucl. Fusion* **44** 560
[132] Ferron J.R. *et al* 2005 *Phys. Plasmas* **12** 056126
[133] Sips A.C.C. *et al* 2005 *Plasma Phys. Control. Fusion* **47** A19
[134] Strait E.J. *et al* 1995 *Phys. Rev. Lett.* **74** 2483
[135] Menard J.E. *et al* 2004 *Phys. Plasmas* **11** 639
[136] Bondeson A. and Ward D.J. 1994 *Phys. Rev. Lett* **72** 2709
[137] Ward D.J. and Bondeson A. 1995 *Phys. Plasmas* **2** 1570
[138] Sontag A.C. *et al* 2005 *Phys. Plasmas* **12** 056112
[139] Reimerdes H. *et al* 2006 *Nucl. Fusion* **13** 056107
[140] Sabbagh S.A. *et al* 2006 *Phys. Rev. Lett.* **97** 045004
[141] Sabbagh S.A. *et al* 2006 *Nucl. Fusion* **46** 635
[142] Sontag A.C. *et al* 2007 *Nucl. Fusion* **47** 1005
[143] Sabbagh S.A. *et al* 2010 *Nucl. Fusion* **50** 025020
[144] Sabbagh S.A. *et al* 2010 *Proc. 23rd Int. Conf. on Fusion Energy 2010 (Daejeon, Korea, 2010)* (Vienna: IAEA) CD-ROM file EXS/5-5 and http://www-naweb.iaea.org/napc/physics/FEC/FEC2010/html/index.htm
[145] Gude A., Guenter S., Sesnic S. and the ASDEX Upgrade Team 1999 *Nucl. Fusion* **39** 127
[146] Okabayashi M. *et al* 2011 *Phys. Plasmas* **18** 056112
[147] Berkery J.W. *et al* 2010 *Phys. Plasmas* **17** 082504
[148] Berkery J.W. *et al* 2010 *Phys. Rev. Lett.* **104** 035003
[149] Berkery J.W. *et al* 2011 *Phys. Plasmas* **18** 072501
[150] Berkery J.W. *et al* 2011 *Phys. Rev. Lett* **106** 075004
[151] Reimerdes H. *et al* 2011 *Phys. Rev. Lett.* **106** 21502
[152] Politzer P.A. *et al* 2005 *Nucl. Fusion* **45** 417
[153] Stutman D. *et al* 2006 *Phys. Plasmas* **13** 092511
[154] Levinton F.M. *et al* 2007 *Phys. Plasmas* **14** 056119
[155] Yuh H.Y. *et al* 2009 *Phys. Plasmas* **16** 056120
[156] Gerhardt S.P. *et al* 2012 *Fusion Sci. Technol.* **61** 11
[157] Troyon F. *et al* 1984 *Plasma Phys. Control. Fusion* **26** 209
[158] Moreau D. *et al* 2011 *Nucl. Fusion* **51** 063009
[159] Moreau D. *et al* 2003 *Nucl. Fusion* **43** 870
[160] Taylor G. *et al* 2012 *Phys. Plasmas* **19** 042501
[161] Kessel C.E. *et al* 2005 *Nucl. Fusion* **45** 814
[162] Kessel C.E. *et al* 2006 *Phys. Plasmas* **13** 056108
[163] Gates D.A. *et al* 2006 *Nucl. Fusion* **46** 17
[164] Soukhanovskii V.A. *et al* 2009 *Phys. Plasmas* **16** 022501
[165] Soukhanovskii V.A. *et al* 2009 *Nucl. Fusion* **49** 092025
[166] Ryutov D. 2007 *Phys. Plasmas* **14** 64502
[167] Ryutov D. *et al* 2008 *Phys. Plasmas* **15** 092501
[168] Soukhanovskii V.A. *et al* 2011 *Nucl. Fusion* **51** 012001